Calibration of micro and nanorobotic systems : Contribution of influential parameters to the geometric accuracy.

Ning Tan

To cite this version:

Ning Tan. Calibration of micro and nanorobotic systems : Contribution of influential parameters to the geometric accuracy.. Micro and nanotechnologies/Microelectronics. Université de Franche-Comté, 2013. English. <tel-01025313>

HAL Id: tel-01025313

https://tel.archives-ouvertes.fr/tel-01025313

Submitted on 17 Jul 2014

HAL is a multi-disciplinary open access archive for the deposit and dissemination of scientific research documents, whether they are published or not. The documents may come from teaching and research institutions in France or abroad, or from public or private research centers.

L'archive ouverte pluridisciplinaire **HAL**, est destinée au dépôt et à la diffusion de documents scientifiques de niveau recherche, publiés ou non, émanant des établissements d'enseignement et de recherche français ou étrangers, des laboratoires publics ou privés.

Thèse de Doctorat

école doctorale sciences pour l'ingénieur et microtechniques

UNIVERSITÉ DE FRANCHE-COMTÉ

Calibration of micro and nanorobotic systems: Contribution of influential parameters to the geometric accuracy

Ning TAN

SPIM

Thèse de Doctorat

école doctorale sciences pour l'ingénieur et microtechniques

UNIVERSITÉ DE FRANCHE-COMTÉ

THÈSE présentée par

Ning TAN

pour obtenir le

Grade de Docteur de
l'Université de Franche-Comté

Spécialité : **Automatique**

Calibration of micro and nanorobotic systems: Contribution of influential parameters to the geometric accuracy

Unité de Recherche :
FEMTO-ST, UMR CNRS 6174

Soutenue le 16 Decembre 2013 devant le Jury :

Wisama KHALIL	Président	Professeur, Ecole centrale de Nantes
Stéphane REGNIER	Rapporteur	Professeur, Université Pierre et Marie Curie
Frédéric LAMARQUE	Rapporteur	Maître de Conférences HDR, Université de Technologie de Compiègne
David J. CAPELLERI	Examinateur	Assistant Professor, Purdue University, USA
Nicolas CHAILLET	Directeur de thèse	Professeur, Université de Franche-Comté
Cédric CLEVY	Co-directeur de thèse	Maître de Conférences, Université de Franche-Comté

Acknowledgements

I heartily acknowledge and thank my advisors Professors Nicolas Chaillet and Cédric Clévy. Three and a half years ago, they accepted me as their PhD student. I appreciate both of them for giving me the opportunity to obtain a French degree even though I can not speak French. I would like to thank Nicolas for the enlightening guidance and suggestions. He was so busy but still planned one meeting with me every month. I am grateful to Cédric for teaching me about organizing, planning, and doing my research effectively. He gave me countless suggestions and were always willing to help in every possible way whenever I had some problem. I have learned from him an enormous amount not only about research, but also about the need for balance in all things.

I would like to acknowledge Professor Stéphane Régnier and Professor Frédéric Lamarque for being the jury members and the reporters that wrote positive reports for my dissertation. And I would like to thank Professor Wisama Khalil and Professor David J. Cappelleri for being the jury members of my defense. They all asked me some enlightening questions and gave me very useful advices.

I would like to thank Dr. Guillaume Laurent who had help me a great deal for the 4th chapter of my dissertation. I have learned a lot about computer vision, cameras, hardware, and many other things from him.

I would like to thank Patrick Rougeot for telling me about the knowhow of AFM probe, Dr. Ioan Alexandru Ivan for teaching me how to use the interferometer, and Dr. Joel Agnus for consulting the electronics.

Many colleagues in AS2M department provided their help during my PhD, they are Kanty Rabenorosoa, Bilal Komati, Naresh Marturi, Nandish R. Calchand, Ahmed Mosallam, Anne Delettre, Khelif Racha, and Vincent Chalvet, Micky Rakotondrabe, Yassine Haddab, Brahim Tamadazte, and Ion Lungu. Here I would like to express my gratitude to them.

I would like to thank David Guibert for his help in machining some mechanical parts which are required for my experimentations.

And finally and the most important, I would like to thank my parents Wenxiong Tan and Guiqing Yu for their unconditional love and constant encouragement.

Contents

1 Introduction **1**

2 Positioning Accuracy, Sensing, and Control at the Microscale **5**
2.1 Introduction . . . 5
2.2 Motivations . . . 5
2.2.1 Needs for microscale . . . 5
2.2.2 Needs for microrobots . . . 7
2.2.3 Needs for positioning accuracy . . . 8
2.3 Sources affecting positioning accuracy . . . 9
2.4 Sensors and sensing issues at the microscale . . . 12
2.5 Control strategies at the microscale . . . 14
2.5.1 Three-tier structure . . . 15
2.5.2 Actuator layer . . . 16
2.5.3 Planning layer . . . 17
2.5.4 Robot calibration . . . 18
2.6 Conclusions . . . 18

3 State of the Art **21**
3.1 Introduction . . . 21
3.2 Precision metrics . . . 21
3.2.1 ISO 9283 standard . . . 21
3.2.2 Other evaluation methods . . . 23
3.2.3 Metrics used in this thesis . . . 24
3.3 Calibration of macrorobotic systems . . . 28
3.4 Calibration of microrobotic systems . . . 31
3.4.1 Works without considering thermal compensation . . . 31
3.4.2 Works with thermal compensation . . . 34
3.4.3 Summary . . . 36
3.5 Sensing solutions . . . 37
3.5.1 Sensor for micropositioning . . . 38
3.5.2 Sensor for nanopositioning . . . 41
3.6 Conclusions and objectives . . . 43

4 Calibration of Microrobotic Systems **47**
4.1 Introduction 47
4.2 General methodology for calibration of microrobotic systems 48
4.2.1 Kinematic modeling 48
4.2.2 Classification of error sources 49
4.2.3 Parameters identification 50
4.3 XYΘ microrobotic system and vision system 53
4.4 Characterization and compensation of position-dependent errors along XY stages 55
4.4.1 Characterization of position-dependent errors 55
4.4.2 Compensation of position-dependent errors 56
4.5 Calibration of the serial XYΘ microrobotic system 61
4.5.1 Five calibration models 64
4.5.2 Calibration procedures 66
4.5.3 Measuring information 69
4.5.4 Parameters identification 69
4.5.5 Experimental identification and validation 71
4.6 Conclusions 76

5 Calibration of Nanopositioning Stages **79**
5.1 Introduction 79
5.2 Modeling and identification of 1-DoF nanopositioning stage 80
5.2.1 Geometric modeling 80
5.2.2 Thermal-drift modeling 81
5.2.3 Single model 83
5.2.4 Adaptive model using kiloMeter-Zero (KMZ) 84
5.2.5 Robustness criterion 87
5.3 Experimental study of 1-DoF nanopositioning stage 87
5.3.1 Experimental setup 87
5.3.2 Procedures of calibration and validation 88
5.3.3 Experimental results and discussions 90
5.4 Calibration of Multi-DoF nanopositioning stage 96
5.4.1 Modeling of 2-DoF nanopositioning stage 97
5.4.2 Experimental study of 2-DoF nanopositioning robot 97
5.5 Conclusions 98

6 Conclusions **105**

List of Figures

2.1 Example of error induced by yaw deviation. 9
2.2 Structure and dimension errors of the robotic manipulator where ΔH and ΔL are height and length errors of the base and the arm. 10
2.3 Assembly errors between two axes. 10
2.4 Position-dependent errors along single axis. 11
2.5 Hysteresis and creep in piezoelectric devices. 11
2.6 Three-tier structure of control architecture of microtask platforms. 15
2.7 Transformation (mapping) between robot frame and global frame. 16
2.8 (a) Measurement of stage position by interferometer; (b) Measurement of ambient temperature close to the stage; (c) Measurement of internal sensor of the stage; (d) Input voltage of the stage. 17
2.9 Architecture of actuator and planning layers. 19
2.10 Basic principle of robot calibration. Step (a): Model structure determination; Step (b): Data acquisition; Step (c): Model training and parameters identification; Step (d): Implementation of calibration model to the robot. 19

3.1 Positioning accuracy AP and repeatability RP. G is the barycenter of attained positions; O_c is the command pose. 22
3.2 Geometric representation of all input-output components of the 1-DoF nanopositioning stage. 25
3.3 Schematic diagram of the experimental setup [21]. 32
3.4 Schematic diagram of mapping from robot frame to global frame. 32
3.5 Schematic diagram of calibration process in [65]. 32
3.6 Coordinate frames assignment for micromanipulators in [65] 33
3.7 Schematic diagram of calibration process in [58]. 33
3.8 Schematic diagram of calibration process in [64]. 34
3.9 Experimental results of aligning the particles in a line, a cross, and a “W” after calibration [64]. 34
3.10 Schematic diagram of experimental setup for calibration of ultra-high-precision linear axis [55]. 35
3.11 Agietron Micro-Nano robot [54]. 36
3.12 Schematic diagram of mapping from robot frame to global frame. 37
3.13 Image of a local area of Pseudo-Periodic Pattern (PPP) where every dot is 2 μm in diameter. 39

3.14 Schematic diagram of absolute position retrieval procedure [88]. 40
3.15 Photos of experimental setup for testing measurement uncertainty. 40
3.16 Experimental results of measuring the fixed pattern. 42
3.17 Micropositioning accuracy in state-of-the-art [21, 58, 57, 65, 80, 81, 82, 93]. 44
3.18 Nanopositioning accuracy in state-of-the-art [54, 64, 87, 90]. 45

4.1 Kinematics of an n-DoF serial robot. World frame $\{O_{WF}, \vec{x}_{WF}, \vec{y}_{WF}, \vec{z}_{WF}\}$; joint variable q_k, $k = 1, \ldots, n$; joint frame $\{O_k, \vec{x}_k, \vec{y}_k, \vec{z}_k\}$, $k = 1, \ldots, n$; tool frame $\{O_{TF}, \vec{x}_{TF}, \vec{y}_{TF}, \vec{z}_{TF}\}$. 48
4.2 Assembly errors between two axes. $\{O_k, \vec{x}_k, \vec{y}_k, \vec{z}_k\}$=frame of mobile part of joint q_k; $\{O_{k+1}, \vec{x}_{k+1}, \vec{y}_{k+1}, \vec{z}_{k+1}\}$=frame of mobile part of joint q_{k+1}. . . 49
4.3 Position-dependent errors along a translation axis. $\{O_k, \vec{x}_k, \vec{y}_k, \vec{z}_k\}$=frame of mobile part of prismatic joint q_k. 50
4.4 Angle-dependent errors about a rotation axis. $\{O_k, \vec{x}_k, \vec{y}_k, \vec{z}_k\}$=frame of mobile part of revolute joint q_k. 51
4.5 Experimental setup for the calibration of XYΘ microrobotic system. . . . 53
4.6 Block diagram of characterization of nonlinearity errors. 55
4.7 Repeatability of errors in x direction when X stage is moving forwards. . . 56
4.8 Errors $(x_T - x_m)$ in x direction when X stage is moving forwards and backwards in one cycle. 57
4.9 Coupling errors $(0 - y_m)$ in y direction when X stage is moving forwards and backwards in one cycle. 57
4.10 Schematic diagram of the errors combination mechanism for compensation. 58
4.11 Block diagram of compensation for nonlinearity errors using lookup table. 59
4.12 Square trajectory (4 segments). 59
4.13 Accuracy of tracking 4×4 mm square trajectory with and without compensation. 60
4.14 Block diagram of interpolation and compensation. 61
4.15 Positioning accuracy of random points with and without compensation of position-dependent and geometric errors for XY stages. 62
4.16 Kinematic diagram of the XYΘ microrobotic system. y_1, x_2, z_3 are the motion joints Y, X, and Θ, respectively. 63
4.17 Flowchart of the calibration procedure for Model I and Model II. 67
4.18 Flowchart of the novel calibration procedure for Model III. 67
4.19 Flowchart of the novel calibration procedure for Model IV. 68
4.20 Flowchart of the novel calibration procedure for Model V. 68
4.21 Observability of cost function E with 3 to 2000 poses. 71
4.22 Joint coordinates of XYΘ stages in data acquisition. 72
4.23 Moving sequence of target points (P_T) in validation. 73
4.24 Block diagram of validation procedure. 74
4.25 Experimental results of positioning accuracies using five models. 74
4.26 Moving sequence of target points (P_T) in measuring angle-dependent errors $f_{ax}(\Theta)$ and $f_{ay}(\Theta)$. 74

5.1 Geometric errors of the nanopositioning stage in forward and backward motions. x_T is the target, x_m is the measured position along x, y_m is the measured position along y. 81
5.2 Relationship between temperature and thermal drift 82
5.3 Block diagram of the system with single calibrated model. 84
5.4 Block diagram of the system with adaptive model using kilometer zero. . . 85
5.5 Experimental setup comprising one single-axis nanopositioning stage and reflective object, two interferometers with affiliated pressure/temperature sensors, four temperature sensors. 88
5.6 Schematic diagram of the hardware allocation and signal flow. 89
5.7 Flow chart of calibration of nanopositioning stage considering thermal drift. 90
5.8 Reference trajectory of measurement for one cycle. 91
5.9 Reference validation trajectory. 91
5.10 Temperature during the experiment in metrology room. 91
5.11 Accuracies of the nanopositioning stage in forward and backward motions without calibration in metrology room. 92
5.12 Repeatability of the nanopositioning stage without calibration in metrology room. 92
5.13 Accuracy in training phase (TP). 94
5.14 Accuracy of the first test without calibration (T1). 94
5.15 Accuracy of the second test with adaptive model using KMZ (T2). 94
5.16 Accuracy of the third test with single model (T3). 94
5.17 Accuracy evolution of all validation poses in five days. Time 0 = end of training = start of validation. 95
5.18 Evolution of maximum accuracy and repeatability of every test in five days. Time 0 = end of training = start of validation. 95
5.19 Evolution of the room temperature in five days. 96
5.20 Relationship between temperature and accuracy and repeatability. 97
5.21 Trajectory of data acquisition for model training. 98
5.22 Coordinates and trajectory of six points for validation. 99
5.23 Experimental accuracy and repeatability of 2-DoF nanopositioning stage in training and validation phases. Time 0 = end of training = start of validation. 100
5.24 Temperature evolution in training and validation phases. 100
5.25 Schematic diagram of experimental setup with kilometer-zero defined by the AFM probe. 102
5.26 Prototype of the KMZ cell. 103

Chapter 1

Introduction

Human beings are always striving to explore the extremes of the scale spectrum. On one side, astronomy is the study of celestial objects involving distance of light year which is extremely large. On the other side, science and engineering at the micro-nano scales are as an exploration on another extreme. Driven by the requirement of high quality of life standard, we need to develop industrial products with small size, low cost, and specific or multi-functionalities. To meet these requirements, research on micro-nano scales has undergone a rapid development. A representative area is MicroElectroMechanical Systems (MEMS). The feature sizes of MEMS devices are from a few micrometers to one millimeter which allow them to break through the space limitation so as to integrate themselves into a wide range of systems. The application fields of MEMS range over automotive, aerospace, medical, chemical, biological, consumer electronics, and measurement devices. Especially in biological and medical areas, to exploit the nature and to root out the disease, research has to go down to cell and molecule. Such research usually needs to get help from miniaturized and precise devices which bring us a lot of benefits.

However, micro an nano scales are where humans can not access directly by themselves. A human being can not observe a micrometer-sized component without the help of a microscope. To pick up a component without using a specific tool is also impossible. For example, a component part of a MEMS, could be a few micrometers. We could manipulate it using a fine gripper or a probe while we can see it through a microscope. However, we might destroy the fragile component due to large force generated by our less accurate motion systems. Moreover, because of our less accurate motion systems, we cannot do the work with repeatability in micro and nano range without the help of micro-nano devices. Because of these facts, we have to get help from sensing and control techniques in order to achieve accuracies and repeatabilities which are compatible with the dimension of the objects being manipulated. These sensing and control techniques usually refer to microrobotics. Microrobotics is a multidisciplinary field that investigates robotic systems which possess either miniature size or precision in the microscopic level [6]. Their objectives are to help human to get access to the usually inaccessible world where needs tools for sensing and manipulating. The corresponding research objects

of these two areas are miniature robot and micromanipulation system [16] respectively. The miniature robot is with volume size down to sub-millimeter range which are able to immerse totally in the microworld.

High accuracy is usually a necessary condition of the performance of the system, i.e. being able to position a frame of a robot, typically an end-effector, at a desired location. To perform successful microtasks, we need microsystems or microrobots with high accuracy. However, this condition is difficult to obtain at the microscale, because of many sources of inaccuracy acting on microrobotic systems. These sources combine to affect the positioning accuracy. To better understand the robot behavior, some imperfections must be characterized and the influences of these sources must be quantified. This quantification knowledge can guide the design, selection of robot structures so as to minimize efforts for accuracy improvement. To improve the positioning accuracy, several approaches are possible through combining many sensors, such as position, force, temperature sensors, etc., with closed loop and/or open loop (i.e., calibration) strategy. In this thesis, we investigate calibration approach which is a systematic way to compensate imperfections and enhance positioning accuracy. Combining microscale measurement and robot calibration, imperfections could be compensated then the positioning accuracy could be improved.

However, at the microscale, there are lots of challenges to perform measurement meeting all requirements, i.e., resolution, accuracy, and range, etc. These challenges include sensing resolution, accuracy, range, bandwith, sensor size, and multi-DoF (Degrees-of-Freedom) [19]. To perform microscale measurement, sensors should be evaluated and the suitable ones should be selected to form an efficient sensing strategy. Calibration of micro and nanorobotic systems considering all the sources is rarely studied and the relative importance of these sources still remains unknown. Therefore, there are two main objectives to explore: 1. characterization of micro-nano robots performances and influences of imperfections; 2. dealing with performance improvements of micro-nano robots based on different kinds of models.

The document is organized in the following way:

In Chapter 2 we discuss the motivations for improving accuracy in micro-nano positioning. All possible imperfections that may affect micro-nano scale accuracy are discussed and presented. Commercially available sensors are presented and difficulties in sensing are discussed. Then applicable control strategies are presented and the approach of robot calibration is chosen.

Chapter 3 presents the state-of-the-art in regard to works on sensing and robot calibration issues. The evaluation criterions of robot performance are reviewed and the metrics to be used in this thesis is presented. We present a novel sensing solution for micropositioning measurement and an available measuring system in the market for nanopositioning measurement. Works on calibration of macro and micro-nano robots are presented. Based on which, both micro and nano robots are classified in terms of actuation features, and objectives of accuracy for micro-nano positioning are quantified. The objectives established in this chapter will be considered to realize in Chapters 4 and 5.

Micropositioning calibration is studied in Chapter 4. We present a generic framework for microrobotic calibration. As a preliminary step, characterization and compensation of XY stages are performed subsequently. A case study of XYΘ serial microrobot is detailed to illustrate the influences of the imperfections and accuracy improvement using the calibration framework and five calibration models.

As another main part of our work, Chapters 5 deals with the nanopositioning calibration. We discuss the modeling, propose calibration models, and perform experimental calibrations and validations on a single-axis and a 2-DoF nanopositioning robots.

Chapter 6 concludes this thesis. We present a summary of the results and contributions arising from this work. Finally, we outline some perspectives concerning the micro-nano measurement and calibration.

Chapter 2

Positioning Accuracy, Sensing, and Control at the Microscale

2.1 Introduction

In this chapter, we will discuss the motivations, related issues and primary direction of our research. First we will discuss the motivation aspects in terms of needs for microscale technology, application of microrobots, and positioning accuracy of the microrobots. This first section will conduct to show how difficult it is to obtain high level and guaranteed positioning accuracies at the micro-nano scales. To tackle this task, we will then discuss influential imperfections affecting microscale positioning accuracies, and the commercially available ways to measure or take them into account. Finally, we will discuss control strategies for microscale positioning and explain why we choose robot calibration approach.

2.2 Motivations

2.2.1 Needs for microscale

With the development of science and technology as well as living standard, more and more attention is being paid to microscale because things in macroscale have not satisfied all human requirements. A conventional industry involving small scale components is typically watchmaking. Watch is a precise and small mechanical and/or electronic machine which integrates a number of tiny components. Especially for a versatile watch, there will be more components to be integrated. Design, fabrication, and assembly of these components are issues in the millimeter range.

Towards a smaller scale, MEMS have grown rapidly in last decades thanks to their advantages of fast speed, small size, and low cost. They integrate mechanical and electronic components and have feature sizes ranging from micrometers to millimeters. The first advantage of MEMS is that micrometer size brings some advanced performances which can not be achieved at the macroscale. For optical applications, features may be

made with size on the order of the wavelength of light, thus making them attractive for many optical applications. For example, micromechanical switches or actuated structures fabricated as part of a communications circuit allow phase shifting and signal switching at speeds that would be impossible to achieve using macro-scale switches. Another advantage is that their sizes make them possible to integrate into a wide range of systems. MEMS devices generally range in size from a few micrometers to one millimeter. This allows on-chip integration of electromechanical devices and electronic circuits used to control them. Furthermore, by leveraging the parallel fabrication techniques of the integrated circuits, MEMS devices can be fabricated in parallel which leads to a reduction in the manufacturing cost and improvement in reliability making them cost-effective for many uses.

MEMS have been used in a variety of areas. One application is automobile airbags which are commonly used safety devices of vehicle. The airbay has a central Airbag control unit which monitors a number of related sensors within the vehicle, including accelerometers, impact sensors, side (door) pressure sensors, wheel speed sensors, gyroscopes, brake pressure sensors, and seat occupancy sensors. Some smart consumer electronics, such as an iphone, equip lots of functionalities that people can enjoy their convenience for daily life. In addition, some office supplies, such as ink-jet printers and projection display systems, also benefit from MEMS techniques.

Thanks to MEMS technology, research has been going down to cells and molecules for the development of biological and medical sciences which is different from the normal scale of clinical operations. For example, Optical Coherence Tomography (OCT) has the ability to detect cancerous tissues at their early stages thanks to its micron-scale resolution [76]. For internal organs, endoscopic probes are needed as the penetration depth of OCT is about 1-3 mm. MEMS devices have been widely used as the scanning engines in endoscopic OCT probes. IntraCytoplasmic Sperm Injection (ICSI) is an in vitro fertilization procedure in which a single sperm is injected directly into an egg. Studies have shown that the average human sperm length is approximately 50 μm [53]. This size is so small that can not be visible to human eyes. We must get help from advanced sensing techniques to get images of the invisible matter. Once we can see things at the microscale, we also need to manipulate them by tools with microscale precision. Another example of micro techniques is minimally invasive surgery which has been becoming more and more common in hospitals. During a minimally invasive procedure, surgeons make some small incisions (just a few millimeters in some cases) instead of large openings (a few centimeters) in the skin. Because the incisions are small, patients tend to have quicker recoveries and less discomfort than with conventional surgery.

As the foundation for many engineering fields, there is an urgent need for new materials because lack of suitable materials hinder development of many other technologies. A lot of nanoscience and nanotechnologies are concerned with producing new or enhanced materials. The ability to machine materials to very high precision and accuracy (better than 100nm) is leading to considerable benefits in a wide range of industrial sectors. Nanomaterials can be constructed either by “top down” or “bottom up” techniques. The former produces small structures from larger pieces of material, for example by etching

to create circuits on the surface of a silicon microchip. The latter is constructed atom by atom or molecule by molecule.

2.2.2 Needs for microrobots

Considering the success rate, speed, and reliability of the tasks performed at the microscale as well as avoiding the contamination of micro-components, the microtasks, such as microassembly [67, 81, 13, 12], biological injection [78, 58, 34], specimen handling [74], microdispensing [31], and AFM scanning [72], usually rely on microrobotic systems with automatic or semi-automatic control instead of fully manual operations [16, 66].

When microassembly task requires a human operator to pick and place micro-components manually using high power microscopes and microtweezers, the assembly is tiresome, time consuming and causes lots of losses because objects to be manipulated are extremely small and fragile. Assembly of micro-components requires specific devices that have to work in a reduced free space and requests advanced control of a gripping tool. A micromanipulation cell, dedicated to manipulate micro-components, can enhance the microassembly of MEMS or MOEMS (Micro Electro-Optical-Mechanical System) applications. So, there is a trend that MEMS and MOEMS manufacture fully or at least partially relies on microrobots. The cell consists of one of several microrobots with microgrippers which are capable of picking up a micropart, reorienting, translating and joining it to another micropart or to assembling slots. Expect for micromanipulation cells, miniature mobile microrobots are also able to perform assembly [23].

In addition, most of MEMS and MOEMS products including actuators and sensors can be seen as microrobots. For example, the micromirror designed for the OCT [76] can be seen as a parallel microrobot which is capable of performing scanning through the mirror plate controlled by the actuator [50]. The control of the micromirror would be in open loop. With existing technologies, it cannot be in in closed loop because it is difficult or nearly impossible to integrate sensors to have sensory feedback.

The core device of the minimally invasive surgery is an endoscope which is a long, thin tube with a miniature camera. Images from the endoscope are projected onto monitors then surgeons can get a clear (and magnified) view of the surgical area. Special instruments are passed through the other openings. These instruments allow humans to perform the surgery by exploring, removing, or stitching whatever's wrong (e.g., a tumor) inside the body. The whole system including all these endoscope, monitor, instruments is a part of medical microrobot. Research on microrobotic pills is also going to revolutionize several decease treatments, such as cancer treatment. The tiny mobile robots are also being developed by researchers [29, 22, 38] whereby therapies will be delivered to hard-to-reach places inside the body. For such applications, the quality of tasks to be performed directly depends on the size of robotic tools: the smaller they can be, the more inner body they will be able to reach providing localized and thus less harmful injection or action.

Research of new materials need to probe matter at the nanoscale. It has been 32 years since the Scanning Tunneling Microscope (STM) was invented, followed four years

later by the Atomic Force Microscope (AFM) when nanoscience and nanotechnology really started to take off. Various forms of scanning probe microscopes based on these discoveries are essential for many areas of nanoscience and nanotechnology research. The AFM is one of the foremost tools. An AFM is a submillimeter-sized cantilever with one or more ultrasharp tips at the end. The AFM cantilevers normally are integrated with microrobotic scanners as the end-effectors. Then the whole systems can perform imaging, measuring, and manipulating matter at the nanoscale.

Besides, sometimes we need to perform some experiments with repeatability in micrometer range, then microrobots should be employed because manual manipulation can not perform tests with so high repeatability. To investigate the micro-nano phenomena, for example the effect of some surface forces, we need a microsystem or microrobot which is able to precisely position to perform the task. Sometimes we need to accurately control the location of contact area. It will be required to accurately sense and tune the force from time to time because the surface is not homogeneous at the microscale.

2.2.3 Needs for positioning accuracy

Because the objects to be dealt with at the microscale are so small that a small positioning error or misalignment may lead to task failure. For example, assembly of optical micro-components require high positioning accuracy. In fiber-to-fiber coupling, 1 μm positioning error leads to 50 % intensity loss. To reach high enough performance, the advanced MOEMS products require 100 nm/0.01 ° positioning accuracy. For some small cells manipulation (e.g., prokaryotic cells) which have typical sizes ranging form 1 to 5 μm, the required accuracy of micropositioning should be in submicrometer range.

Since microtask platforms usually consist of one or several microrobots, the efficiency of the microtasks depends on the performance of microrobots to a large extent. Among the characteristics of the microrobotic systems, positioning accuracy is an foremost criterion evaluating the positioning performance. To fulfill successful tasks, it is very important to control positioning within a certain accuracy range. As the macrorobots, microrobots are with high repeatability, but accuracy does not meet requirements in many applications. Since the tasks at the microscale require more and more flexibility, accuracy can become an issue to reach any specific target position or/and orientation and not only taught positions.

The MEMS micromirror for OCT applications with a circular mirror plate was proposed and fabricated [50]. The measured lateral shift and tilt angle of the mirror plate are about 7 μm and 0.7° respectively, through the entire piston motion 227 μm and $\pm 11^\circ$. If we would like to achieve smaller lateral shift and tilt angle, the errors should be characterized and compensated efficiently. AFM scanners usually consist of XYZ nanopositioning stages whose motion behaviors affect the scanning performances. For some applications, the out-of-plane motion should be less than a few nanometers over entire XY scan range when imaging a flat surface. In these cases, Z stages must be actively controlled, even though only XY planar motions are desired.

However, achieving higher accuracy is always difficult. For example, if the perpendicularity error between X and Y axes is 0.1°, 1 cm motion along Y could induce error of 17

μm along X. This error is in the range of the typical values for the stroke of microgrippers or tools acting with active material. Another example is shown in Fig. 2.1 that the error at the end-effector of a micropositioning stage mounted with a 20 mm robotic arm could be around 3 μm at the end-point due to yaw deviation 150 μrad. This error is larger than most bacteria which have sizes of $1 \sim 2$ microns. Hence, the error on a microrobot for bacteria manipulation must be compensated. At the microscale, it is difficult to measure and even quantify the influence of these imperfections. The environmental noise could lead to more than 100 nm deviation that it is difficult to reach such positioning accuracy value [9].

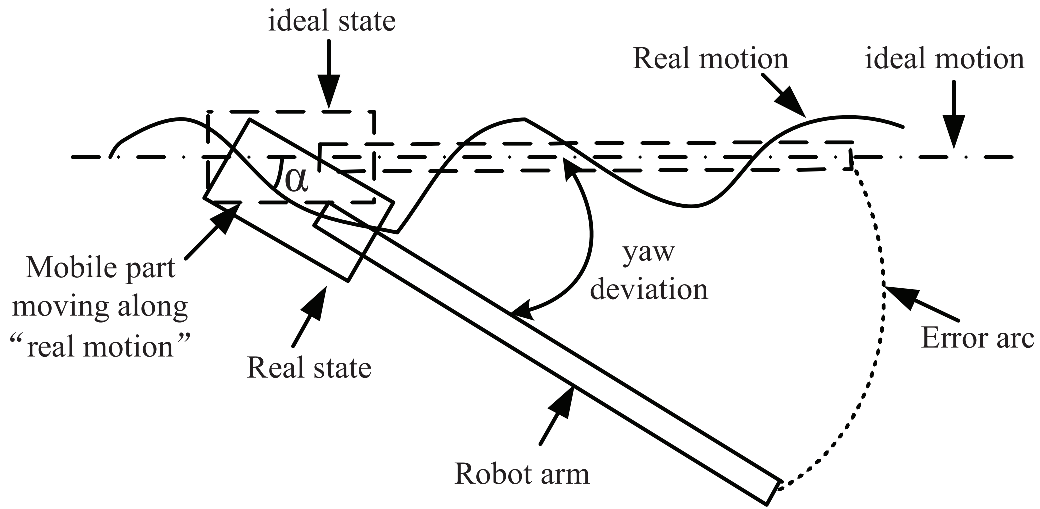

Figure 2.1: Example of error induced by yaw deviation.

Therefore, the accuracy or quality of position control of microrobots we can achieve directly influences on task success and task quality which are very important.

2.3 Sources affecting positioning accuracy

At the microscale, there are different sources of imperfections acting on microrobotic systems [62]. The positioning accuracy is hampered by the imperfections.

Some errors come from fabrication process or wear and tear during the normal use of robots. For example, the structure and dimension of the robot (Fig. 2.2) varies more or less after they left the factory. ΔH and ΔL are height and length errors of the base and the arm. The values of nominal kinematic parameters (L, H in Fig. 2.2) are not consistent with those written in datasheets. So the control models based on the nominal kinematic values are likely not able to fulfill the manipulation tasks.

In microscale applications, several micropositioning stages often have to be assembled to perform some functionalities. In such cases, errors about parallelism and perpendicularity may be induced during the manual assembly process. In Fig. 2.3, the angle γ

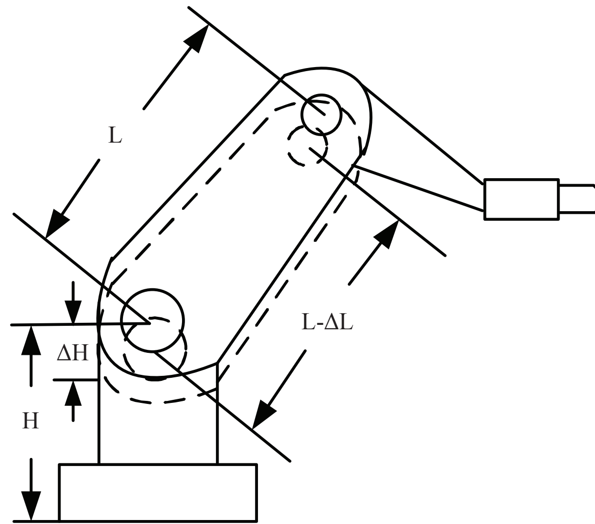

Figure 2.2: Structure and dimension errors of the robotic manipulator where ΔH and ΔL are height and length errors of the base and the arm.

between two axes is usually desired to be right angle, however, it is difficult to be exact right angle by manual assembly.

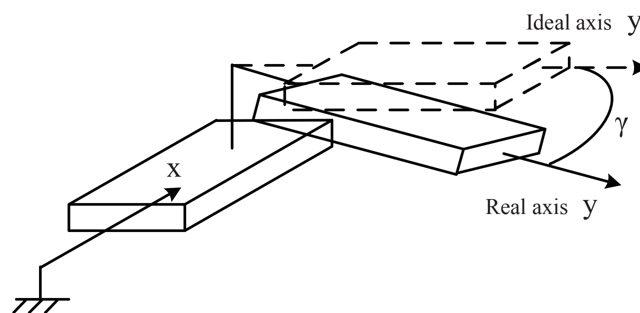

Figure 2.3: Assembly errors between two axes.

Another kind of imperfection is due to the inherent characteristics along axes or actuators. Machine tool industry pays more attention to these sources than robot manufactures. However, these sources become significant at the microscale where higher accuracy is desired. For positioning, linear motion is required, but at the microscale we cannot consider it as perfectly linear. Fig. 2.4 shows position-dependent errors such as flatness and straightness errors as well as roll, pitch, and yaw angles. The absolute values of these sources are usually small but induce errors to be considered or influential at the micro or nanoscale. The example of Fig. 2.1 shows that the error induced by the small yaw angle 150 μrad can be amplified by the 20 mm length robot arm to 3 μm. In ball and lead screw products, there is backlash depending on different actuation principles.

Backlash affects the positioning performance when direction change happens. This error is usually from 100 nm to several microns according to the datasheets.

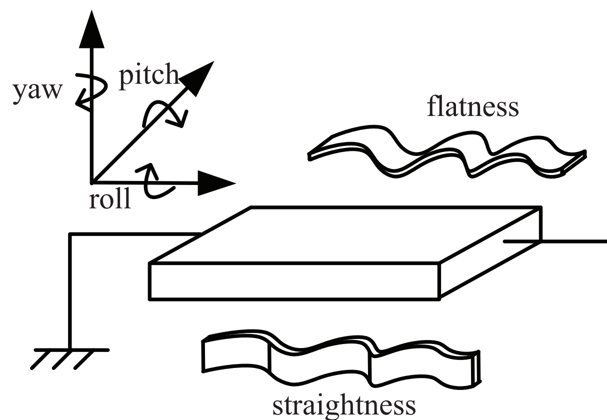

Figure 2.4: Position-dependent errors along single axis.

For micro-nano positioning, piezoelectric devices are widespread used because of their fast response time, high resolution and sensor capabilities [69]. However, there are nonlinearities in voltage-strain transfer which induce hysteresis and creep behavior (Fig. 2.5). They affect the repeatability and accuracy of the micropositioning stages using piezoelectric actuators, especially in open loop but not closed loop.

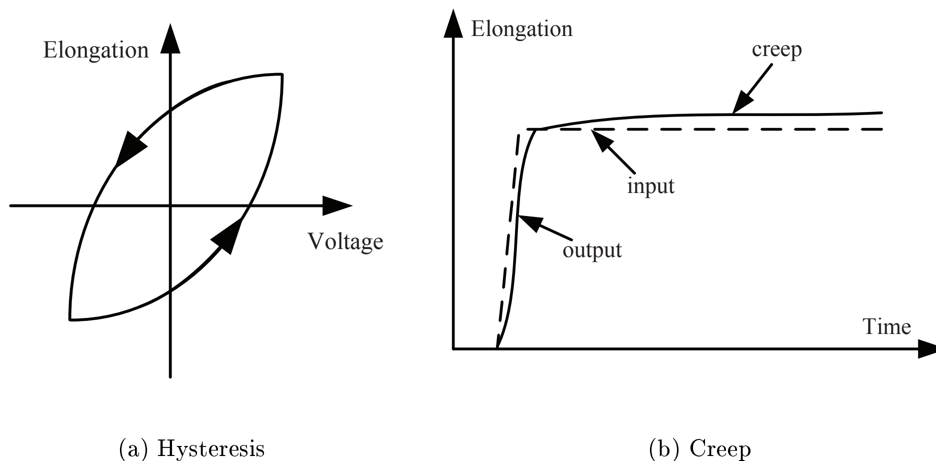

(a) Hysteresis (b) Creep

Figure 2.5: Hysteresis and creep in piezoelectric devices.

Some errors are induced by environments, such as temperature [92], humidity [35], and noise [10]. Due to different requirements of accuracy, temperature has more significant effects at the microscale than macroscale. Even in a clean room with controlled

temperature, the influence of small temperature change $\pm$ 1 or $\pm$ 2 $°C$ can not be neglected. Acoustic influence could also become an issue of positioning accuracy when the microrobotic systems are working in a noisy environment. Vibration can be minimized by placing the microrobotic systems on the anti-vibration tables and isolation bases.

The main sources of imperfections and some examples are summarized in Table 2.1. All the sources exist for both macrorobots and microrobots. However, macrorobots do not consider some sources because of their small influences on less strict requirement of accuracy. The importance of some sources at the microscale differs from macroscale where different levels of accuracy are concerned. And it is very difficult to quantify these imperfections.

Table 2.1: Imperfections affecting accuracy of microrobotic systems.

Sources	Examples
Fabrication or wear and tear	- Structure and dimension errors
Mounting and assembly	-Assembly errors
Intrinsic imperfections of the actuators	- Position-dependent errors (main direction, vertical flatness and horizontal straightness) - Angle-dependent errors - Backlash - Hysteresis and creep - Flexibility
Environmental influence	-Temperature - Humidity - Acoustic - Mechanical vibration

2.4 Sensors and sensing issues at the microscale

To achieve high accuracy, first of all, we need to be able to measure the real positions and imperfections accurately. The measurement task can be fulfilled by sensors. However, sensing at the microscale is a very challenging issue. Microscale measurement requires sensing devices with high resolution (e.g., a few nanometers) and accuracy (e.g., tens of nanometers) because motion and errors in this scale are very small. Only accurate enough sensors can detect such motion and errors otherwise they may immerse in measuring uncertainty of the sensors.

In addition, suitable sensing range and bandwidth are required for an appropriate sensor. Microtask platforms usually consist of micropositioning stages for coarse positioning and nanopositioning stages for fine positioning. Measurement of coarse positioning

requires relatively large measuring range (a few millimeters), and medium levels (tens of nanometers) of resolution/sensitivity and stability/repeatability are sufficient.

Based on their locations relative to the objects to be measured, sensors can be classified into proprioceptive (internal) and exteroceptive (external) ones [19]. Proprioceptive sensors are often embedded into the robots thanks to their physical principles favorable to miniaturization. Proprioceptive sensors provide measurements in the robot frame. Exteroceptive sensors are independent to the robots which provide measurements in the sensor frames.

Sensors are affected by changes of air refraction index, temperature, humidity, and other environmental behaviors. To minimize the environmental influence, sensors should be mounted as close as possible to the robot end-effector. The longer the measuring path, the more the measurement will be influenced by changes of environment conditions. Displacement and force signals at the micro-nano scale are very weak relative to those at the macroscale. Noises caused by the environment may have the same order of magnitude as the useful signals. This is a specific problem at the microscale which needs additional noises-eliminating strategies.

Optical sensors are commonly used thanks to their high resolution, accuracy, wide measuring range and bandwidth. They normally need reflecting objects (e.g. a mirror) to reflect the beam they generate. Using reflecting objects may introduce inaccuracies linked to the reflection depending on the state of the mirror surface. And it is not easy to find such objects and integrate them on the microrobots.

Vision system is relatively low-cost and more flexible which does not need reflecting object but calibration target (e.g., dots board with known size). The vision system need calibration to correlate real motion and that in the image. The resolution of the vision system is often linked with the measuring range. High resolution and wide measuring range are usually a contradiction. To increase resolution, we must reduce the measuring area and vice verse. High magnification microscope using usual algorithm is able to reach resolution of $1/10$ pixel with pixel size $\simeq 1 \times 1\ \mu m$. We can achieve resolution of $1/1000$ pixel but require specific patterns and algorithm which are not yet commercially available.

Capacitive sensors themselves are small (the sensor probes could be $1 \times 1 \times 3$ cm). But they require the target surfaces larger than their probe surfaces. This sometimes is impossible in case the objects to measure are small (a few millimeters or smaller) which are usually the cases, such as the microgrippers.

Multi-DoF sensing is required when the microrobot to be measured motions in multi-DoF. In current market, there is a lack of sensing device satisfying multi-DoF measurement. From Table 2.2, the optical sensors usually can only offer 1-DoF measurement and the vision is able to provide 2-DoF measurement. However, vision's performances on resolution, accuracy, and measuring range are less efficient than optical sensors. If performing multi-DoF measurement, several sensors should be combined to build a measuring system. Like most of the microrobots, our microrobotic system also needs multi-DoF measurement. In this case, another problem may appear, that is, the workspace is too small to arrange all these sensors. Optical sensors and vision systems usually have bulky

sizes relative to the microrobots, let alone the end-effectors, which make the workspace very crowded.

In summary, for measurement at the microscale, the following qualifications are required:

- high resolution and accuracy
- suitable sensing range and bandwidth
- small volume
- noises reduction
- multi-DoF sensing
- low sensitivity to environmental influence

The measuring range, resolution/sensitivity, stability/repeatability, measuring DoF, volume, and cost of seven kinds of external sensors are evaluated and summarized in Table 2.2. However, there are few sensors satisfying all these requirements. Sensors that overcome all the challenges are still under development in research laboratories and companies. In Chapter 3, we will discuss the measuring systems we choose and give the evaluations of their measuring uncertainties.

Table 2.2: External sensors for position measurement at the microscale.

Sensors	Laser interferometer	Triangulation Laser sensor	Capacitance sensor	Video camera	Eddy current sensor	PSD	MEMS analyzer
Measuring range	wide 10 mm	short 500 μm	short $< 500\ \mu m$	medium $500 \sim 1000\ \mu m$	short 500 μm	medium 4 mm	medium 1 mm
Resolution or sensitivity	high $1 \sim 2$ nm	medium 10 nm	high < 1 nm	low 1 μm	medium 30 nm	low 0.7 μm	high 1 nm
Stability or repeatability	medium	medium	low	medium	medium	low	high
DoF	one	one	one	two/three	one	two	three
Volume	medium 7 cm	medium 7 cm	small 5 mm	large 20 cm	small 3 mm	small 1 cm	large 20 cm
Cost	high	medium	medium	medium	medium	low	very high

2.5 Control strategies at the microscale

Once we can measure the positions or imperfections, we need to choose a strategy for positioning control based on the measured information. This section will discuss the control strategies that can be applied to achieve micro-nano positioning.

2.5.1 Three-tier structure

Nowadays, most control architectures of microtask platforms are constructed in a three-tier structure [93]. According to the functionality of every part, the platform can be divided into three layers (Fig. 2.6): actuator control layer, motion planning layer, and mission control layer.

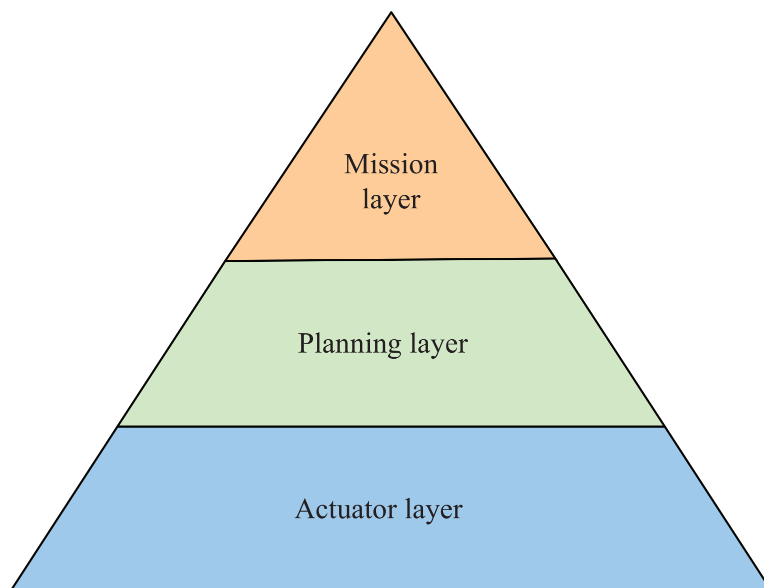

Figure 2.6: Three-tier structure of control architecture of microtask platforms.

The actuator control layer is the bottom layer of the whole system. Because this layer only deals with the individual actuators, it is also called local control layer. It is responsible for driving and maintaining the micropositioning axis at desired positions given corresponding commands from the higher layers. This layer provides the control signal (voltages) to the actuator and reads the feedback signal from the internal sensors if any. Various control strategies [8] have been used in this layer for actuator control. This layer enables to compensate the nonlinear behavior inherent in the actuators, such as hysteresis, creep.

The middle layer is the planning layer which concerns relations between each device, but not about the control of individual actuators. Different from the local sensing system in the actuator layer, the planning layer usually adopts external measuring systems which are able to provide position information in a global frame. This layer enables a synchronization of all devices in the platform and compensates some imperfections which can not be detected in actuator layer alone, such as mounting errors. The synchronization enables to achieve a trajectory based on several elementary actuator motions. In modeling of the micromanipulation platform, several coordinate frames and their one-to-one relationship must be established. To correlate them, the transformation matrices between them must be determined. In practical micromanipulation platforms, the re-

quired transformation is usually from the robot frame to the global frame (substrate) as shown in Fig. 2.7. For example, to map the robot frame $\{O_R, x_R, y_R, z_R\}$ to the global frame $\{O_G, x_G, y_G, z_G\}$, the robot end-effector is required to reach at least three points on the substrate.

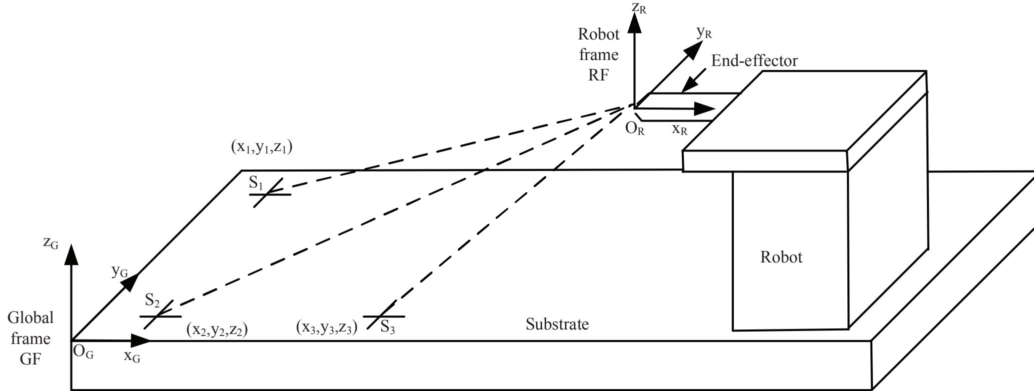

Figure 2.7: Transformation (mapping) between robot frame and global frame.

The top layer is mission layer which directly interacts with operators. People communicate in this layer with the systems through the I/O interface, such as, script-based commands, joystick, and virtual reality (VR) environment.

2.5.2 Actuator layer

Normally, most of the commercial motorized micropositioning stages are equipped with built-in sensors and controlled in closed loop in the actuator layer. Especially for nanopositioning stages with piezoelectric actuator, closed loop in actuator layer can eliminate the hysteresis and creep efficiently which are important sources of errors (≈ 20 % of full stroke). The control in actuator layer is only a local one, which can not guarantee the absolute positioning accuracy in the whole system because no information about relation between two stages is known based only on internal sensors (for example, an internal capacitance sensor in a 1-DoF nanopositioning stage). Therefore, microrobots often have closed loop in actuator layer which guarantee high repeatability, but are unable to identify the aforementioned relationship by themselves. Moreover, closed-loop in actuator layer may not be sufficient because of deficient actuation model and/or indirect measurement. For instance, we use PID control to keep a nanopositioning stage at its zero position (reference position) with internal capacitance sensor. An interferometer can be used as external sensor to measure the real position of the stage. In Fig. 2.8 (a) and (b), there is drift of position up to 400 nm when temperature decreases of 0.35 °C. However, the internal sensor gives us constant information (with 100 nm measuring noises in Fig. 2.8 (c)). Fig. 2.8(d) show that the control input (also the output of the PID controller) of the stage changes somewhat during this time, which means the internal sensor detects a part of the drift and the controller compensate it, but not sufficiently. From internal

sensor point of view, there is no motion; from external sensor point of view, there is a motion. The internal sensor misses the part detected by the interferometer. This is due to the fact that the internal sensor makes indirect measurement which is different from the direct measurement by the interferometer. The source is likely that there is a deformation of the robot structure under temperature change. But the model used to estimate real stage motion based on internal sensor has constant parameters.

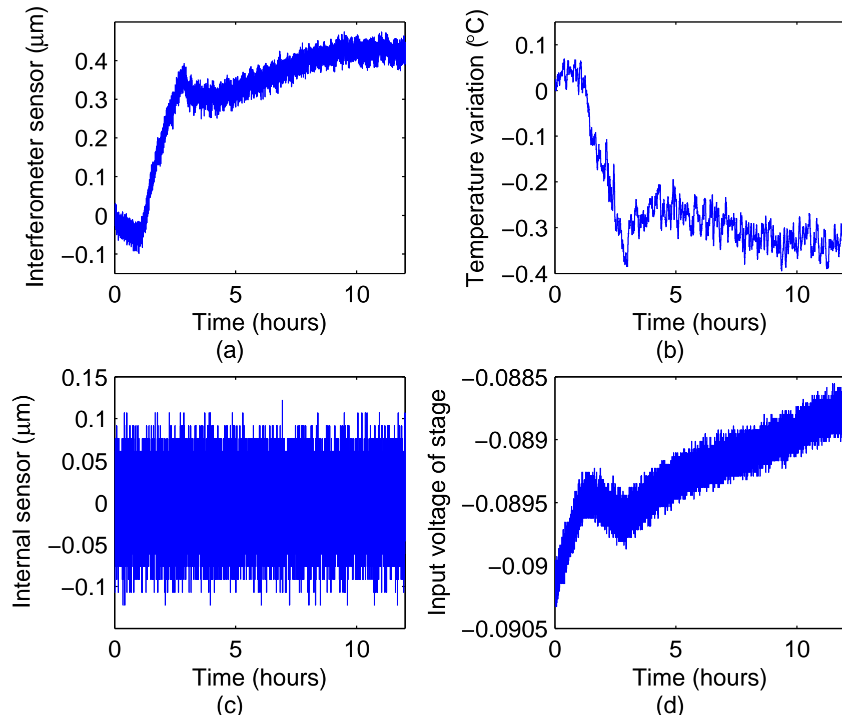

Figure 2.8: (a) Measurement of stage position by interferometer; (b) Measurement of ambient temperature close to the stage; (c) Measurement of internal sensor of the stage; (d) Input voltage of the stage.

2.5.3 Planning layer

In microrobotic systems, closed loop control is a popular manner to perform microtasks. It could be accomplished via a microscope or/and a force sensor integrated at the microscale. Closed loop control possesses many merits. However, there are some drawbacks. First, the exteroceptive sensors are generally bulky and often offer only one or two directions of measurement. Multi-direction of measurement requires to combine several sensors, which is a tough task because of the limited workspace [19]. Moreover, the time and computation cost paid is considerable. For example by visual servo control, image acquisition, feature extraction and other image processing (e.g., subpixel enhancement) introduce non-negligible time delays resulting in low assembly throughput.

Open loop strategy requires good knowledge about system behavior. But it has advantages over closed loop strategy as it uses only driving blocks and/or limit measurement [8, 14]. Comparing to closed loop, open loop strategy does not need sensors in the implementation phase. Positioning speed is faster because of no feedback and convergence processes. In addition, noise in the feedback loop can be avoided. Thus, open loop control is a rational alternative to improve efficiency and accuracy for microtasks. We choose this alternative because many micro-nano robots are used in open loop in planning layer and in closed loop in actuator layer.

2.5.4 Robot calibration

As shown in Fig. 2.9, we choose control strategy of planning-layer-open-loop and actuator-layer-closed-loop. Open loop in planning layer can be fulfilled via robot calibration. Calibration is a process of locating the end-effector of the manipulator in a global coordinate frame with acceptable or improved absolute accuracy by identifying and compensating errors in the control model. The basic idea of robot calibration requires a good model and identification of the model parameters. The whole process of calibration can be divided into four steps as Fig. 2.10:

- Model structure determination (a): First we select the model structure which could be a kinematic model or model-free structure, such as a neural network, etc. The joint variables are q.
- Data acquisition (b): In this step, the microrobotic system is controlled to the defined target points $q = x_t$. The external sensor estimates the real position x_r of the microrobotic system. Some external disturbance factors t, such as temperature, are recorded at the same time.
- Model training/identification (c): Subsequently, all the information including position measurements x_m, target points $q = x_t$, and/or external disturbance t is fed into optimization algorithm, and then the vector of model parameters C is identified.
- Implementation (d): In this phase, the calibrated model is implemented. The control input x_c is calculated using the model combining the identified vector C, new targets q', and real-time measurement of external disturbance t'. Finally, the microrobotic system reaches positions x'_r.

2.6 Conclusions

This chapter discusses the motivations to achieve high accuracy at the microscale. Microtechnology has immersed in a lot of applications in our life. Microrobots are assistants that help us to access microworld. The accuracy of microrobots is the most important criterion determining if the applications of microrobots are successful or not. Depending on different practical cases, the required accuracy would range from several tens of

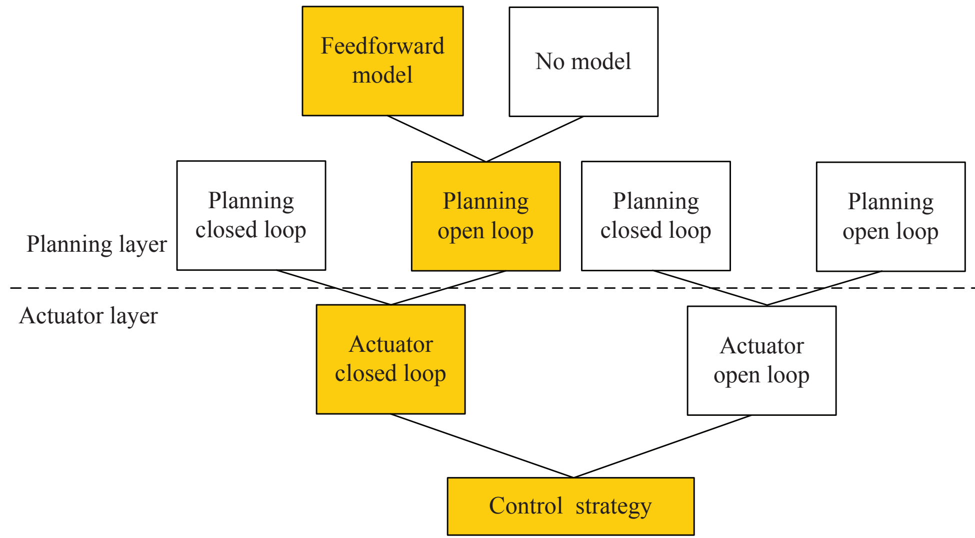

Figure 2.9: Architecture of actuator and planning layers.

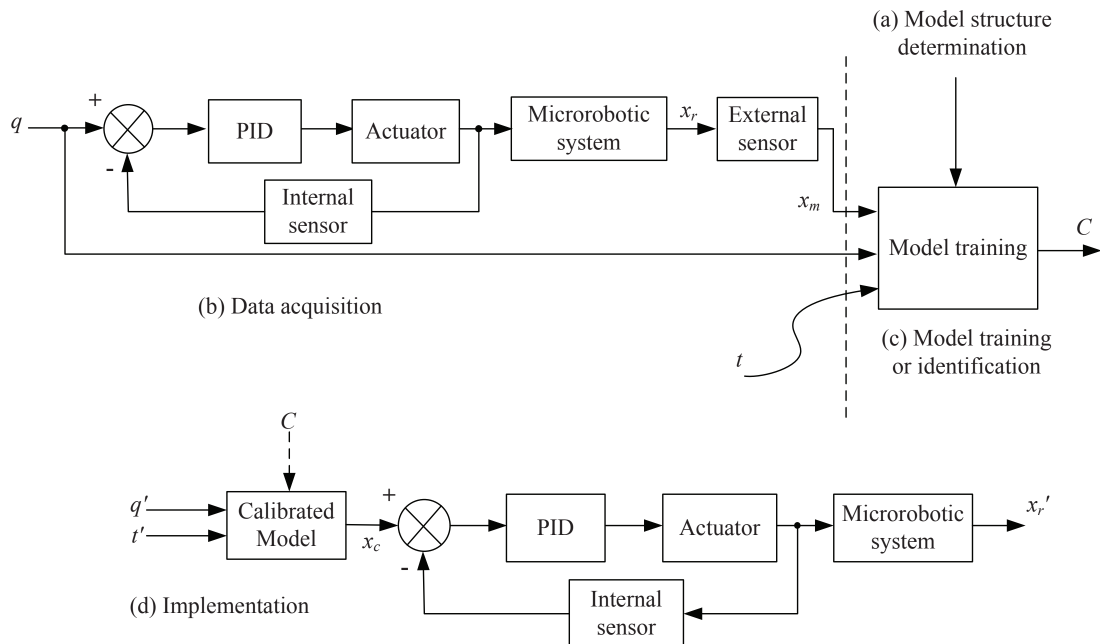

Figure 2.10: Basic principle of robot calibration. Step (a): Model structure determination; Step (b): Data acquisition; Step (c): Model training and parameters identification; Step (d): Implementation of calibration model to the robot.

micrometers to a few nanometers. However, to achieve high accuracy is usually difficult because there are many sources of imperfection affecting the motion of microrobots. Al-

l possible imperfections are discussed and presented, such as assembly error, position- and angle-dependent errors, thermal drift and so on. Before to improve the accuracy, we have to measure the real positions and imperfections of the microrobots using appropriate sensors. The difficulty is the lack of sensors that satisfy all the measuring requirements, such as high accuracy and resolution, suitable range and bandwith, small volume and sensitivity, multi-DoF and so on. This lack induces planing-layer control very complex. In this thesis, robot calibration in open loop is chosen because its advantages over closed loop. Open loop avoids the use of external sensors and feedback convergence when implementing the robot, which is good for enhancing the efficiency.

Chapter 3

State of the Art

3.1 Introduction

Based on the discussions in Chapter 2, our primary direction is to improve positioning accuracy through robot calibration. To go further, this chapter will review the state-of-the-art of accuracy criterion in precision metrics that will be applied to experimental tests to analyze positioning accuracy and repeatability for micro-nano robots. This chapter will also review calibration of macro and micro-nano robots. Among them, we will discuss their modeling methods, considered parameters, used sensors as well as links to our work. This will enable to identify which models could be adapted for micro-nano robot calibration, what sensing solution is today available and adapted and to state which level of accuracy can be attained. Sensing solutions will be presented in terms of micro- and nanopositioning respectively.

3.2 Precision metrics

Precision metrics will be discussed in this section to provide a common way for performance characterization enabling performances comparison. Robot precision is usually characterized by two indices: accuracy and repeatability. These two indices are explicitly defined in international standard ISO 9283 [1] and American national standard ANSI/RIA R15.05 [2]. ISO 9283 and ANSI/RIA R15.05 standards are designed for evaluating the performances of industrial robots [37]. Here, we only introduce standard ISO 9283 which will be partially applied in our work.

3.2.1 ISO 9283 standard

ISO 9283 standard defines the positioning accuracy and repeatability. Fig. 3.1 shows geometric view of the two performance indices.

The position accuracy AP is defined as the difference between the position of a given command pose $O_c(x_c, y_c, z_c)$ and the barycenter $G(\bar{x}, \bar{y}, \bar{z})$ of the attained positions

Figure 3.1: Positioning accuracy AP and repeatability RP. G is the barycenter of attained positions; O_c is the command pose.

(x_i, y_i, z_i) when reaching the command pose from the same direction:

$$AP = \sqrt{(\bar{x}-x_c)^2+(\bar{y}-y_c)^2+(\bar{z}-z_c)^2}, \tag{3.1}$$

where

$$\bar{x} = \frac{1}{n}\sum_{j=1}^{n} x_j, \tag{3.2}$$

$$\bar{y} = \frac{1}{n}\sum_{j=1}^{n} y_j, \tag{3.3}$$

$$\bar{z} = \frac{1}{n}\sum_{j=1}^{n} z_j, \tag{3.4}$$

where $\bar{x}$, $\bar{y}$, and $\bar{z}$ are the coordinates of the barycenter of the cluster of points obtained after repeating the same pose n times.

ISO standard requires to perform n=30 cycles (command the same pose 30 times) for every test. x_c, y_c and z_c are the coordinates of the command pose; x_j, y_j and z_j are the coordinates of the j-th attained pose.

Pose repeatability is defined to express the closeness of agreement between the attained poses after n repeat visits to the same command pose in the same direction. For a given pose, the repeatability RP is expressed by the radius of the sphere whose center is the barycenter.

$$RP = \bar{l} + 3\delta \tag{3.5}$$

with

$$\bar{l} = \frac{1}{n}\sum_{j=1}^{n} l_j, \tag{3.6}$$

$$l_j = \sqrt{(x_j - \bar{x})^2 + (x_j - \bar{y})^2 + (x_j - \bar{z})^2} \tag{3.7}$$

$$\delta = \sqrt{\frac{\sum_{j=1}^{n}(l_j - \bar{l})^2}{n-1}} \tag{3.8}$$

To obtain the pose positions x_j, y_j and z_j, an external measuring system is required.

3.2.2 Other evaluation methods

ISO and ANSI standards are dedicated to industrial robots. They propose a general framework which can be applied to specific application cases, whereas there are some difficulties to apply them to micro-nano robotics. For example, the standards are based on the fact that the measuring system's resolution is much higher than the robot's resolution and the measuring errors could be neglected which is true in macrorobotics. However, in micro-nano robotics, measuring uncertainty can not be ignored because the resolution of sensors is closed to the resolution of micro-nano robots. Some researchers thus proposed their own criteria to characterize accuracy and repeatability.

D. Popa *et al.* [65] proposed a new precision metric to redefine repeatability and accuracy. This new metric combines the sensor (used for performance evaluation) position and measurement uncertainty into accuracy and repeatability. For accuracy test, the robotic system is commanded to place the end-effector at a designated position in 3-dimensional space. The error distribution with respect to the sensor gives the measure for accuracy. The difference between this proposed approach and the standard one is that the conventional accuracy is a mean value, not a distribution. For the repeatability test, the robotic system is commanded to place the end-effector alternatively between two predefined but arbitrary points in 3-dimensional space. The error distribution with

respect to the sensor gives the measure for repeatability. A notable advantage of the metrics is the consideration of measuring uncertainty from the sensor. This is meaningful because every kind of sensor has its specific measuring uncertainty which means performances evaluated by different sensors are different.

Paying attention to the maximum position error, Jean-François Brethé [11] proved that neither the pose repeatability nor the accuracy are adequate to calculate such error. The author proposed a granular stochastic modeling method which combines spatial resolution and actuators' repeatability. The granulous space modeling was introduced to depict the workspace which has holes, aggregates, and hyperredundant areas in the micrometric structure. The granulous paradigm enables the determination of the maximum position error at the microscale. In our work, maximum position error is not what we concern, instead we focus on average positioning error which is represented by ISO accuracy.

3.2.3 Metrics used in this thesis

In ISO 9283, the definitions of repeatability and accuracy are formulated. However, positioning performances depicted in literature are usually with different criteria and named in different ways, such as absolute errors, positioning errors, accuracy, MSE and so on. This makes comparison and reference difficult. Moreover, there is no clear formulation analysis to distinguish the different error components induced by different sources. We seek to unify the calculation of positioning performance and express the role of different components in virtue of the calculation methods of ISO 9283. Besides, we will evaluate the measuring uncertainty in the next section.

Without lost of generality, the following calculation and analysis will be based on 1-DoF case which is easy to expand to multi-DoF. For example, for a 1-DoF nanopositioning stage, given the target input x_T, the real position measured by the external sensor is x_m and defined by:

$$x_m = G(x_T) + L(t) + S, \tag{3.9}$$

where $G(x_T)$ is the latent geometric model depicting the real displacement; $L(t)$ is the drift from environment (we will consider thermal effect) acting on the nanopositioning stage; S is the measuring uncertainty of the external sensor. Expending $G(x_T)$, we have

$$x_m = P(x_T) + x_T + g(x_T) + L(t) + S, \tag{3.10}$$

where $P(x_T)$ is the error component inherent in the nanopositioning stage; $g(x_T)$ is the position-dependent error corresponding to joint input x_T. $P(x_T)$ is named intrinsic error which cannot be compensated. This error results from the control precision of actuator layer which is affected by controller capability and resolution of internal sensor. $P(x_T)$ can also be minimized by design, fabrication and setting. And $g(x_T)$ can be minimized by robot calibration. Fig. 3.2 shows the geometric representation of every component of input-output of the 1-DoF nanopositioning stage. S can be minimized by use of adequate sensor and measurement procedure which are not easy at the microscale. Except for that,

the thermal drift due to the thermal expansion of the material of sensor head and the table are rest parts of S.

In this chapter, S has been minimized through sensor selection and preliminary experiments, and is neglected in the followings. So, the Eq. (3.10) becomes

$$x_m = P(x_T) + x_T + g(x_T) + L(t). \tag{3.11}$$

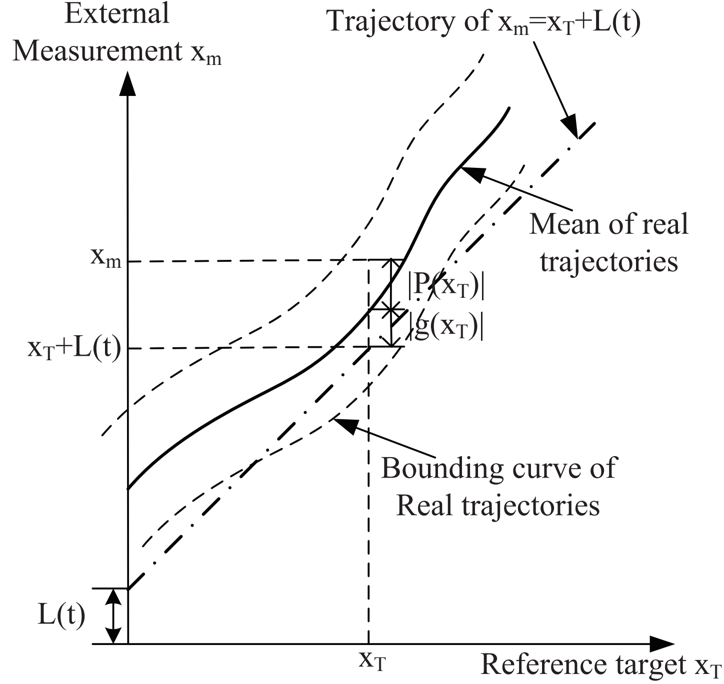

Figure 3.2: Geometric representation of all input-output components of the 1-DoF nanopositioning stage.

Accuracy and repeatability without external disturbances

Without considering external disturbances $L(t) = 0$, we define the following remark regarding the accuracy and repeatability.

Remark 1: Without external disturbances, the accuracy of the micropositioning stage is determined by geometric error and intrinsic errors; the repeatability called intrinsic repeatability is determined absolutely by intrinsic errors.

Exploiting the intrinsic characteristics, the external disturbances will be ignored, so the measured pose can be expressed by:

$$x_m = G(x_T) = P(x_T) + x_T + g(x_T) \tag{3.12}$$

For a given pose, the accuracy expresses the deviation between the reference target x_T and the mean of a set of measured poses $\overline{x_m} = \frac{1}{n}\sum_{i=1}^{n} x_{mi}$ when reaching the target n times. The 1D accuracy can be calculated according to ISO 9283:

$$\begin{aligned} AP_I &= |\overline{x_m} - x_T| \\ &= \left|\frac{1}{n}\sum_{i=1}^{n} x_{mi} - x_T\right| \\ &= \left|\frac{1}{n}\sum_{i=1}^{n} G_i(x_T) - x_T\right| \\ &= \left|\frac{1}{n}\sum_{i=1}^{n} P_i(x_T) + g(x_T) + x_T - x_T\right| \\ &= \left|g(x_T) + \frac{1}{n}\sum_{i=1}^{n} P_i(x_T)\right| \end{aligned} \tag{3.13}$$

The repeatability expresses the closeness of agreement between n measured poses as:

$$\begin{aligned} RP_I &= \frac{1}{n}\sum_{i=1}^{n} |x_{mi} - \overline{x_m}| + 3\sigma_I \\ &= \frac{1}{n}\sum_{i=1}^{n} \left|G_i(x_T) - \frac{1}{n}\sum_{j=1}^{n} G_i(x_T)\right| + 3\sigma_I \\ &= \frac{1}{n}\sum_{i=1}^{n} \left|P_i(x_T) + x_T + g(x_T) - \frac{1}{n}\sum_{j=1}^{n} P_i(x_T) - x_T - g(x_T)\right| + 3\sigma_I \\ &= \frac{1}{n}\sum_{i=1}^{n} \left|P_i(x_T) - \frac{1}{n}\sum_{j=1}^{n} P_i(x_T)\right| + 3\sigma_I \end{aligned} \tag{3.14}$$

where σ_I is the standard deviation. From Eq. (3.14), it can be seen that the repeatability RP_I comes from the intrinsic part $P(x_T)$ of the stage. We call this repeatability as intrinsic repeatability.

Accuracy and repeatability with external disturbances

Remark 2: When subjected to external disturbances, the accuracy of the micropositioning stage is degraded by geometric error, intrinsic errors, and external errors; the repeatability is a combination of intrinsic part and extrinsic part represented by external drift.

Similar to Remark 1, positioning accuracy can be calculated through:

$$\begin{aligned} AP_E &= \left| \frac{1}{n}\sum_{i=1}^{n} x_{mi} - x_T \right| \\ &= \left| g(x_T) + \frac{1}{n}\sum_{i=1}^{n} P_i(x_T) + \frac{1}{n}\sum_{i=1}^{n} L_i(t) \right| \end{aligned} \tag{3.15}$$

$$\begin{aligned} RP_E &= \frac{1}{n}\sum_{i=1}^{n} |x_{mi} - \overline{x_m}| + 3\sigma_E \\ &= \frac{1}{n}\sum_{i=1}^{n} \left| P_i(x_T) - \frac{1}{n}\sum_{j=1}^{n} P_i(x_T) + L_i(t) - \frac{1}{n}\sum_{j=1}^{n} L_i(t) \right| + 3\sigma_E \\ &\leq \frac{1}{n}\sum_{i=1}^{n} \left| P_i(x_T) - \frac{1}{n}\sum_{i=1}^{n} P_i(x_T) \right| + \frac{1}{n}\sum_{j=1}^{n} \left| L_i(t) - \frac{1}{n}\sum_{j=1}^{n} L_i(t) \right| + 3\sigma_E \end{aligned} \tag{3.16}$$

Therefore inside the sign of absolute value in Eq. (3.16), $P_i(x_T) - \frac{1}{n}\sum_{j=1}^{n} P_i(x_T)$ is the part composed by intrinsic repeatability; $L_i(t) - \frac{1}{n}\sum_{j=1}^{n} L_i(t)$ is the part composed by thermal drift, which is extrinsic repeatability. Extrinsic repeatability comes from external disturbances and changes somehow with external sources.

Accuracy and repeatability with calibration

With calibration, $q = x_T + g'(x_T) + L'(t)$ replaces x_T as control input

$$\begin{aligned} x_m &= G(q) + L(t) \\ &= g(q) + P(q) + q + L(t) \\ &= g(x_T + g'(x_T) + L'(t)) + P(x_T + g'(x_T) + L'(t)) + x_T + g'(x_T) + L'(t) + L(t) \end{aligned}$$

where $g'(x_T)$ and $L'(t)$ are additional inputs for compensating geometric and thermal errors respectively.

In reality, $g'(x_T)$ and $L'(t)$ are small, e.g. $g'(x_T)$<0.4 μm and $L'(x_T) \leq 5\mu m$ in a nanopositioning stage. Therefore, $g(x_T + g'(x_T) + L'(t)) \approx g(x_T)$ and $P(x_T + g'(x_T) + L'(t)) \approx P(x_T)$. Moreover, because $g(x_T)$ is relatively simple and steady, the hypothesis of perfect compensation of geometric error is strong, namely $g'(x_T) = -g(x_T)$. Then,

$$\begin{aligned} x_m &= g(x_T) + P(x_T) + x_T + g'(x_T) + L'(t) + L(t) \\ &= P(x_T) + x_T + T(t) \end{aligned}$$

If the compensation of thermal model is perfect, $T(t) = 0$, then $x_m = x_T + P(x_T)$.

Remark 3: When subjected to external disturbances, the accuracy of the micropositioning stage using calibration is degraded by intrinsic errors and residual errors of

imperfect compensation based on the assumption of complete compensation of geometric error; the repeatability is a combination of intrinsic part and extrinsic part represented by residual drift.

Similar to Remark 1 and Remark 2, we have

$$\begin{aligned} AP_S &= \left| \frac{1}{n} \sum_{i=1}^{n} x_{mi} - x_T \right| \\ &= \left| \frac{1}{n} \sum_{i=1}^{n} P_i(x_T) + \frac{1}{n} \sum_{i=1}^{n} T_i(t) \right| \end{aligned} \tag{3.17}$$

$$\begin{aligned} RP_S &= \frac{1}{n} \sum_{i=1}^{n} |x_{mi} - \overline{x_m}| + 3\sigma_C \\ &= \frac{1}{n} \sum_{i=1}^{n} \left| P_i(x_T) - \frac{1}{n} \sum_{j=1}^{n} P_i(x_T) + T_i(t) - \frac{1}{n} \sum_{j=1}^{n} T_i(t) \right| + 3\sigma_C \end{aligned} \tag{3.18}$$

Summary

Repeatability can be divided into two types, intrinsic repeatability and extrinsic repeatability. Intrinsic repeatability is the characteristics of the stage itself and is only relevant to geometric nature of the microrobot and controller capability. Extrinsic repeatability is the summation of intrinsic repeatability and the portion affected by external environment.Intrinsic repeatability is relatively stable and extrinsic repeatability changes with external factor (temperature in this case). In general, the deviation of temperature is wider, the extrinsic repeatability is larger. In the same condition of temperature changing, the repeatability with thermal compensation is greater than that of no compensation. The final accuracy and repeatability are determined by the maximum values of tests with M testing poses:

$$AP = max(AP_i), i = 1, 2, \ldots, M;$$

$$RP = max(RP_i), i = 1, 2, \ldots, M.$$

3.3 Calibration of macrorobotic systems

Robot calibration has been extensively investigated over 30 years. Most of these works can be classified into two categories based on modeling: model-based and model-free methods [3]. Their main difference is whether using kinematic modeling or not.

Model-based method involves systematic approaches establishing the relationship between joint angles and end-effector position with respect to a global frame. The relative transformation between each two joints is clearly depicted with mathematical equations. The most often used modeling approach is Denavit-Hartenberg (DH) parameterization.

However, the error models based on DH convention are not continuous when consecutive joint axes are parallel or almost parallel. To remedy this drawback, some modified DH methods were proposed, such as the Hayati *et al* models, Veitschegger and Wu's model, Stone and Sanderson's S-model. Zhuang *et al* proposed a Complete and Parametrically Continuous (CPC) model [96]. Most of these modeling methods use *ad hoc* kinematic representations which usually produce complicated expressions. Product-of-Exponentials (POE) formula is a more general representation eliminating *ad hoc* expressions and possessing singularity-free feature [63, 52, 32, 85]. Expect for these advanced methods, there are another method based on vectors (3×3 matrices) or homogeneous matrices (4×4 matrices) [6], which are suitable for simple cases modeling and will be applied in our case study.

Due to structural complexity of many multi-DoF robots, alternative modeling adopts model-free method instead of modeling explicitly different sources of imperfections. The commonly used model-free methods are multivariate polynomials, bilinear and cubic spline interpolations, Artificial Neural Networks (ANN), or fuzzy logic [4]. Model-free methods have advantages of simplicity and effectiveness in small workspace. However, because there is no semantic relationship between model parameters and physical properties of the data to be approximated, it works like a black-box.

As mentioned in Chapter 2, one of our objectives is to understand the imperfection behavior and to quantify the influences of imperfections to the microrobots. Therefore, model-based calibration is more suitable than model-free one. To do that, we will need to express all the considered imperfections in a unified kinematics model. In model-free approach, interpolation techniques are used to calculate the errors on the poses not measured [5, 4]. These techniques can also be used to estimate the position- and angle-dependent errors on the poses not measured. Therefore, combining the kinematic model with the interpolation techniques would be helpful to improve the model-based calibration. This idea will be applied in calibration of our microrobotic systems.

The most commonly considered imperfections are errors on joint offset, link length, link offset and link twist, which correspond to the four parameters associated with every link of a robot in DH-convention. Calibration of these errors are performed with two kinds of methods. One kind of methods require external sensor to measure the robot end-effector pose. The most commonly used sensors are coordinate measurement machine (CMM) [25] and laser tracking system [86]. Another kind of methods imposes some constraints on the end-effector or joints by some lock mechanisms. An automated method was proposed to calibrate joint offset of industrial robot based on single-point constraint approach using position sensitive detectors (PSD) [51]. Another method was based on tracking a laser line in the robot workspace [17]. The robot joint angles were recorded during the tracking and then used for estimating the robot zero offset.

The calibration in [41] made use of the motorized prismatic joint positions corresponding to some sets of configurations where in each set either a passive universal joint or a passive spherical joint is fixed using a lock mechanism. Robot calibration with planar constraints was proposed in [95]. It first showed that a single-plane constraint is normally not sufficient to calibrate a robot. It is also proven that by using a three-plane

constraint, the constrained system is equivalent to an unconstrained point-measurement system under certain conditions.

Recently, vision-based metrology became a powerful tool in robot calibration. A proposed algorithm required a ground-truth scale in the reference frame and assumed that there was a camera is rigidly attached to the robot end-effector, which made it possible to obtain the pose of the robot with the pose of the camera [60]. By designing a robot movement trajectory, the camera poses can be estimated up to a scale factor at each configuration with the factorization method, where a nonlinear least-square algorithm is applied to improve its robustness. The great advantage of this proprioceptive method was that only image sequences of a calibration object and a ground-truth length are needed, which made the robot calibration procedure more autonomous in a dynamic manufacturing environment. Exteroceptive sensing using vision was adapted for calibration of parallel robots [71, 70]. In [71], the need for accurate calibration target was suppressed. A novel approach was proposed for observation of parallel robot legs with a camera. The vision-based methods are low-cost and flexible, however, it is very difficult to apply and integrate vision systems with sufficient range and resolution in microrobots. Except for the four DH parameters, [56] and [68] included two further parameters describing distortions of the motion axis from its ideal orientation in the kinematic model and modeled them as two rotations performed before the joint angle rotation.

Flexibility on joints and links is a hot topic in robot calibration in recent years. Compared to the above-mentioned constant parameters, elastic deformation is much more difficult to model and compensate. The calibration and compensation of flexibility involve elasticity modeling, spring constant, the location of the mass center of each link, the mass of the links, the joint configurations. A model of harmonic drive stiffness was developed through a controlled loading experiment [79]. The stiffness component of joint torque on a manipulator was modeled as a function of the applied load [40]. Authors in [36] and [59] used a set of generalized error functions unifying geometric and elastic errors but did not identify physically meaningful parameters. Khalil and Besnard recently developed a nonlinear least-squares method to calculate physically meaningful geometric and flexibility parameters [42]. A flexible model describing the PPS (Patient Positioning Systems) was developed [39]. This model took into account the most significant structure distortions, and the model parameters had a physical meaning. Lightcap et al. defined a flexible geometric model including cubic spring coefficients [49]. The flexibility in the harmonic drive transmission was modeled with the torsional spring model. Four methods were presented for the identification of the inertial parameters of the load of a manipulator [45]. The knowledge of the values of these parameters can be used to tune the control law parameters in order to improve the dynamic accuracy of the robot. These works all modeled systematically the flexibility with a limited number of coefficients and identified such coefficients using optimization algorithms. The flexibility errors are load-, position-, and angle-dependent which will also be encountered in microrobotic systems. However, the position- and angle-dependent errors at the microscale normally can not be modeled with limited numbers of coefficients. This is because, at the microscale, the main influence sources of such errors comes from the actuation system and fabrication instead of gravity load, which makes behavior too complex to model.

Temperature is also a major cause affecting positioning accuracy in micro-nano positioning. There have been a lot of works about real-time thermal compensation for machine tools. [18] applied and compared multiple regression analysis and artificial neural network for calibration of machine tools. An approach based on Gaussian integration technique was proposed for modeling thermally induced errors and selecting optimum temperature locations [46]. In [94], thermal modal analysis was utilized for the temperature sensor placement determination and robust thermal error modeling for CNC (Computer Numerical Control) machine tools. Zhao et al. [91] simulated the thermal deformation of a CNC spindle and calculated the thermal error using finite element method. Fraser et al. [28] developed expressions for the generalized transfer functions of the thermal, and thermal deformation response of the machine tool structure. Thermal compensation was also tackled on industrial robot [30]. Principal component analysis was used to find the temperature vector containing most information of the thermal-induced errors, and thermal error models was established using orthogonal regression methods.

3.4 Calibration of microrobotic systems

Comparing with macrorobotics, calibration of microrobotics is rarely studied. With the fast development of microrobotics during the last decades, research about calibration of microrobots is getting more and more attention. To fulfill micromanipulation tasks, microrobotic systems usually need to get help from calibration to improve the positioning accuracy.

3.4.1 Works without considering thermal compensation

A simple calibration scheme [21] was proposed based on linear interpolation of a set of taught benchmarks. M_1 and M_2 were micropositioners with grippers and M_3 was the micropositioner with a MEMS die (Fig. 3.3 (a)). The end-effector of M_1 or M_2 was controlled to point to reference points at M_3 and its three joint coordinates are recorded (Fig. 3.3 (b)). Using these data, the transformation or mapping between joint coordinates in the robot frame and die coordinates in the global frame was calculated based on linear interpolation (Fig. 3.4). Two sets of information were provided by internal and external sensor respectively. After calibration, the micropositioners were controlled to perform out-of-place assembly to arbitrary desired locations on the MEMS die held by M_3. The average positioning error using calibration was better than 4 μm.

A procedure (Fig. 3.5) of calibration and the application was presented in [65]. A schematic diagram of the relative position of several local/global frames is shown in Fig. 3.6. First the tilt angle was manually adjusted in order to guarantee that end-effectors were vertical enough to pick up all parts. The paper illustrated the calibration method by finding the transformation from world frame into R_1 frame, and then into the gripper tool manipulator R_2 frame. The calibrated microrobotic system fulfilled the task of aligning the MEMS die to the carrier with error 35 μm.

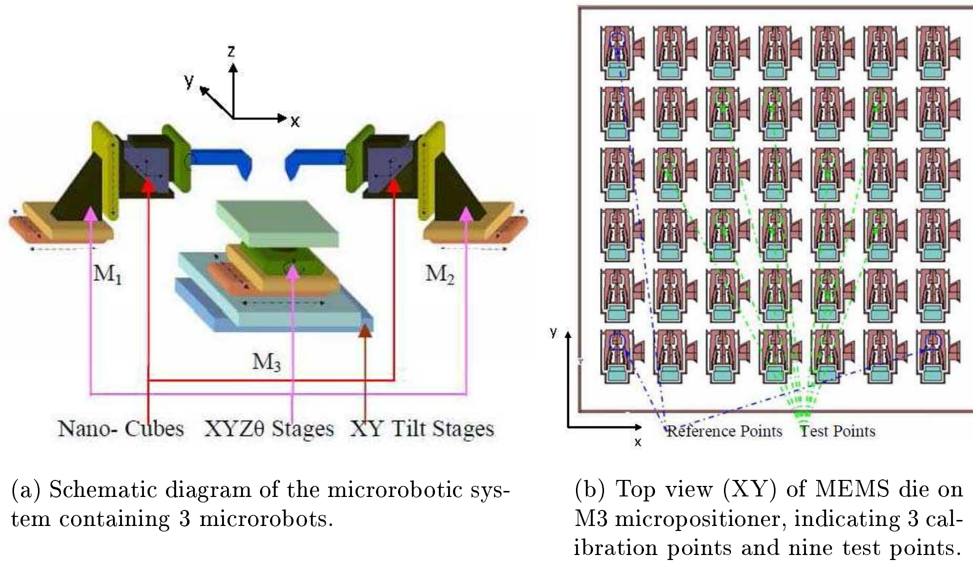

(a) Schematic diagram of the microrobotic system containing 3 microrobots.

(b) Top view (XY) of MEMS die on M3 micropositioner, indicating 3 calibration points and nine test points.

Figure 3.3: Schematic diagram of the experimental setup [21].

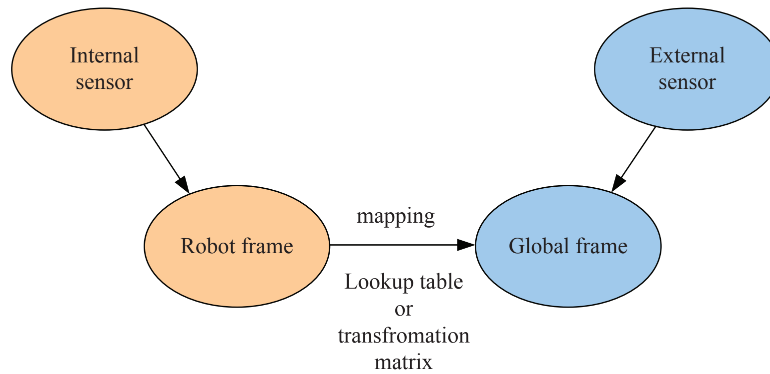

Figure 3.4: Schematic diagram of mapping from robot frame to global frame.

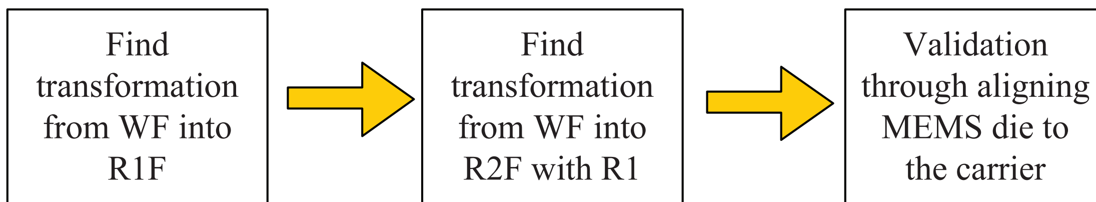

Figure 3.5: Schematic diagram of calibration process in [65].

A hybrid scheme [58] was proposed combining open loop calibration and closed loop visual servoing. As shown in Fig. 3.7, the robot-camera calibration was performed

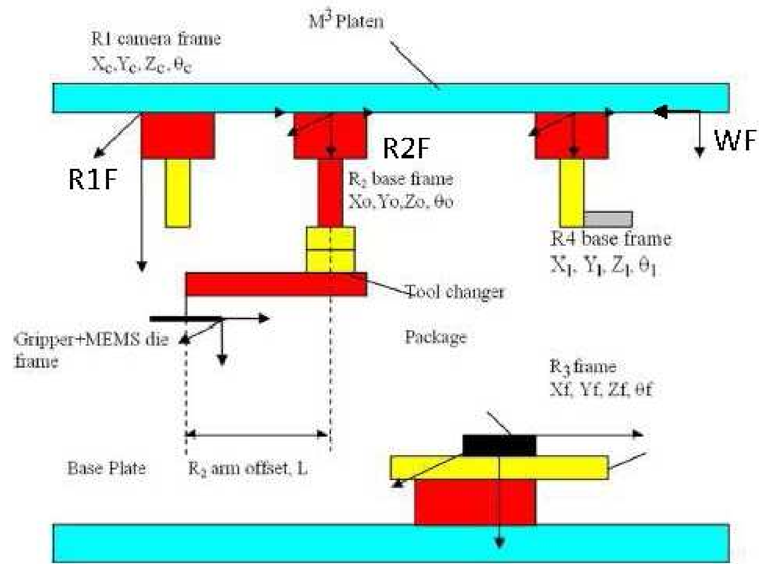

Figure 3.6: Coordinate frames assignment for micromanipulators in [65]

first, and then problems related to tool position drift were dealt using continuous recalibration. Fine positioning was achieved through visual servoing. Here, calibration and recalibration were used for coarse positioning which brought the micropipette inside the field-of-view of the camera. For the task of reaching over 300 targets in a workspace 400×300 μm, the average positioning error was achieved 5.65 μm using calibration and 1.75 μm using recalibration.

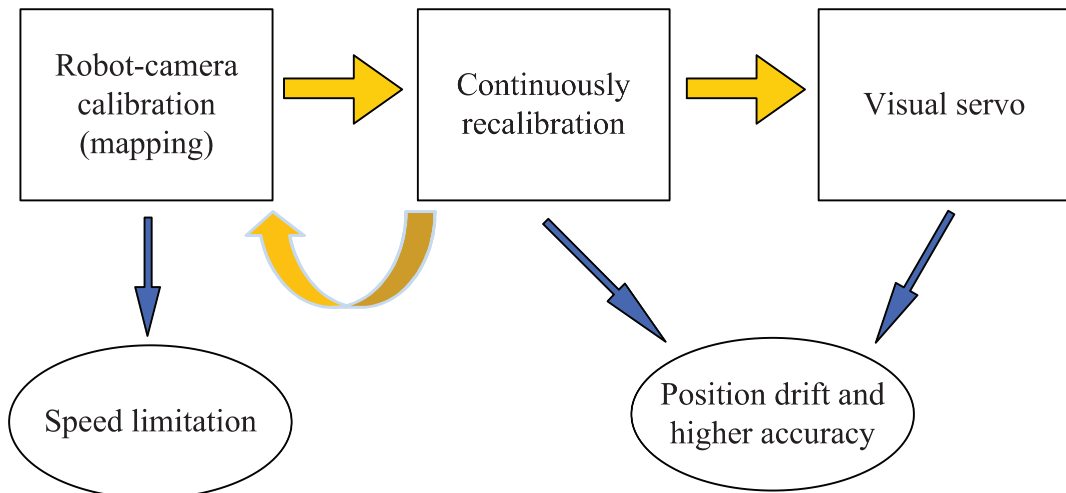

Figure 3.7: Schematic diagram of calibration process in [58].

Similarly, [64] used a solution which relies on approximation to create a lookup table between the world frame and image frame. Fig. 3.8 shows that the end-effector was manually brought to the corner of the field-of-view of the camera by teleoperation. The microrobot was controlled to move with joint coordinate (X_i, Y_i), and (x_i, y_i) was recorded concurrently in image frame. The transformation between (X_i, Y_i) and (x_i, y_i) was constructed using least square fitting. For validation, three tests (Fig. 3.9) of particles manipulation were preformed to construct a line, a cross, and a "W". Average positioning errors between targets and real positions are less than 1 μm in three tests (Table 3.1).

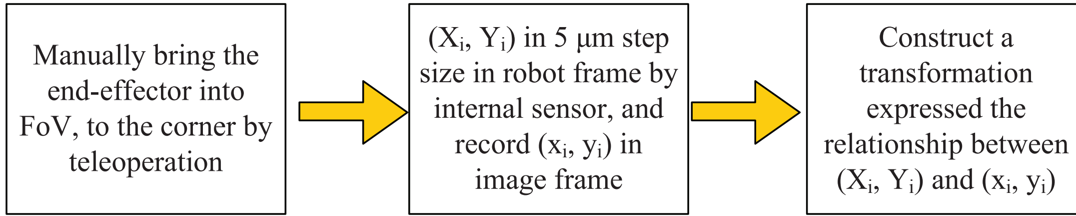

Figure 3.8: Schematic diagram of calibration process in [64].

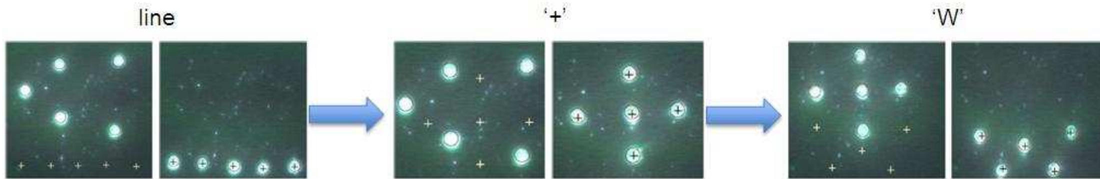

Figure 3.9: Experimental results of aligning the particles in a line, a cross, and a "W" after calibration [64].

Table 3.1: External sensors for position measurement at the microscale [64].

Experiment	Average error ϵ	Minimum error	Maximum error
1. line	0.35 μm	0.18 μm	0.71 μm
2. cross	0.39 μm	0.25 μm	0.63 μm
3. W	0.53 μm	0.13 μm	0.97 μm

3.4.2 Works with thermal compensation

As discussed in Section 3.3, there have been numerous works concerning large-sized and macropositioning robots or machine tools with thermal compensation.

In the condition of indoor temperature, drift of the nanopositioning stage can reach a few microns, which is not acceptable in many applications [58]. For example, the thermal drift of a 5 cm long aluminium bar can reach 1.2 μm while temperature changes

1 °C. However, microrobots should guarantee accuracy within submicron range when operating in uncontrolled environment where complex and nonlinear disturbances occur from everything (robot, measuring instruments, nearby devices, ...). One solution to wipe off temperature influence is using thermal-isolation or stabilization equipments to keep temperature stable within the workspace.

[27] carried out the measurement in a chamber inside which the measuring environment was protected against thermal perturbations. The temperature was stabilized within less than $\pm 0.1°C$. To investigate the influence of environmental conditions on microassembly, the experimental setup was put inside an environment controlled station in [92]. However, appropriate devices are not easy to get in the context of micro and nanoscale. Even in clean room (an environment more steady than normal labs), temperature variation is sufficiently large (±1 to ±2 °C) to affect the reference position and induce inaccuracy in micrometer range. To achieve submicron accuracy, these temperature drift can not be ignored in a temperature changing environment.

An ultra-high-precision linear axis was calibrated while thermal effects acting on it in [55]. The model is:

$$q = \alpha_1 x^2 + \beta_x + \gamma + a_1 T1 + \ldots + a_{10} T_{10}, \tag{3.19}$$

where α, β and γ are coefficients, while $a_1, \ldots, a_{10}$ are thermal coefficients. A few thermocouples were attached on some locations of the setup (Fig. 3.10) to measure the temperature. The calibration procedure is: First, they took data sets $S1$ and $S2$ using interferometer. Second, $S1$ is used for training the model and the parameters can be obtained. Finally $S2$ was used to check the extrapolation of the model. Hence, actually the validation is the fitting performance of the model rather than the real performance implementing the model. Further experiment must be performed by implementing the calibrated model so that the real performance will be known.

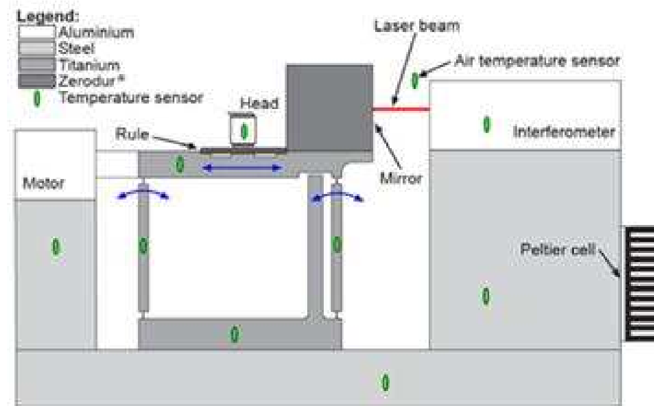

Figure 3.10: Schematic diagram of experimental setup for calibration of ultra-high-precision linear axis [55].

In [54], calibration was performed for Agietron Micro-Nano robot (Fig. 3.11). A model was developed to compensate geometric and thermal effects. Similar to the one

in [55], the model for axis i, $i = x, y, z$ is:

$$q_i = \text{Geometric model} + b_1T1 + \ldots + b_7T_7, \tag{3.20}$$

where q_i is the motor coordinate of axis i, $i = x, y, z$; $b_1, \ldots, b_7$ are thermal coefficients. The Geometric model is much complex than that of single axis:

$$\begin{aligned} \text{Geometric model} &= a_{1i}x + a_{2i}y + a_{3i}z + a_{4i}x^2 + a_{5i}y^2 + a_{6i}z^2 + a_{7i}xy + a_{8i}xz + a_{9i}yz \\ &+ a_{10i}x^3 + a_{11i}y^3 + a_{12i}z^3 + a_{13i}xyz + a_{14i}x^2y + a_{15i}x^2z + a_{16i}y^2x \\ &+ a_{17i}y^2z + a_{18i}z^2x + a_{19i}z^2y + a_{20i}, \end{aligned} \tag{3.21}$$

where $a_{1i}, \ldots, a_{20i}$ are geometric parameters of axis i, $i = x, y, z$. Validation was performed to evaluate the final positioning performance of the end-effector. Different from [55], the validation data set $S2$ was taken after calibration (Fig. 3.12). The final positioning error is ±100 nm in reaching 94 positions. The calibrated performance was good in 50 minutes of validation. Temperature of the robot during training step changed from 20 °C to 22.5 °C approximately. However, there was no temperature in the validation step presented.

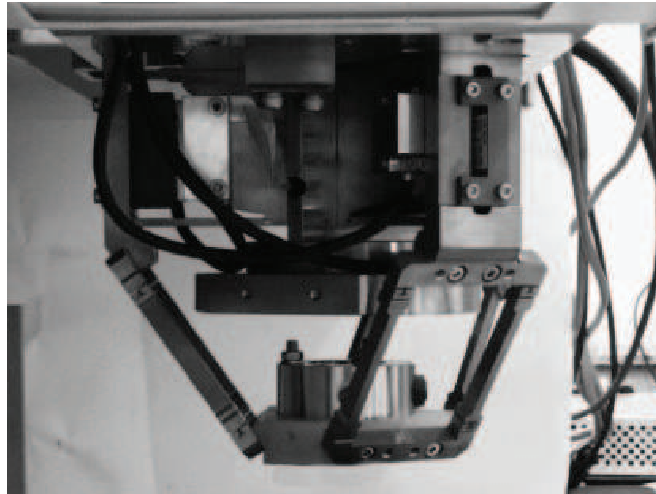

Figure 3.11: Agietron Micro-Nano robot [54].

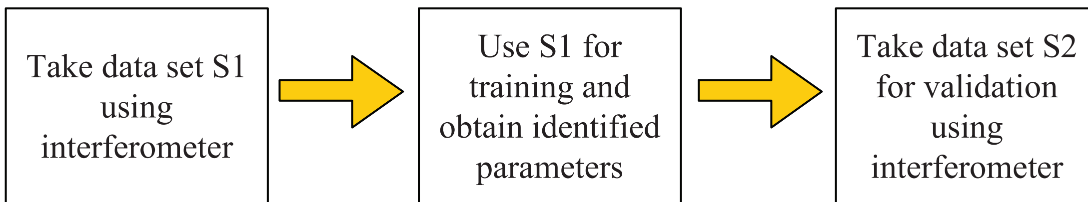

Figure 3.12: Schematic diagram of mapping from robot frame to global frame.

3.4.3 Summary

The above reported works concerning calibration of micro-nano robotic systems are summarized in Table 3.2. We classify them into two groups based on considering thermal compensation or not.

Table 3.2: Calibration of micro-nano robotic systems.

		Robot	DoF of robot	Model	Imperfection	External sensor	Positioning errors after calibration
I	Das07 [21]	Micro-Nano stages	3	linear interpolation	geometric	vision	$< 4\ \mu m$
	Pop09 [65]	Micro stage	3	kinematic	geometric	vision	$35\ \mu m$
	Mat09 [58]	Micro stage	2	mapping	geometric	vision	$5.65\ \mu m$
	Paw06 [64]	Nano stage	2	mapping	geometric	vision	$\approx 0.5\ \mu m$
	Zha08 [90]	Nano stage	2	mapping	geometric	vision	$2\ \mu m$
II	Lub11 [54]	Agietron Micro-Nano robot	3	Polynomial	geometric + thermal	interferometer	$\pm$ 100 nm

Group I is about calibration of micro-nano robotic systems used in micromanipulation platforms. Works in [21, 58, 64, 90] all deal with seeking direct transformation between robot joint coordinates and object coordinates in image frame. These methods are simple and easy to implement. However, they are somehow like a black box or semi-black box from which we have no ideal about the detail behavior of the robots. Even though [65] gave the kinematic model of the microrobotic system, it did not consider the modeling of some higher order imperfections, such as position-dependent and angle-dependent errors. To better depict the behavior of microrobotic systems, we should use model-based method and take into account all or most important imperfections.

Group II is about calibration of an ultra-high-precision industrial robot with thermal drift compensation. To achieve high accuracy up to nanometer range, thermal drift is an inevitable factor. Work in Group II proposes calibration models including thermal drift compensation for ultra-high-precision robots. However, [54] did not provide long term examination of robustness and repeatability performance. To push further the research, we will investigate the thermal compensation in the long term by implementing the calibrated model, and study about repeatability in thermal compensation.

3.5 Sensing solutions

As stated in chapter 2, sensing is difficult to satisfy all the requirements at the microscale. There is a lack of commercially available device providing adequate resolution, accuracy, and range for microscale. Therefore, research is making every effort to fulfill sensing requirements at the microscale. In this thesis, the micro and nano stages involved have already been controlled in closed loop with internal sensors. Therefore, we concentrate on open loop control with external sensing. A vision system working with particular pattern

and algorithm developed in AS2M, Femto-st is chosen for micropositioning measurement. Laser interferometers are selected for nanopositioning measurement.

3.5.1 Sensor for micropositioning

A novel measuring system was proposed for absolute position measurement and the retrieval of an area of interest under microscope [89, 75, 88]. The system consists of a normal video camera, a microscope lens, an objective with $10\times$ magnification and a micro-pattern with a specific design. This pattern is encoded with 2-D binary numbers which is distinct from the commonly used calibration patterns in vision system. The representation of this binary code using the pseudo-periodic distribution of dots enables absolute position (x and y) and orientation (Θ) retrieval from any view of a local zone of small dimensions observed by the vision (Fig. 3.13) with respect to the whole encrypted pattern in both position and orientation. The processing algorithm (Pseudo-Periodic Pattern or PPP algorithm) possesses high range-to-resolution rate ($\approx 10^5$) where the measuring range depends only on the size of the pattern and the high resolution is achieved using the phase measurement of the grid. About the fabrication of the pattern and the algorithm, one can refer to [88] for more details. There are two parts of the algorithm. The first part involves linear processing and provides a very fine positioning of the periodic frame with respect to the pixel frame of the camera. The second part involves binary processing for bit value identification and LFSR (Linear Feedback Shift Registers) sequence reconstruction and decoding. The overall procedure is shown in Fig. 3.14 and the detailed steps are as follows:

- Step 1: Images of local areas of the pattern are recorded.
- Step 2: The images are processed with Fourier Transform (FT). A spectrum composed of a few lobes is obtained where two of them are representative of the periodical fringes that contain the information about the vertical and horizontal position of the PPP.
- Step 3: Such lobes are filtered by a band-pass filter.
- Step 4: Inverse Fourier transform is executed for these filtered lobes and the phases relative to the vertical and horizontal directions are obtained.
- Step 5: The wrapped phases are unwrapped then.
- Step 6: After phase unwrapping, least square fitting is used to obtain the phase planes which is linear with respect to the pixel frame.
- Step 7: The PPP is binarized by distinguishing the absent dots from the present ones by means of thresholding the wrapped phase obtained in Step 4.
- Step 8: The encrypted binary code is extracted and bits are obtained from which we decrypt the bi-dimensional pseudo-random sequences.

- Step 9: From the obtained sequences, reference and shifted lines are then decrypted which values lead to a coarse absolute position.
- Step 10: Finally, the fine measurement obtained at step one is compensated with the coarse measurement from step two in order to obtain the corresponding (x, y, θ) high-accurate absolute coordinates of the zone under view.

Figure 3.13: Image of a local area of Pseudo-Periodic Pattern (PPP) where every dot is 2 μm in diameter.

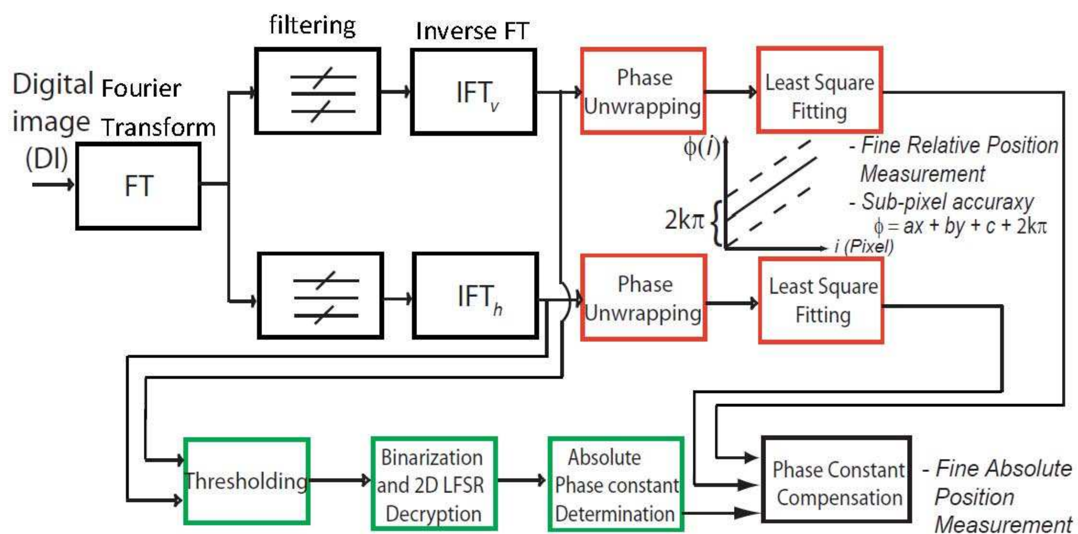

Figure 3.14: Schematic diagram of absolute position retrieval procedure [88].

This PPP algorithm possesses high resolution which is below 10 nm. In this thesis, we employ such algorithm to measure the motion of the microrobotic system.

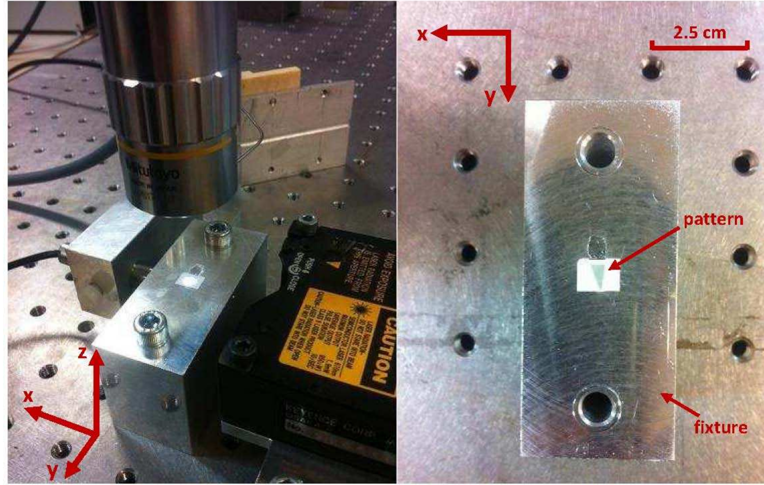

Figure 3.15: Photos of experimental setup for testing measurement uncertainty.

Table 3.3: Drift in x and y directions.

Axis	x	y
Drift rate ($\mu m/°C$)	0.157	1.357

To evaluate the measuring uncertainty, the vision system has to be tested by measuring static pattern. The motions of the pattern along x and y are measured with the camera. Fig.3.15 is the pictures of the vision system, a fixture glued with a pattern, and a temperature sensor. This vision system is always fixed on the same place during all the experiments in this chapter. Tests take place in the ambient temperature for 15 hours. The result of one of the tests is shown in Fig. 3.16. In this case, the temperature deviation is about 0.6 °C, and the measurement drifts about 0.1 μm in x direction, and drift in y direction is larger (0.9 μm). From Fig. 3.16(e), we can see the drift along y is quite proportional to the temperature deviation. However, the drift along x appears to be less correlated to the temperature change (Fig. 3.16(c)). The magnitude of the drift regarding temperature deviation is concluded in Table 3.3, even though the drift may not totally be induced by temperature. Drift rate in y direction is almost ten times of that in x direction. This is an intrinsic feature of our measuring system and is maximizing. Another two tests measuring the microrobotic system with XY stages on/off have been performed. The results demonstrate that the drift is also in the range as the fixture. To sum up, the results in the table can be regarded as measuring uncertainty inherent in our measuring system than which positioning accuracy cannot be improved better.

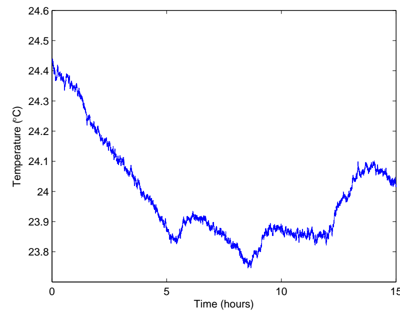

(a) Temperature

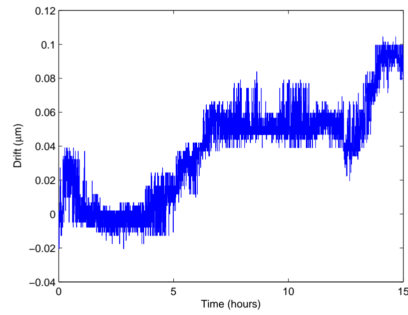

(b) Drift in x direction with time

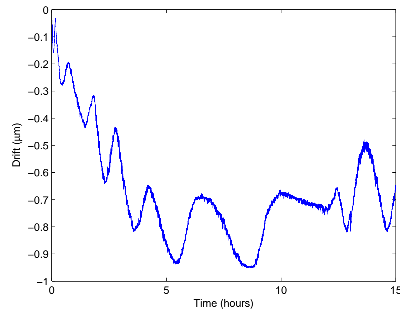

(c) Drift in y direction with time

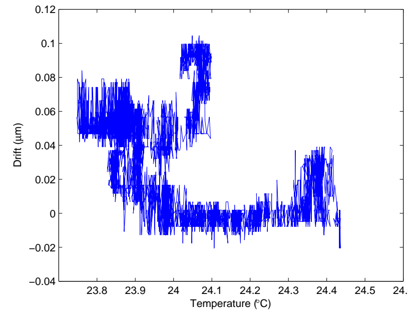

(d) Drift in x direction with temperature

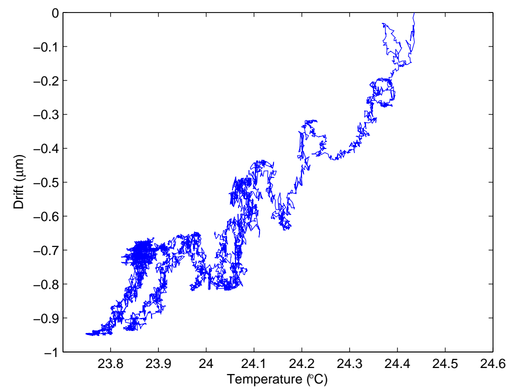

(e) Drift in y direction with temperature

Figure 3.16: Experimental results of measuring the fixed pattern.

3.5.2 Sensor for nanopositioning

For nanopositioning measurement, we use a commercial system with either one or two SP-S 120 SIOS laser interferometers (Meßtechnik GmbH). The interferometer has high resolution (0.3 nm) and large measuring range (± 2.2 mm) which are indicated in Table 3.5.2. These features are suitable for measurement of nanopositioning. Before using the interferometer, we should know first its measuring uncertainty. According to [15], the measuring uncertainty of interferometer can be classified into three categories: intrinsic errors, environmental errors, and installation errors. The uncertainties (denoted by $U_1, \ldots, U_8$) considered for errors budget are laser wavelength accuracy, electronics error, optics nonlinearity, wavelength compensation, optics thermal drift, deadpath error, Abbe error, and cosine error.

According to the standard GUM (Guide to the Expression of Uncertainty in Measurement) and [15], we obtain a set of uncertainties as shown in Table 3.5.2. The laser wavelength accuracy is obtained through laser wavelength stability which is negligible ($U_1 = 0.087$ nm). Electronics error which is equal to 0.08 nm is associated with the resolution 0.3 nm of the interferometer. Optics nonlinearity is different for each interferometer. Here, we do not have this value for our sensors. For estimation, we use the value 3 nm provided in [15]. Wavelength compensation and deadpath correction are realized by built-in temperature/pressure-correction module (incorporates a temperature sensor and barometric-pressure sensor. Three main atmospheric factors, temperature, pressure, and humidity, affect the laser wavelength. 1 ppm (parts per million, 1 ppm $= \frac{1}{10^6}$) error results from any one of the following change [15]:

- 1 $^\circ C$ change in ambient temperature;
- 2.5 mmHg change in ambient pressure;
- 80 % change in ambient relative humidity.

To compensate these atmospheric influence, there is a wavelength compensation system embedded in the interferometer. As stated in Table 3.5.2, the measuring uncertainties of temperature, pressure, and humidity are smaller than 0.1 K, 300 Pa, and 3% respectively. The atmospheric induced uncertainty is calculated as 0.262 nm. The uncertainty $U_5 = 29$ nm induced by optics thermal drift is calculated based on a typical ratio 0.5 μm/°C. The optics thermal drift comes from changes of the physical sizes and index-of-refraction of some optical components when temperature varies. Deadpath error U_6 is 26.2 nm. Abbe error is 10 nm which is due to parallel offset of the laser beam exiting the sensor head relative to the measurement axis. Cosine error is 0.76 nm which is due to angular misalignment of the beam exiting the sensor head on the object to be measured. Finally, the combined standard uncertainty including all these uncertainty sources is 40.6 nm. This uncertainty is the S in Eq. (3.10).

Table 3.4: Specification and evaluation of measuring uncertainty of interferometer SP-S 120 subjected to ambient temperature.

			Interferometer SP-S 120
	Laser wavelength		Approx. 633 nm
	Measuring range		±2.2 mm
	Resolution		0.3 nm
	Measured distance L		500 μm
	Deadpath length		5cm
Intrinsic errors	Laser wavelength stability		$\leq 3 \times 10^{-7} = 0.3$ ppm $U_1 = \frac{L(m)(0.3 \times 10^{-6})}{\sqrt{3}}$ $= \frac{0.0005 \times 0.3}{\sqrt{3}}$ $= 0.087$ nm
	Electronics error		$U_2 = \frac{0.0003/2}{\sqrt{3}} = 0.08$ nm
	Optics nonlinearity		$U_3 = \frac{0.0042}{\sqrt{2}} = 3$ nm
Environmental errors	Atmospheric compensation	Temp: $\leq$0.1K	U_W (ppm) = $\sqrt{(\frac{0.1}{\sqrt{3}})^2 + (\frac{0.9}{\sqrt{3}})^2 + (\frac{0.0375}{\sqrt{3}})^2}$ =0.5233 ppm $U_4 = U_W L = 0.5233$ ppm $\times$ 0.0005 = 0.262 nm
		Pressure: $\leq$0.6% of F. S. = 300 Pa =2.25 mmHg	
		Humidity: $\leq$3%	
	Optics thermal drift		$U_5 = \frac{0.1 \times (0.5 \mu m ^\circ C)}{\sqrt{3}} = 29$ nm
Installation errors	Deadpath error		$U_6 = 0.5233 \times 0.05 = 26.2$ nm
	Abbe error		$U_7 = \triangle$ L$_{Abbe}$=1cm$\times$tan(6μrad) =10 nm
	Cosine error		$U_8 = \triangle$ L$_{cos}$=L(1-cos(α)) =500$\mu m \times$(1-cos(0.1/°)) = 0.76 nm
Combined standard uncertainty	$\sqrt{(U_1)^2 + (U_2)^2 + (U_3)^2 + (U_5)^2 + (U_7)^2 + (U_8)^2 + (U_4 + U_6)^2}$ $= \sqrt{(0.087)^2 + (0.08)^2 + (3)^2 + (29)^2 + (10)^2 + (0.76)^2 + (0.262 + 26.2)^2}$ =40.6 nm		

3.6 Conclusions and objectives

In this chapter we review research works dedicated to calibration of macro and micro-nano robots. Objective accuracies to be achieved for micro- and nanopositioning are determined based on analysis about the state-of-the-art. Existing precision criteria are reviewed and discussed, and our further analysis and discussions about accuracy and repeatability are presented.

The relationship between accuracy/positioning errors and workspace/stroke of micropositioning in some state-of-the-art works is shown in Fig. 3.17. Performances achieved by closed loop are better than open loop which are as mentioned in last chapter. Closed loop control achieves accuracy better than 3 μm, and the best accuracy achieved

by open loop is about 4.7 μm. Also as discussed in Chapter 2, different literatures have their own calculation methods of accuracy, we can not compare them absolutely. However, we can still define the objectives of accuracy based on these results. For micropositioning, we aim to achieve accuracy ≤ 4 μm and propose a procedure for general purpose applicable for all microrobots.

The accuracies/errors achieved for nanopositioning in literature are shown in Fig. 3.18. Result in [54] is quite good and concerns performance in 50 minutes. Our objective is to achieve ≤ 100 nm for nanopositioning in a longer term (e.g., a few days) in room temperature.

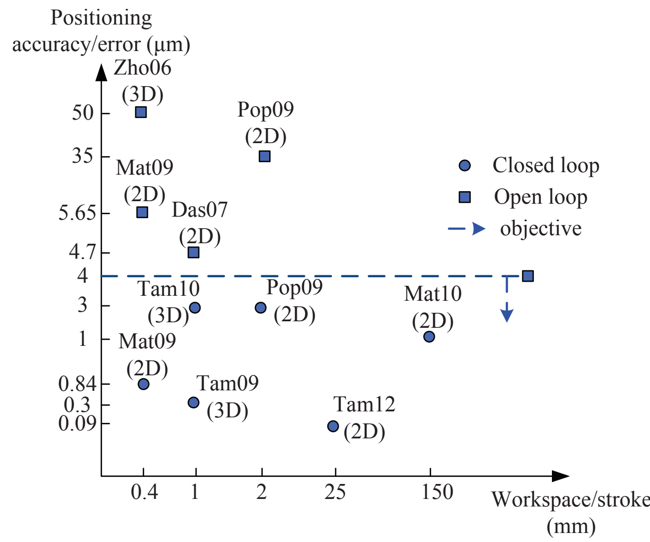

Figure 3.17: Micropositioning accuracy in state-of-the-art [21, 58, 57, 65, 80, 81, 82, 93].

There remain two main problems to be solved: 1. performances of micro-nano robots are relatively locally known and should be characterized; 2. improvement of micro-nano positioning accuracy. In terms of these issues, in the following two chapters, we aim at better understanding of robot behavior and sources of inaccuracy. Our objectives are to achieve accuracy ≤ 4 μm for micropositioning and ≤ 100 nm for nanopositioning. We will adopt the novel measuring tool for measuring micropositioning in a relatively large area (e.g., 10×4 mm). Thermal compensation in the long term will be investigated. All the characterization and calibration will be implemented on real micro-nano robotic stages and validated experimentally.

In this thesis, considering the most influential factors, we will tackle and quantify the influences of main imperfections which are assembly errors, position-dependent errors, and angle-dependent errors on the micropositioning stages. Temperature is a prevalent factor when it is not strictly controlled. For higher requirement of accuracy in nanopositioning, geometric errors and temperature effect are considered together for nanopositioning stages.

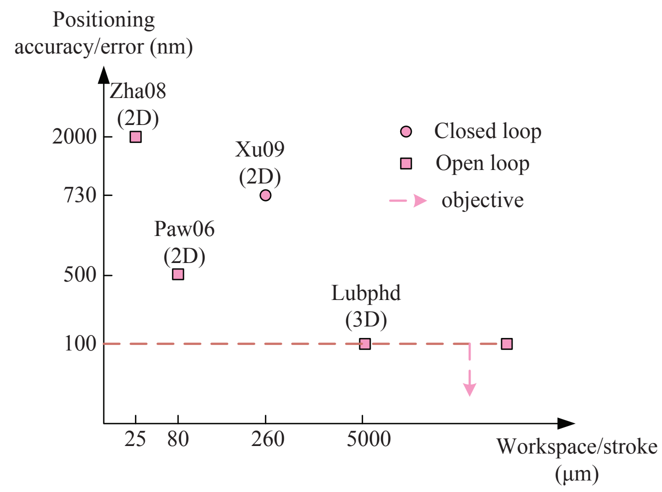

Figure 3.18: Nanopositioning accuracy in state-of-the-art [54, 64, 87, 90].

Chapter 4

Calibration of Microrobotic Systems

4.1 Introduction

This chapter deals with the calibration of microrobotic systems in order to achieve high positioning accuracy. Microrobotic systems comprising several micropositioning stages are commonly used in micromanipulation systems. Micropositioning stages have motion strokes from a few micrometers up to several tens of millimeters relying on mechanical guiding with friction based principle. Many factors influence the accuracy of microrobotic systems, such as the qualities of fabrication, linearity, backlashes, weight of the axes. Since the tasks at the microscale require high flexibility, microrobotic systems consisting of several micropositioning stages have to be constructed according to specific tasks [20]. Each of these stages usually has limited Degrees-of-Freedom. Then, several of them have to be assembled together to meet multi-DoF requirements. Tools such as gripper, probe, and sensors are fixed onto the stages as end-effector. The assemblies of micropositioning stages and end-effectors are usually performed by hands and not in an accurate way at this scale. Therefore, to achieve an positioning accuracy better than 4 μm, some physical parameters (e.g., perpendicularity of two stages and position of end-effector with respect to the stages) must be identified and compensated. Moreover, imperfections, such as position-dependent and angle-dependent errors, intrinsic to the micropositioning stages are noticeable issues at the microscale desiring higher accuracy.

In this chapter, we present a generic methodology to achieve microrobot calibration. This general framework consist of kinematic modeling, sources classification, and parameters identification. Subsequently, as a preliminary step for the full calibration, characterization and compensation for position-dependent errors of XY stages are performed using a lookup table. The XYΘ microrobotic system is chosen as the case study because such system includes most of the sources of inaccuracy at the microscale. Based on the generic framework and characterization information of XY stages, we perform a full procedure of calibration for the XYΘ microrobotic system. We consider five complementary models to analyze the most influential factors and quantify their relative influences and performances on the microrobotic system.

4.2 General methodology for calibration of microrobotic systems

4.2.1 Kinematic modeling

The objective of robotic calibration is to locate the end-effector to global positions accurately. To do that, different frames must be defined and their mathematical equations must be deduced based on the relative positions of the frames. As shown in Fig. 4.1, two coordinate frames are defined which are the world frame WF ($\{O_{WF}, \vec{x}_{WF}, \vec{y}_{WF}, \vec{z}_{WF}\}$) and the tool frame TF ($\{O_{TF}, \vec{x}_{TF}, \vec{y}_{TF}, \vec{z}_{TF}\}$). Every joint is assigned one frame. q_k is the kth joint variable which could be a translation distance or a rotation angle. The coordinates of point O_{TF} with respect to frame WF are represented by vector $(\overrightarrow{O_{WF}O_{TF}})_{WF}$ passing through all the joints and the tool. To depict the whole system and identify the parameters, a forward kinematics is required to define the relation between the joint coordinates q_k and the end-point coordinates with respect to WF. The forward kinematics of the robot is calculated by:

$$\begin{aligned}(\overrightarrow{O_{WF}O_{TF}})_{WF} &= (\overrightarrow{O_{WF}O_1})_{WF} + (\overrightarrow{O_1O_2})_{WF} \\ &+ \cdots + (\overrightarrow{O_kO_{k+1}})_{WF} + \cdots + (\overrightarrow{O_nO_{TF}})_{WF}. \end{aligned} \tag{4.1}$$

Furthermore, each vector can be expressed in its local coordinate frame:

$$\begin{aligned}(\overrightarrow{O_{WF}O_{TF}})_{WF} &= (\overrightarrow{O_{WF}O_1})_{WF} + T_1^{WF}(\overrightarrow{O_1O_2})_1 \\ &+ \cdots + T_k^{WF}(\overrightarrow{O_kO_{k+1}})_k + \cdots + T_n^{WF}(\overrightarrow{O_nO_{TF}})_n, \end{aligned} \tag{4.2}$$

where T_k^{WF} is the matrix expressing the transformation from the local frame of the kth joint to the world frame WF.

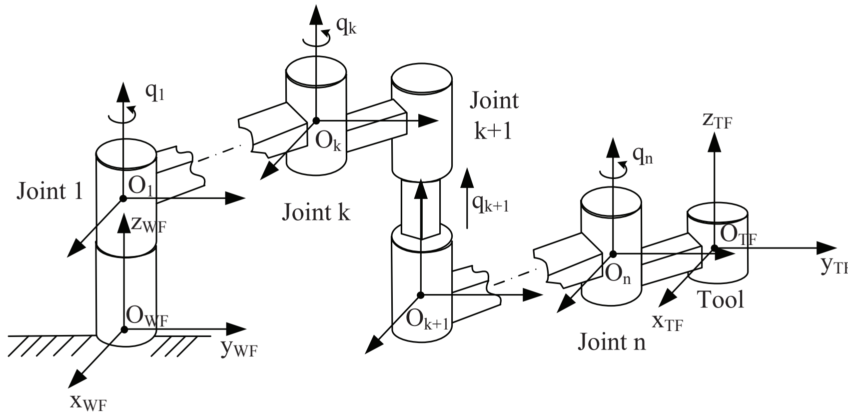

Figure 4.1: Kinematics of an n-DoF serial robot. World frame $\{O_{WF}, \vec{x}_{WF}, \vec{y}_{WF}, \vec{z}_{WF}\}$; joint variable q_k, $k = 1, \ldots, n$; joint frame $\{O_k, \vec{x}_k, \vec{y}_k, \vec{z}_k\}$, $k = 1, \ldots, n$; tool frame $\{O_{TF}, \vec{x}_{TF}, \vec{y}_{TF}, \vec{z}_{TF}\}$.

Parameters are identified based on the forward kinematics. Inverse kinematics is used to control the microrobotic system by implementing the models after calibration. For the sake of convenient discussion, the forward f and inverse g kinematics are represented by the following form:

$$\begin{cases} f(q,\phi) = P \\ g(P,\phi) = q, \end{cases} \tag{4.3}$$

where q is the vector of joint coordinates, ϕ is the vector of kinematic parameters, and P is the vector of tool coordinates with respect to the world frame.

4.2.2 Classification of error sources

For microrobotic systems commonly used, the most influential imperfections or unknown parameters can be classified into three types: the ones between two axes, the ones along a translation axis, and the ones about a rotation axis. In this work, we call them assembly errors, position-dependent errors, and angle-dependent errors, respectively.

The first type is shown in Fig. 4.2. We assume that a joint axis attached with a frame $\{O_k, \vec{x}_k, \vec{y}_k, \vec{z}_k\}$ links with an adjacent axis attached with a frame $\{O_{k+1}, \vec{x}_{k+1}, \vec{y}_{k+1}, \vec{z}_{k+1}\}$. Three parameters a_k, b_k, and c_k depict their relative positions along $\vec{x}_k$, $\vec{y}_k$, and $\vec{z}_k$ axes. Another two parameters α_k, β_k depict their relative orientations. These parameters are affected by the assembly process which are called assembly parameters.

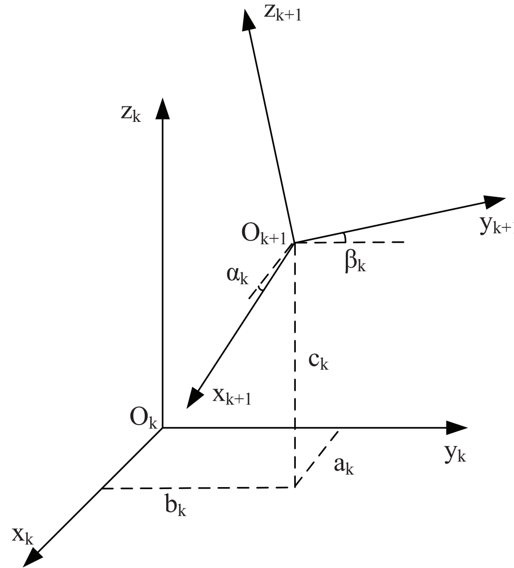

Figure 4.2: Assembly errors between two axes. $\{O_k, \vec{x}_k, \vec{y}_k, \vec{z}_k\}$=frame of mobile part of joint q_k; $\{O_{k+1}, \vec{x}_{k+1}, \vec{y}_{k+1}, \vec{z}_{k+1}\}$=frame of mobile part of joint q_{k+1}.

The second type is local imperfections along a translation axis (e.g., $\vec{x}_k$ axis in this case) shown in Fig. 4.3. Because the motions of micropositioning axes are not perfectly

linear, the commanded positions are not equal to the really reaching positions, and there are coupling errors in one axis when the motion happens in another axis. For a given joint input q_k, there are three translation and three rotation errors along the axis. The real position along the axis is $q_k + a_k(q_k)$ along $\vec{x}_k$ accompanying coupling errors $b_k(q_k)$ and $c_k(q_k)$ along $\vec{y}_k$, and $\vec{z}_k$ respectively when control input along $\vec{x}_k$ is q_k. Meanwhile, there are three angular defects $\alpha_k(q_k)$, $\beta_k(q_k)$, and $\gamma_k(q_k)$ along three directions.

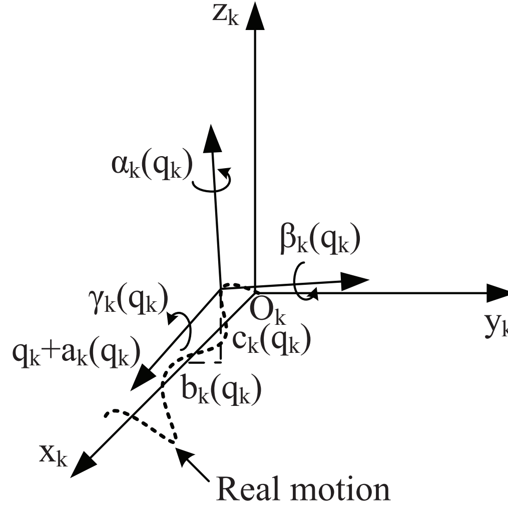

Figure 4.3: Position-dependent errors along a translation axis. $\{O_k, \vec{x}_k, \vec{y}_k, \vec{z}_k\}$=frame of mobile part of prismatic joint q_k.

The counterparts of the rotation around $\vec{z}_k$ axis are shown in Fig. 4.4. Depending on the rotating angle q_k, the rotation center changes in 3-dimensional space. The real trajectory is defined by three position errors $a_k(q_k)$, $b_k(q_k)$, and $c_k(q_k)$ when control input angle is q_k. Rotation motion may also generate angular errors in three directions which are $\alpha_k(q_k)$, $\beta_k(q_k)$, and $\gamma_k(q_k)$ along $\vec{x}_k$, $\vec{y}_k$, and $\vec{z}_k$, respectively.

These imperfections have different effects on positioning accuracy. Hence, in a following case study, we construct different models to investigate their influences on positioning accuracy taking into account these imperfections.

4.2.3 Parameters identification

Identification of the model parameters is performed following four steps: First, a cost function is built up inclusive of calculated poses and measured poses. Second, identifiability of the parameters is examined to evaluate whether the parameters are identifiable or not. Third, observability analysis is performed to estimate the optimal number of poses. The last step is to identify the parameters through minimizing the cost function. The first three steps are discussed in detail in followings, and the last step is performed with experimental data in next section. The second and third steps are investigated through simulation.

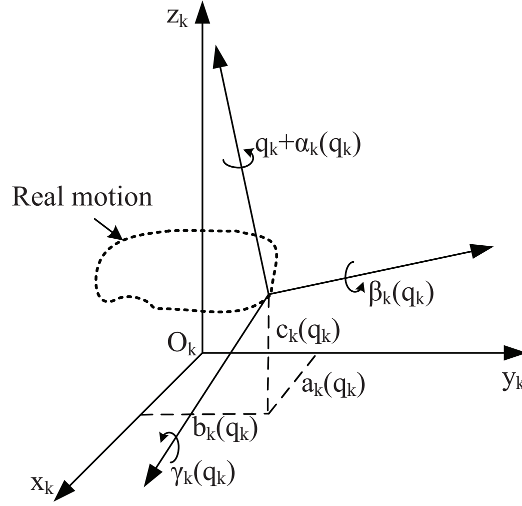

Figure 4.4: Angle-dependent errors about a rotation axis. $\{O_k, \vec{x}_k, \vec{y}_k, \vec{z}_k\}$=frame of mobile part of revolute joint q_k.

Cost functions

Parameters are identified through minimizing the error between measured position $P_m = (x_m, y_m, z_m)$ and calculated position $P_c = (x_c, y_c, z_c)$ which is calculated through forward kinematics. For the ith measured position $P_{mi} = (x_{mi}, y_{mi}, z_{mi})$ and the ith calculated position $P_{ci} = (x_{ci}, y_{ci}, z_{ci})$, the ith element of the cost function is defined as

$$e_i = \varepsilon_{x_i}^2 + \varepsilon_{y_i}^2 + \varepsilon_{z_i}^2$$

where

$$\begin{cases} \varepsilon_{x_i} = x_{ci} - x_{mi} \\ \varepsilon_{y_i} = y_{ci} - y_{mi} \\ \varepsilon_{z_i} = z_{ci} - z_{mi} \end{cases} \tag{4.4}$$

The cost function E can be defined with different pose combinations for n poses:

$$E = \sum_{i=1}^{n} e_i. \tag{4.5}$$

Parameters identification turns into an optimization problem of minimizing E.

Identifiability analysis

Identifiability analysis is going to determine if the parameters in the cost function are identifiable [43]. The determination of the identifiable parameters must be done before the identification process. The first equation of (4.3) is a general form of forward

kinematic equation that can be linearized as:

$$\Delta P = \frac{\partial f}{\partial \phi} \Delta \phi, \tag{4.6}$$

where $\frac{\partial f}{\partial \phi} = J$ is the Jacobian matrix.

Through QR decomposition [44], we have the following equation:

$$QR = J.$$

An upper triangular matrix R can be obtained where the elements on the diagonal correspond to the kinematic parameters. The non-identifiable parameters are those who are equal to zero.

Observability analysis

To identify unknown parameters, a set of poses is chosen and measurements are performed at these poses. In the expertise of robotic calibration, observability index measures the quality of the poses chosen. The observability index is based on singular values by Singular Values Decomposition (SVD) [77]. For a problem with m parameters, n poses, and 2-dimensional measurements, the Jacobian becomes:

$$J = U \Sigma V^T \tag{4.7}$$

using SVD, where U is $2n \times 2n$ orthogonal matrix, V is an $m \times m$ orthogonal matrix, and Σ is the $2n \times m$ matrix of singular values:

$$\Sigma = \begin{pmatrix} S \\ 0_{2n-m,m} \end{pmatrix}, \tag{4.8}$$

where

$$S = \begin{bmatrix} \sigma_1 & 0 & 0 & \cdots & 0 \\ 0 & \sigma_2 & 0 & \cdots & 0 \\ \vdots & \vdots & \vdots & \vdots & \vdots \\ 0 & 0 & 0 & \cdots & \sigma_m \end{bmatrix} \tag{4.9}$$

is a $m \times m$ matrix of ordered singular values, with $\sigma_1 \geq \sigma_2 \geq \cdots \geq \sigma_m \geq 0$; $0_{2n-m,m}$ is a $2n - m \times m$ matrix with all the elements are zero. There are four observability indices proposed in literature [77, 48, 33], which are denoted by O_1, O_2, O_3 and O_4 respectively.

Borm and *Menq* [7] proposed an observability index O_1 that maximizes the product of all of the singular values:

$$O_1 = \frac{\sqrt[m]{\sigma_1 \sigma_2 \cdots \sigma_m}}{m}. \tag{4.10}$$

Index O_2 [24] is the ratio of minimum singular value to the maximum singular value:

$$O_2 = \frac{\sigma_m}{\sigma_1}. \tag{4.11}$$

Index O_3 [61] is the minimum singular value:

$$O_3 = \sigma_m. \tag{4.12}$$

Index O_4 [61] is the product of O_2 and O_3 which is termed noise amplification index:

$$O_4 = \frac{\sigma_m^2}{\sigma_1}. \tag{4.13}$$

4.3 XYΘ microrobotic system and vision system

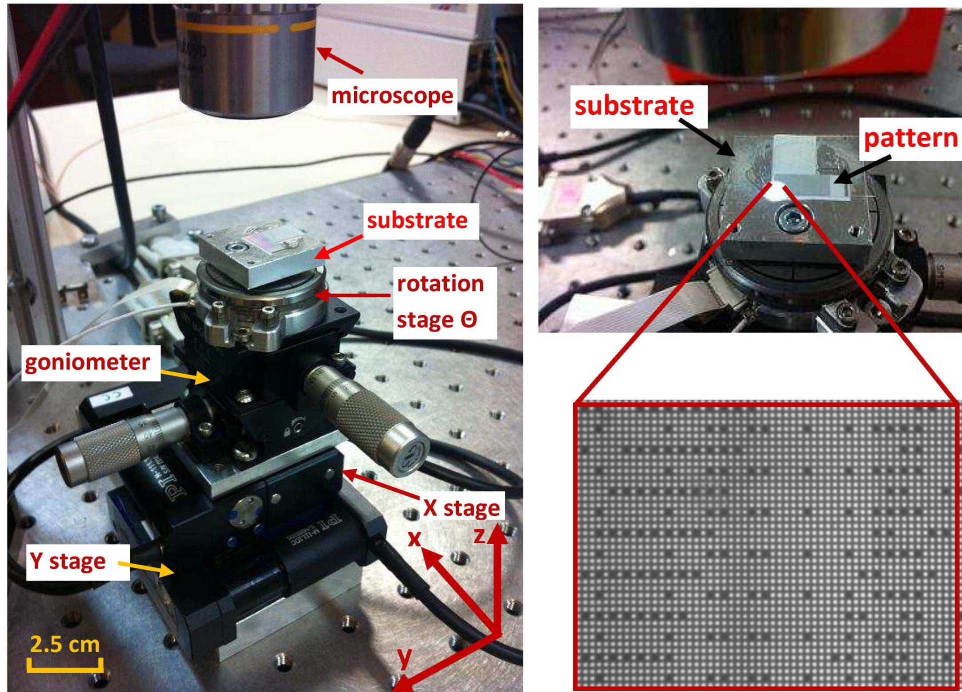

(a) The whole system: XYΘ microrobot and microscope measuring the tool frame (substrate).

(b) Pattern attached on the substrate and close view of the pattern

Figure 4.5: Experimental setup for the calibration of XYΘ microrobotic system.

Microrobotic systems have common features. For example, normally they consist of translation and rotation axes and suffer from imperfections mentioned above. Without loss of generality, a XYΘ microrobotic system [84] is chosen for case study. Based on commonly used devices for microscale applications, this XYΘ structure faces main kinds of imperfections influencing microrobots. The pictures of the whole experimental setup and the end-platform are shown in Fig. 4.5 (a) and (b). The microrobotic system is mounted on an anti-vibration table. It consists of two translation stages (XY) followed

by a rotation stage Θ in a 3-DoF serial robotic structure. The two translation stages are PI M-111.1DG equipped with MercuryTM C-863 controller. A miniature DC motor actuates motion via a backlash-compensated leadscrew system and gearhead. This kind of stages is representative for many micropositioning stages commonly used in micromanipulation which work with mobile parts that are guided based on friction principles. The rotary stage is SmarAct SR-3610-S which uses the stick-slip principle and is controlled by MCS-3D unit. All the micropositioning stages X, Y, and Θ are equipped with internal sensors and are closed-loop controlled in actuator layers already. The specifications of translation stages XY and rotation stage Θ from the datasheets are given in Table 4.1 and 4.2 respectively.

Table 4.1: Specification of XY translation stages in datasheet.

Stage	PI M-111.1DG
Travel range	15 mm
Resolution	50nm
Unidirectional repeatability	100nm
Pitch angle deviation	$\pm150\mu rad$
Yaw angle deviation	$\pm150\mu rad$
Backlash	$2\mu m$
Thread pitch	0.4 mm
Driving mechanism	Leadscrew

Table 4.2: Specification of Θ rotation stage in datasheet.

Stage	SmarAct SR-3610-S
Range	$360°$
Stepwidth	$0.3m°$ to $3m°$
Scanning range	$\simeq 4.3m°$
Resolution	$< 1.1\mu°$

The external measuring system for calibration consists of a video camera (AVT STINGRAY F-125C), a microscope lens (Optem zoom 70XL), an objective with $10\times$ magnification and a micro-pattern which has been already introduced in Chapter 3 (Fig. 5.5 (b)). The representation of this binary code use the pseudo-periodic distribution of dots. The binary code enables absolute position (x and y) and orientation (Θ) retrieval from any view of a local zone observed by the vision with respect to the whole encrypted pattern. The measuring range in the present case is 9.5 mm for x-axis and is 4.2 mm for y-axis. The resolution is below 10 nm. About the fabrication, working principle, characterization of the pattern and the algorithm, one can refer to [89, 75] for

more details. Besides, the image format is 1024×768 mono in this work. The upper goniometer (M-GON40-U) and lower goniometer (M-GON40-L) are used for adjusting the parallelism between the pattern and the camera.

4.4 Characterization and compensation of position-dependent errors along XY stages

Before performing calibration of the whole XYΘ microrobotic system, we propose to study and characterize the errors along XY stages first. This step is for understanding of robot and error behaviors and for the use for further calibration.

4.4.1 Characterization of position-dependent errors

As discussed in Chapter 2, the nonlinearity errors along axes may be significant characteristics of precise positioning stages. These errors are position-dependent and due to the geometric nature of the axes. In macroscale robotics, this type of errors is usually neglected in calibration which mainly focuses on kinematic parameters identification or elastic deformation. It is because even though they exit in robot's axes, their influence is negligible with respect to other errors. However, these errors become significant at the microscale, especially for Cartesian microrobots. According to the specification of the PI stage, the driving mechanism is leadscrew. So the errors along the axis could be foreseen somehow based on the mechanical property. The error curves are functions of axis coordinates, and the functions are different from one axis to another, so measurements of these errors for every axis are necessary. The position-dependent errors are calculated by comparing the measured positions (estimation of real positions) with the target positions (positions to be reached). The designed trajectories of measurement are 1-DoF straight lines, that is, one stage is moving, while another stage is kept static.

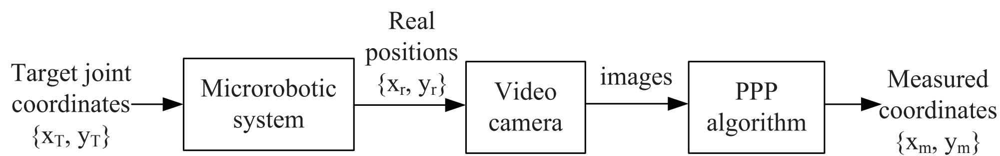

Figure 4.6: Block diagram of characterization of nonlinearity errors.

As depicted in Fig. 4.6, each of micropositioning stages X or Y is controlled to reach appointed target coordinate x_T or y_T. One axis moves while another axis keeps still. At the real positions x_r, y_r, the camera captures the images of the pattern which are processed subsequently with the decoding algorithm so as to obtain measured coordinates x_m and y_m. Every cycle of trajectory corresponds to one forward and one backward motion along X or Y. In the 9500 and 4200 μm strokes of XY stages, measurements are taken with 5 μm as step size and a total of 11403 and 5043 data are obtained in 3 cycles. Time spent on data acquisition is 9.5 hours and on data processing is 23 hours.

Fig. 4.7 shows the repeatability of errors along x for all measuring points of X axis. The repeatability calculated in 3 cycles is $\leq 1\ \mu m$ for most of the measuring points except for two peaks. This result is larger than what we expect from Table 4.1. This is because the duration of the test and experimental condition are different from our experiment to those of datasheet. The performance tests of PI company are performed in a short term and metrology lab with temperature control. However, the residual errors after compensation should theoretically not be better than our measured repeatability.

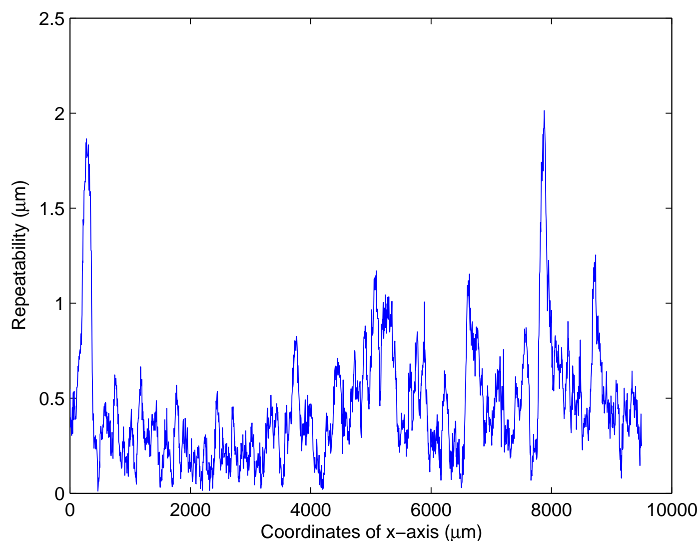

Figure 4.7: Repeatability of errors in x direction when X stage is moving forwards.

The errors between x_T and x_m measured in one cycle is shown in Fig. 4.8. It can be seen that errors vary cyclically. Such behavior is reasonably assumed due to systematic turn-to-turn nature inherent in the leadscrew. The thread pitch of the stage is 400 μm, so the cyclical error repeats with the same period. We can also see that the periods of the errors in forward and backward motions of the X stage are the same, but the magnitudes are quite different, which may be due to the fact that the driving system does not work symmetrically.

Position-dependent errors appear not only in the driving direction but also in the lateral direction. Fig. 4.9 shows this coupling errors in y direction when only X stage is moving forwards and backwards. It can be seen that the coupling errors have the same period as the errors in driving direction.

4.4.2 Compensation of position-dependent errors

As mentioned before, we have characterized the position-dependent errors of discrete coordinates along each axis. The error at a given point contains two parts, the first part induced by X motion and the second part by Y motion. We define $f_{xi}(x_T, 0)$ and

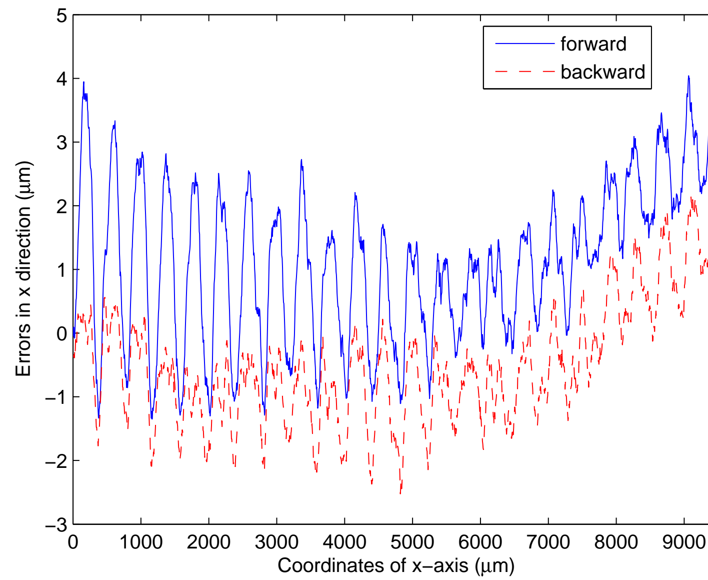

Figure 4.8: Errors $(x_T - x_m)$ in x direction when X stage is moving forwards and backwards in one cycle.

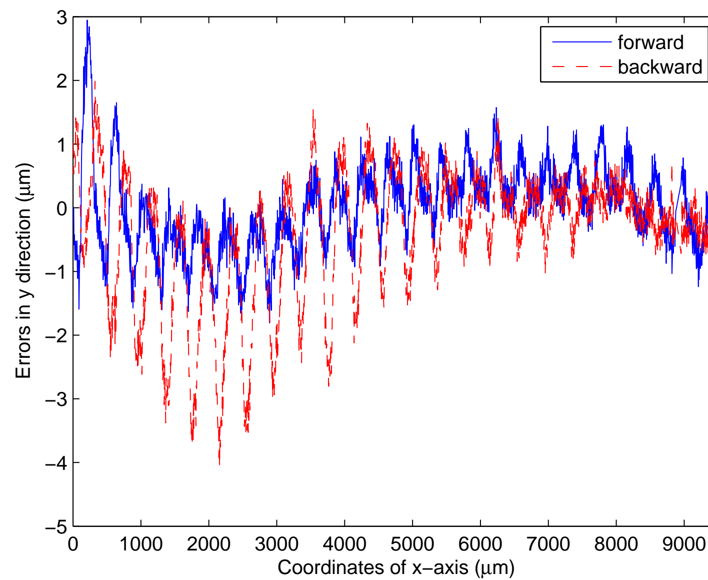

Figure 4.9: Coupling errors $(0 - y_m)$ in y direction when X stage is moving forwards and backwards in one cycle.

$f_{yi}(0, y_T)$ that denotes the errors component in i direction when moving forward along x or y axis to target x_T or y_T, and $b_{xi}(x_T, 0)$ and $b_{yi}(0, y_T)$ that denotes the errors component in i direction when moving backward along x or y axis to target x_T or y_T.

The schematic diagram (Fig. 4.10) shows the compensation principe based on a lookup table. Depending on the motion direction (forward or backward) and the target coordinates, the error components have various combinations. Take X stage as an example, first the kth target position x_{Tk} and its previous target x_{Tk-1} are compared to judge it is doing forward or backward motion; second, the program selects the corresponding errors from the lookup table of X stage based on the information of motion direction; finally these error components are summed up to form the total errors. The aggregated errors $ex(x_T, y_T)$ and $ey(x_T, y_T)$ along x and along y are expressed by the following equations:

$$ex = \begin{bmatrix} f_{xx}(x_T, 0) \\ or \\ b_{xx}(x_T, 0) \end{bmatrix} + \delta_x(y_T) + \begin{bmatrix} f_{yx}(0, y_T) \\ or \\ b_{yx}(0, y_T) \end{bmatrix} \tag{4.14}$$

$$ey = \begin{bmatrix} f_{xy}(x_T, 0) \\ or \\ b_{xy}(x_T, 0) \end{bmatrix} + \begin{bmatrix} f_{yy}(0, y_T) \\ or \\ b_{yy}(0, y_T) \end{bmatrix} \tag{4.15}$$

Due to the fact that the Y stage is not perfectly perpendicular to the X stage, the errors in x direction should be added by a bias $\delta_x(y_T)$ depending on the y coordinate.

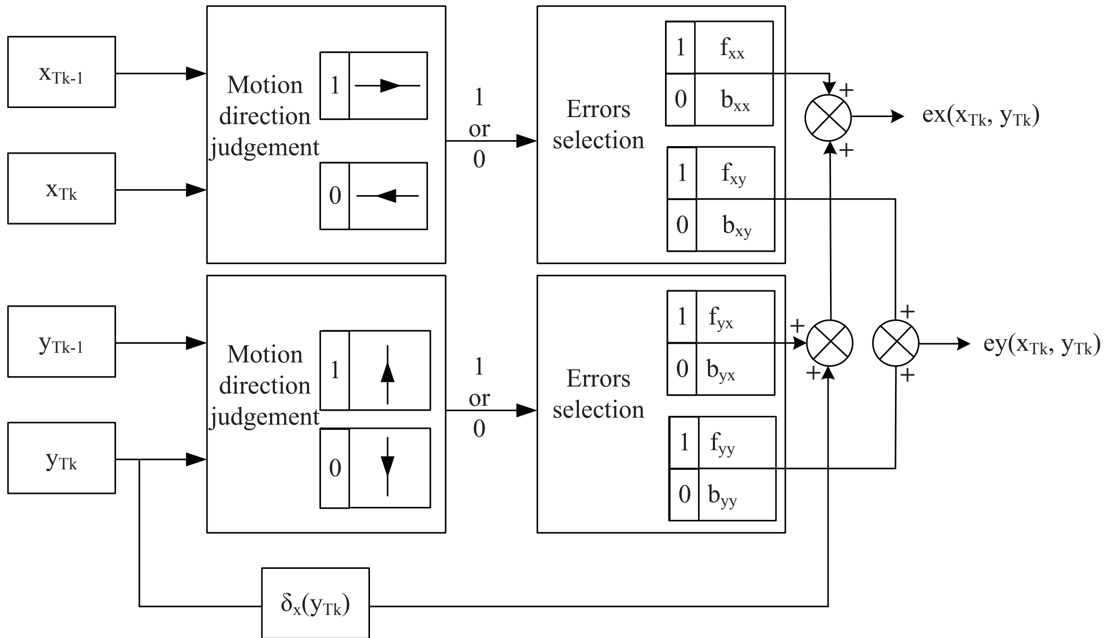

Figure 4.10: Schematic diagram of the errors combination mechanism for compensation.

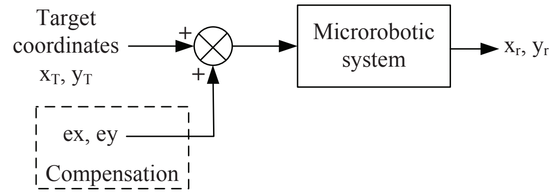

Figure 4.11: Block diagram of compensation for nonlinearity errors using lookup table.

Trajectories tracking

The first test is tracking of a square trajectory with nonlinearity compensation using a lookup table. The planning trajectory is chosen with a size of $4000 \times 4000\mu m$ square spanning from coordinates $10\mu m$ to $4010\mu m$. In this test, the input of the XY stages is the target trajectory minus the corresponding geometric errors in the lookup table instead of the target trajectory alone as shown in Fig. 4.11. For compensation, the errors at the target points are eliminated by adding the same amplitude of errors to the input. The square is divided into 4 segments: AB, BC, CD, and DA (Fig. 4.12). The tracking performances with and without ($ex = exy = 0$) compensation are shown in Fig. 4.13. We can see the tracking accuracy (calculated following ISO standard 9283 introduced in Chapter 3) of four segments of the square. Accuracy is about 22 μm without compensation which is contributed by the perpendicularity error (about 20 μm in BC and DA segments) mainly and by position-dependent error (AB and CD segments). In CD segment, the inaccuracy induced by position-dependent error is reduced from about 4 μm to 2 μm. After compensation, accuracy approximately improves to 3 μm (86% inaccuracy reduction).

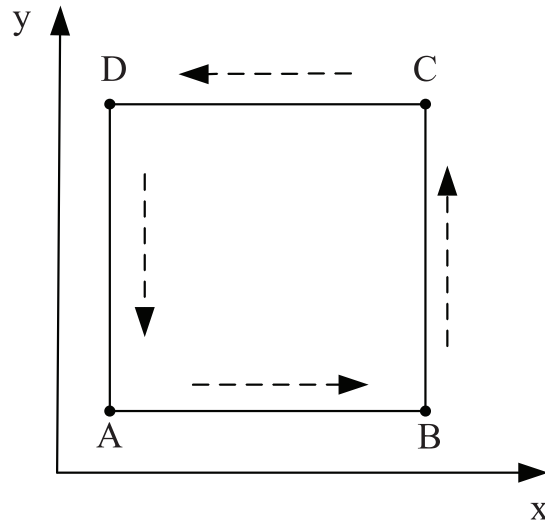

Figure 4.12: Square trajectory (4 segments).

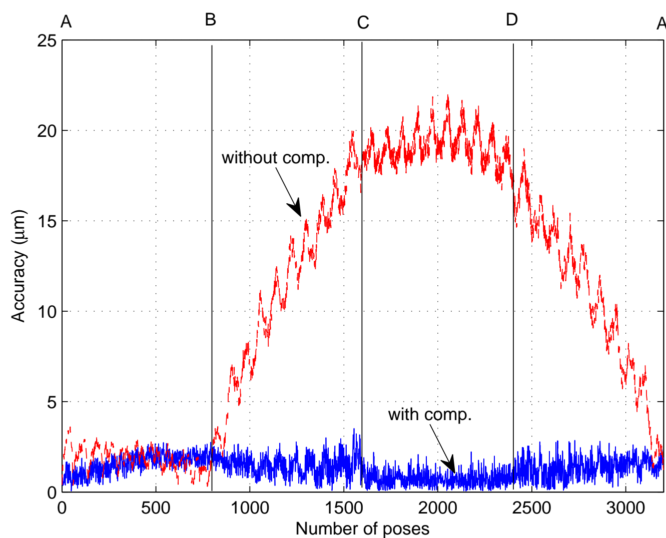

(a) Accuracy in all poses of tracking a square.

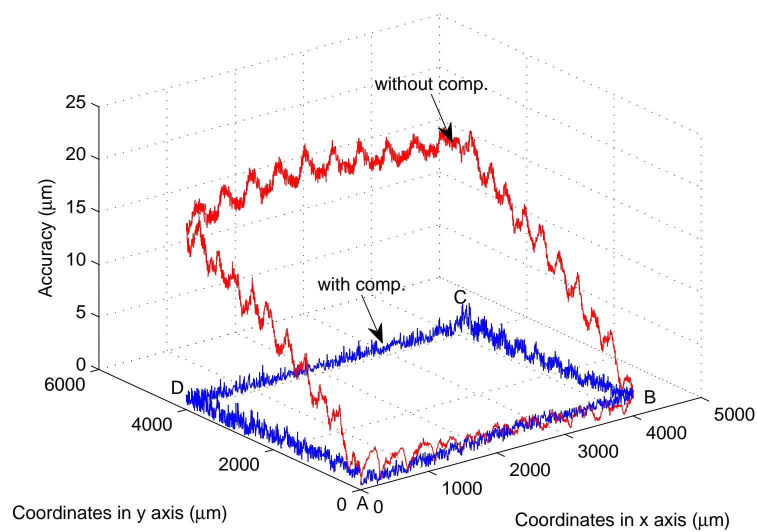

(b) 3D display of accuracy.

Figure 4.13: Accuracy of tracking 4 × 4 mm square trajectory with and without compensation.

Random points positioning

To examine the positioning accuracy of arbitrary points in the whole joint workspace experimentally, XY stages are commanded to reach random coordinates. The input targets P_{Ti} are coordinates of ten points which are randomly chosen. Hence, targets might not be in the lookup table, the errors at these targets either. In this case, interpolation techniques are required to calculate the unknown errors (interpolated errors) based on the knowledge of known errors (characterized errors). The block diagram of this process is shown in Fig. 4.14. Here, x'_T and y'_T could be the coordinates x_T and y_T in the lookup table or the ones not (need interpolation). Table 4.3 shows the coordinates of ten random targets defined for the test. The XY stages are controlled to reach the target $P_1, \ldots, P_{10}$ in sequence. Two interpolation techniques (Matlab® function *interp*1) are used for comparison. The sequence of the tests is no compensation, linear interpolation, and cubic spline interpolation. From Fig. 4.15, we can see that the positioning accuracy is improved from about 22 μm to 7 μm (68% reduction) by using the interpolated compensation. The two interpolation techniques provide more or less equivalent results in this case.

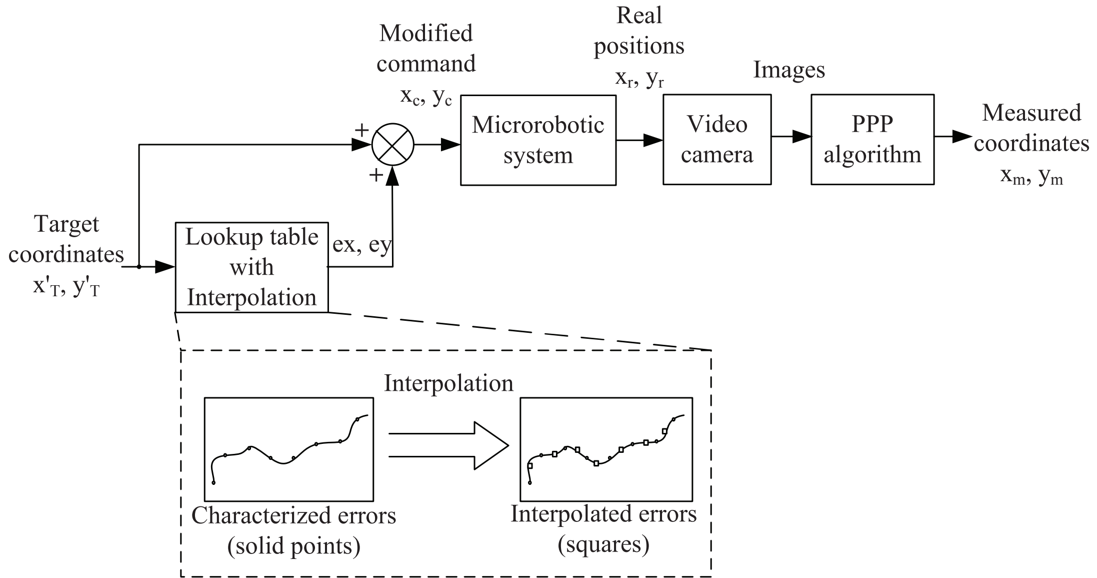

Figure 4.14: Block diagram of interpolation and compensation.

4.5 Calibration of the serial XYΘ microrobotic system

For the case study of the serial XYΘ microrobotic system, Fig. 4.16 is the kinematic diagram demonstrating the frames attachment. The microrobotic system consists of three actuated joints (stages) X, Y, and Θ. The pattern is fixed on a substrate located on the rotation stage Θ. The tool frame TF is the Pattern Frame PF ($\{P, x_{PF}, y_{PF}, z_{PF}\}$)

Table 4.3: Coordinates of random targets.

Targets	P_1	P_2	P_3	P_4	P_5	P_6	P_7	P_8	P_9	P_{10}
$x_T(\mu m)$	3471	6044	3673	5118	3643	8196	1702	3776	3903	1035
$y_T(\mu m)$	2311	3991	39	2738	2071	186	756	3815	1390	35

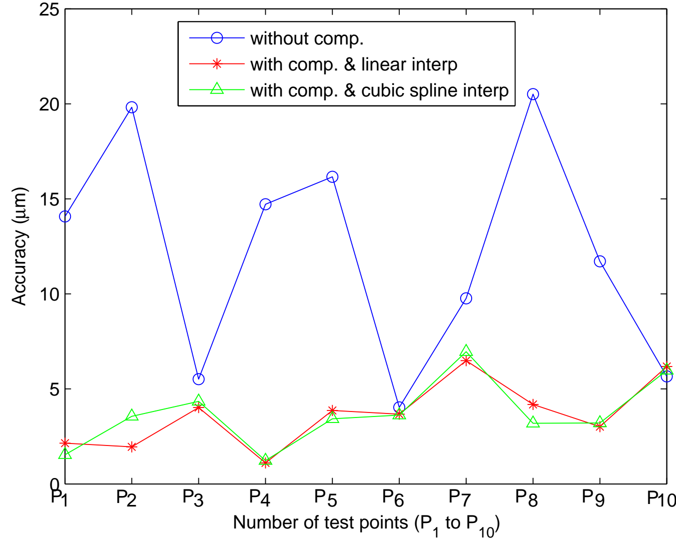

Figure 4.15: Positioning accuracy of random points with and without compensation of position-dependent and geometric errors for XY stages.

attached to the pattern moving with different poses of the microrobotic system. The origin P of the pattern is defined as the tool tip of the end-effector, so this is the point of interest to be controlled. We define the World Frame WF ($\{O_{WF}, x_{WF}, y_{WF}, z_{WF}\}$) locating on the table. x_{WF} and y_{WF} are parallel with x_{PF0} and y_{PF0} of the initial pattern frame ($\{P_0, x_{PF0}, y_{PF0}, z_{PF0}\}$), respectively. Frames $F1$ ($\{O_1, x_1, y_1, z_1\}$) and $F2$ ($\{O_2, x_2, y_2, z_2\}$) are assigned to the mobile parts of Y and X stages respectively. The Y motion is along y_1, and the X motion is along x_2. Under the hypothesis of perfect perpendicularity between the rotation axis and the XY plane, the frame $F3$ ($\{O_3, x_3, y_3, z_3\}$) is attached to the mobile part of Θ stage with the same x and y directions as the world frame. The Θ motion rotates with z_3 in clockwise. M is the origin of the image frame $\{M, x_{MF}, y_{MF}\}$).

In this case, we focus on 2-D planar motion with the coordinate frames and parameters. The main imperfections in this system are rotation center coordinates (x_R,y_R) with respect to WF, alignment angle α and assembly error β, position-dependent errors ex along X stage and ey along Y stage, and angle-dependent error f_{ax} along x_{WF} and f_{ay} y_{WF}. α is the angle between x_{WF} and x_2, and β is the angle between y_1 and y_2. The

rotation center O_3 is (x_R, y_R) with respect to world frame. The positive direction of X motion is not parallel to the x axis of world frame. Then, the parameter α is the angle between x_W and x_2 which is the 180° in the ideal case, and β is the perpendicularity error between X stage and Y stage which is also the angle between y_1 and y_2.

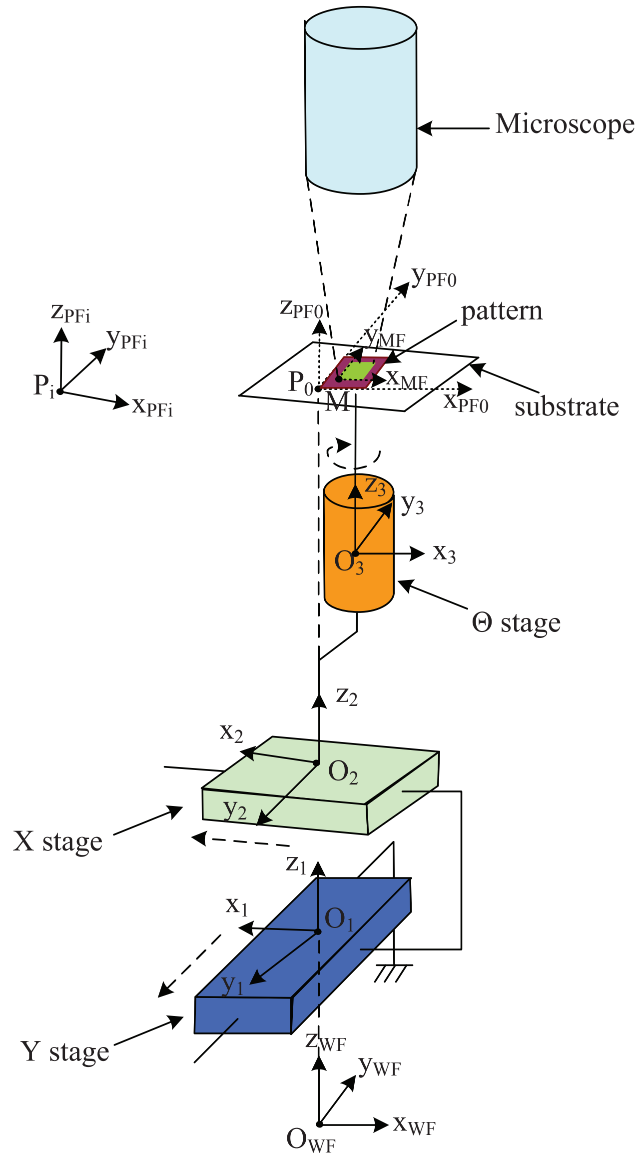

Figure 4.16: Kinematic diagram of the XYΘ microrobotic system. y_1, x_2, z_3 are the motion joints Y, X, and Θ, respectively.

The coordinates of point P in frame WF is represented by vector $(\overrightarrow{O_{WF}P})_{WF}$ passing through all the joint axes of the microrobotic system and the end-point (x_P, y_P):

$$(\overrightarrow{O_{WF}P})_{WF} = (\overrightarrow{O_{WF}O_1})_{WF} + (\overrightarrow{O_1O_2})_{WF} + (\overrightarrow{O_2O_3})_{WF} + (\overrightarrow{O_3P})_{WF}. \tag{4.16}$$

Furthermore, each vector can be expressed in its local coordinate frame:

$$(\overrightarrow{O_{WF}P})_{WF} = (\overrightarrow{O_{WF}O_1})_{WF} + T_1^{WF}(\overrightarrow{O_1O_2})_1 + T_2^{WF}(\overrightarrow{O_2O_3})_2 + T_3^{WF}(\overrightarrow{O_3P})_3. \tag{4.17}$$

Given joint coordinates $q_1 = X$, $q_2 = Y$, and $q_3 = \Theta$, parameters $\phi = \{x_R, y_R, \alpha, \beta\}$, and considering ex, ey, f_{ax} and f_{ay}, the coordinates of end point in the world frame could be calculated by expanding Eq. (4.17):

$$\begin{bmatrix} x_P \\ y_P \end{bmatrix} = \begin{bmatrix} (X - ex)\cos(\alpha) - (Y - ey)\sin(\alpha + \beta) \\ +x_R + f_{ax}(\Theta) - x_R\cos(\Theta) - y_R\sin(\Theta); \\ (X - ex)\sin(\alpha) + (Y - ey)\cos(\alpha + \beta) \\ +y_R + f_{ay}(\Theta) + x_R\sin(\Theta) - y_R\cos(\Theta) \end{bmatrix}, \tag{4.18}$$

which is the forward kinematics of the microrobotic system. ex and ey are corresponding position-dependent errors of coordinate (X,Y). $f_{ax}(\Theta)$ and $f_{ay}(\Theta)$ are angle-dependent errors when rotation angle equals to Θ. Then the inverse kinematics can be obtained accordingly:

$$\begin{bmatrix} X \\ Y \end{bmatrix} = \begin{bmatrix} \frac{1}{\cos(\beta)}\Big(x_P\cos(\alpha + \beta) + y_P\sin(\alpha + \beta) \\ -x_R\cos(\alpha + \beta) - y_R\sin(\alpha + \beta) \\ +x_R\cos(\Theta + \alpha + \beta) \\ +y_R\sin(\Theta + \alpha + \beta)\Big) + g_{ax} + ex; \\ \frac{1}{\cos(\beta)}\Big(- x_P\sin(\alpha) + y_P\cos(\alpha) \\ +x_R\sin(\alpha) - y_R\cos(\alpha) \\ -x_R\sin(\Theta + \alpha) + y_R\cos(\Theta + \alpha)\Big) + g_{ay} + ey \end{bmatrix}, \tag{4.19}$$

where $g_{ax}(\Theta)$ and $g_{ay}(\Theta)$ are inverse increment of $f_{ax}(\Theta)$ and $f_{ay}(\Theta)$ providing to joint input. We choose a lookup table to construct $g_{ax}(\Theta)$ and $g_{ay}(\Theta)$ with corresponding Θ. And, of course, interpolation might be needed if angle Θ is not a part of the lookup table.

4.5.1 Five calibration models

We propose five models (Model I to V) to investigate the influence of every kind of imperfection. All specific parameters in the case study and their corresponding general

Table 4.4: Variables and parameters in five models (Model I to V).

Model	a_1	b_1	α_1	a_2	b_2	α_2	a_3	b_3	α_3
I	0	Y	180	X	0	0	x_R	y_R	Θ
II	0	Y	$\alpha+\beta$	X	0	α	x_R	y_R	Θ
III	ex	$Y+ey$	$\alpha+\beta$	$X+ex$	ey	α	x_R	y_R	Θ
IV	0	Y	$\alpha+\beta$	X	0	α	$x_R+f_{ax}(\Theta)$	$y_R+f_{ay}(\Theta)$	Θ
V	ex	$Y+ey$	$\alpha+\beta$	$X+ex$	ey	α	$x_R+f_{ax}(\Theta)$	$y_R+f_{ay}(\Theta)$	Θ

parameters are listed in Table 4.4. As defined Section 4.2, a_i, b_i, and α_i are positions and angle of the frame of the ith axis with respect to the $i-1$th one.

First, for a microrobotic system with rotation axis, the location of the rotation center is the desired knowledge for modeling and control. So the first model considers the basic parameters which are identified x_R and y_R. The nominal values $\alpha = 180°$, $\beta = 0°$, and $ex = ey = f_{ax} = f_{ay} = g_{ax} = g_{ay} = 0$ are used for alignment and assembly parameters. Based on Eq. (4.3), (4.18), and (4.19), Model I is expressed as:

$$\begin{cases} f([X,Y,\Theta],[x_R,y_R,180,0]) = [x_P,y_P] \\ g([x_P,y_P],[x_R,y_R,180,0]) = [X,Y,\Theta]. \end{cases} \tag{4.20}$$

This model considers the minimum requirement of modeling ignoring other errors which could also be called the basic geometric model.

Model II takes into account two more parameters than Model I (α and β):

$$\begin{cases} f([X,Y,\Theta],[x_R,y_R,\alpha,\beta]) = [x_P,y_P] \\ g([x_P,y_P],[x_R,y_R,\alpha,\beta]) = [X,Y,\Theta]. \end{cases} \tag{4.21}$$

In addition to the basic parameters x_R and y_R, this model also tackles the inaccuracy induced by alignment parameter α and assembly error β.

Taking into account position-dependent errors in parameters identification phase and inverse kinematics, we have Model III:

$$\begin{cases} f([X-ex,Y-ey,\Theta],[x_R,y_R,\alpha,\beta]) = [x_P,y_P] \\ g([x_P,y_P],[x_R,y_R,\alpha,\beta]) + [ex,ey] = [X,Y,\Theta]. \end{cases} \tag{4.22}$$

To quantified ex and ey, a preliminary experiment is performed, and values of ex and ey are obtained at a set of discrete points along XY axes (see Section 4.4). A lookup table can be built up with this information. Interpolation technique is used to calculate the corresponding ex and ey at the points not measured.

Angle-dependent errors induced by Θ motion are compensated in Model IV which is depicted as:

$$\begin{cases} f([X,Y,\Theta],[x_R,y_R,\alpha,\beta]) + [f_{ax}(\Theta),f_{ay}(\Theta)] = [x_P,y_P] \\ g([x_P,y_P],[x_R,y_R,\alpha,\beta]) + [g_{ax}(\Theta),g_{ay}(\Theta)] = [X,Y,\Theta]. \end{cases} \tag{4.23}$$

Finally, the most advanced model (Model V) takes into account all four kinds of imperfections which is formalized as:

$$\begin{cases} f([X-ex, Y-ey, \Theta], [x_R, y_R, \alpha, \beta]) \\ +[f_{ax}(\Theta), f_{ay}(\Theta)] = [x_P, y_P] \\ g([x_P, y_P], [x_R, y_R, \alpha, \beta]) + [g_{ax}(\Theta), g_{ay}(\Theta)] \\ +[ex, ey] = [X, Y, \Theta]. \end{cases} \quad (4.24)$$

In summary, different models tackle different sets of aforementioned imperfections. Their corresponding relation is summarized in Table 4.5. Model I is basic geometric model considering basic parameters x_R and y_R. Model II considers the basic parameters as well as another geometric parameter α and β. As an enhanced version of Model II, Model III compensates errors along X and Y considering microscale specificities, namely, position-dependent errors ex and ey. Instead of position-dependent errors, Model IV directly compensates angle-dependent errors even though a part of position-dependent errors could also be compensated in this process. Most important imperfections are taken into account in Model V. Considering more and more imperfections, the model complexity is getting higher and higher from Model I to Model V which means the models should be selected based on their performances and complexities.

Table 4.5: Imperfections and parameters considered by five models.

Calibration Model	Rotation center x_R and y_R	Assembly parameters α and β	Position-dependent errors ex and ey	Angle-dependent errors f_{ax} and f_{ay}	Model complexity
Model I: Basic geometric	⋆				⋆
Model II: Geometric	⋆	⋆			⋆⋆
Model III: Geometric + position-dependent	⋆	⋆	⋆		⋆⋆⋆
Model IV: Geometric + angle-dependent	⋆	⋆		⋆	⋆⋆⋆⋆
Model V: Geometric + position-dependent + angle-dependent	⋆	⋆	⋆	⋆	⋆⋆⋆⋆⋆

4.5.2 Calibration procedures

From a general point of view, Model I and Model II follow the conventional calibration procedure (1. Modeling, 2. Data acquisition, 3. Identification, 4. Implementation, 5. Validation) [73, 26] as shown in Fig. 4.17. The calibration procedure for Model III tackling the position-dependent errors is displayed in Fig. 4.18. These microscale errors are measured and interpolated in pre-calibration sub-procedure and added into the joint input in identification and implementation phases. The calibration procedure of Model IV is Fig. 4.19 where post-calibration is proposed to compensate the angle-dependent errors. The procedure of Model V combines the conventional procedure with two sub-procedures for all the imperfections compensation.

Although the numbers of imperfections are the same in Model III and IV, the post-calibration sub-procedure of Model IV should be performed after the main procedure,

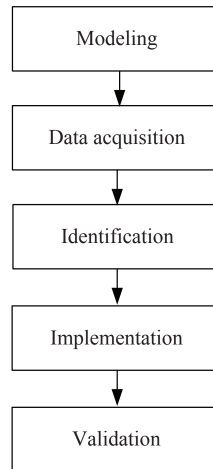

Figure 4.17: Flowchart of the calibration procedure for Model I and Model II.

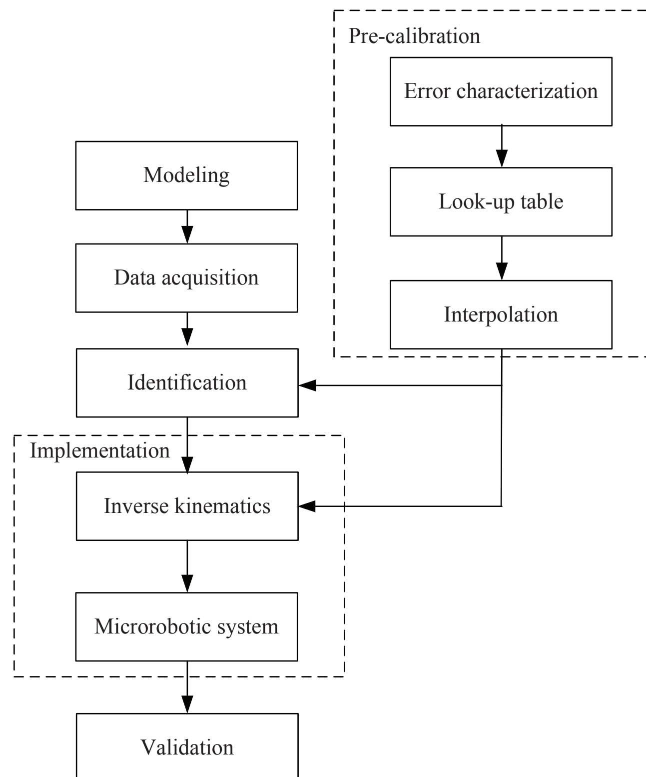

Figure 4.18: Flowchart of the novel calibration procedure for Model III.

and the pre-calibration sub-procedure could be reused time to time. So Model IV ranks higher complexity than Model III.

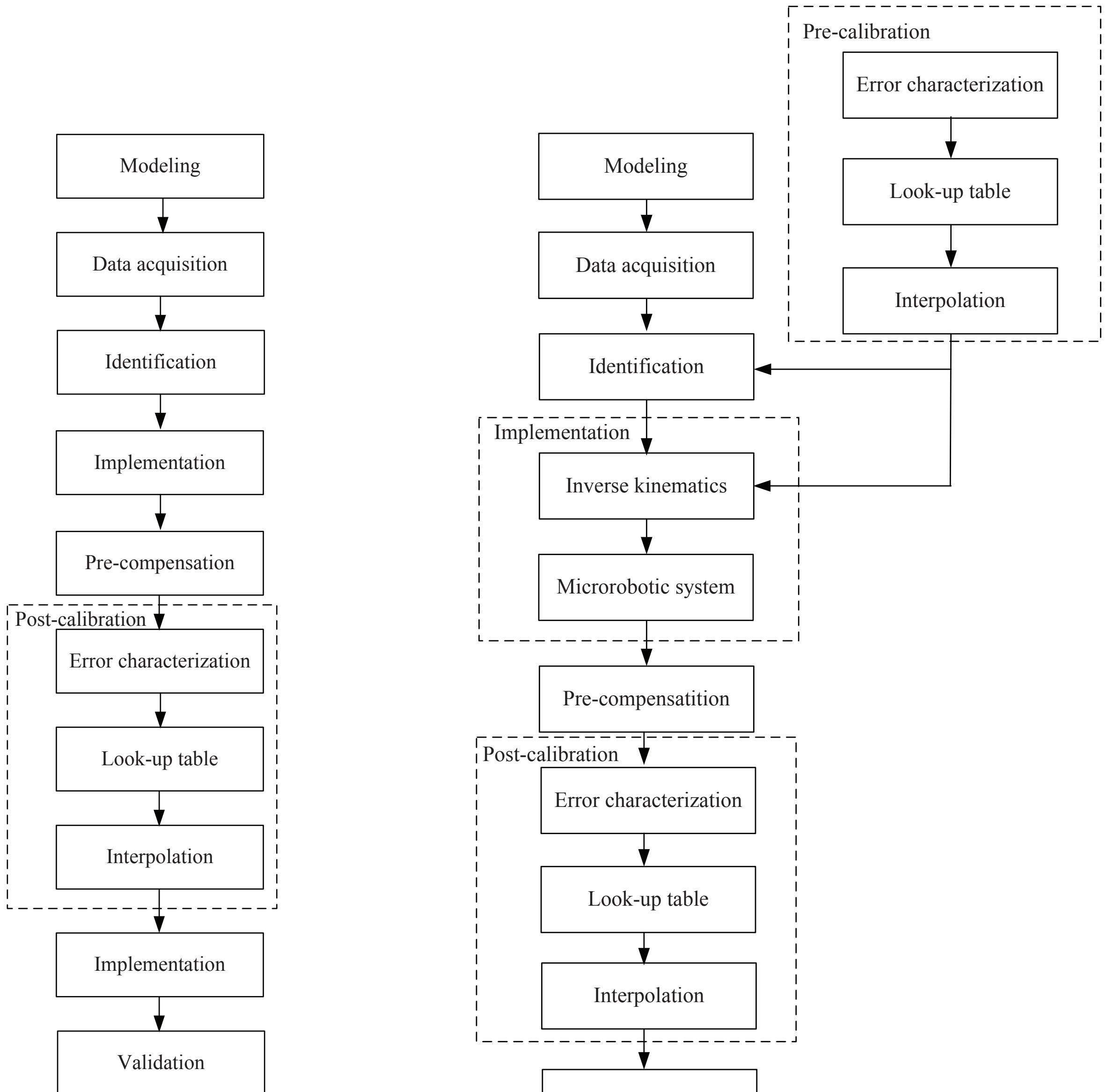

Figure 4.19: Flowchart of the novel calibration procedure for Model IV.

Figure 4.20: Flowchart of the novel calibration procedure for Model V.

4.5.3 Measuring information

The measuring information in traditional calibration is normally the position of the end-effector with respect to the measuring device fixed during calibration. To obtain such information, additional processing is required because the measuring principle in our case is different from those of conventional vision systems. The ith pair of coordinates (x_{Pi},y_{Pi}) are with respect to the world frame, but the ith corresponding measurements (x_{mi}, y_{mi}) that we acquire via the vision system are coordinates of point M with respect to the pattern frame (in this case, also the end-effector frame) which keeps moving during motion of XYΘ stages. Therefore, the measuring information must be transformed from pattern frame to world frame.

The relationship between the calculated vector $D^{WF} = [x_M - x_{Pi}, y_M - y_{Pi}]^T$ and the measured vector $D^{PF} = [x_{mi}, y_{mi}]^T$ is depicted by the following equation:

$$D^{WF} = T_{PF}^{WF} \cdot D^{PF}. \tag{4.25}$$

That is,

$$\begin{bmatrix} x_M - x_{Pi} \\ y_M - y_{Pi} \end{bmatrix} = \begin{bmatrix} x_{mi}\cos(\Theta_i) + y_{mi}\sin(\Theta_i) \\ -x_{mi}\sin(\Theta_i) + y_{mi}\cos(\Theta_i) \end{bmatrix}, \tag{4.26}$$

where

$$x_M = x_{m0},$$

$$y_M = y_{m0},$$

are initial measurements. The arbitrary position $P_i = (x_{Pi}, y_{Pi})$ in the world frame can be correlated with the measurement P_{mi} through following equation:

$$P_{mi} = \begin{bmatrix} x_{Pi} \\ y_{Pi} \end{bmatrix} = \begin{bmatrix} x_{m0} - x_{mi}cos(\Theta_i) - y_{mi}sin(\Theta_i) \\ y_{m0} + x_{mi}sin(\Theta_i) - y_{mi}cos(\Theta_i) \end{bmatrix}. \tag{4.27}$$

4.5.4 Parameters identification

Cost functions

Through minimizing the error between measured position P_{mi} and calculated position P_{ci}. The ith element of the cost function is defined as:

$$e_i = \varepsilon_{x_i}^2 + \varepsilon_{y_i}^2$$

where

$$\begin{cases} \varepsilon_{x_i} = x_{Pi} - x_{m0} + x_{mi}cos(\Theta_i) + y_{mi}sin(\Theta_i) \\ \varepsilon_{y_i} = y_{Pi} - y_{m0} - x_{mi}sin(\Theta_i) + y_{mi}cos(\Theta_i) \end{cases} \tag{4.28}$$

x_{m0} and y_{m0} can be eliminated by subtracting two poses,

$$\begin{cases} \varepsilon_{x_{i,j}} = \varepsilon_{x_i} - \varepsilon_{x_j} \\ \varepsilon_{y_{i,j}} = \varepsilon_{y_i} - \varepsilon_{y_j} \end{cases} \tag{4.29}$$

and x_{Pi} and y_{Pi} can be substituted by forward kinematics Eq. (4.18). The following cost function E can be defined with different pose combinations for n poses:

$$E = \varepsilon^T \varepsilon \tag{4.30}$$

where

$$\varepsilon = \begin{bmatrix} \varepsilon_{x_{1,2}} \\ \varepsilon_{y_{1,2}} \\ \varepsilon_{x_{2,3}} \\ \varepsilon_{y_{2,3}} \\ \vdots \\ \varepsilon_{x_{n-1,n}} \\ \varepsilon_{y_{n-1,n}} \end{bmatrix}, \text{with } 2(n-1) \text{ elements.}$$

Parameters identification turns into an optimization problem of minimizing E.

Identifiability analysis

In this case, all elements on the diagonal of the matrix R are not equal to zero, which means all parameters are identifiable. The QR decomposition of Jacobian can be done through software simulation. One example of the simulation results is:

$$R = \begin{pmatrix} 2.0077 & -1.7347e-18 & 0.5169 & 8.2052e-18 \\ & 2.0077 & 0.0158 & 8.3210e-17 \\ & & -464.5673 & -72.7559 \\ & 0 & & 168.8389 \end{pmatrix}.$$

The matrix demonstrates that all four geometric parameters are identifiable for two cost functions using randomly generated poses.

Observability analysis

Based on maximization of these indices, optimal number of poses and optimal poses can be selected. Fig. 4.21 shows the simulation results of observability with increasing number of random poses for cost function E. Among these indices, O_3 only takes into account the minimum singular value instead of both minimum and maximum singular values. Index O_1 was found to be worse than the others [61]. Hence, we mainly consider indices O_2 and O_4. In general, values of observability indices increase with the number of poses. However, there is no obvious change on index O_2 after about 400 poses indicating this number is the minimum. Meanwhile, the slope of index O_4 curve is getting smaller and smaller, which means taking more poses is getting less and less important. Moreover, index O_4 is an indicator of the amplification of sensor noise. To balance the best number and elimination of sensor noise, a trade-off between O_2 and O_4 is made that 1200 pairs of measurements will be taken.

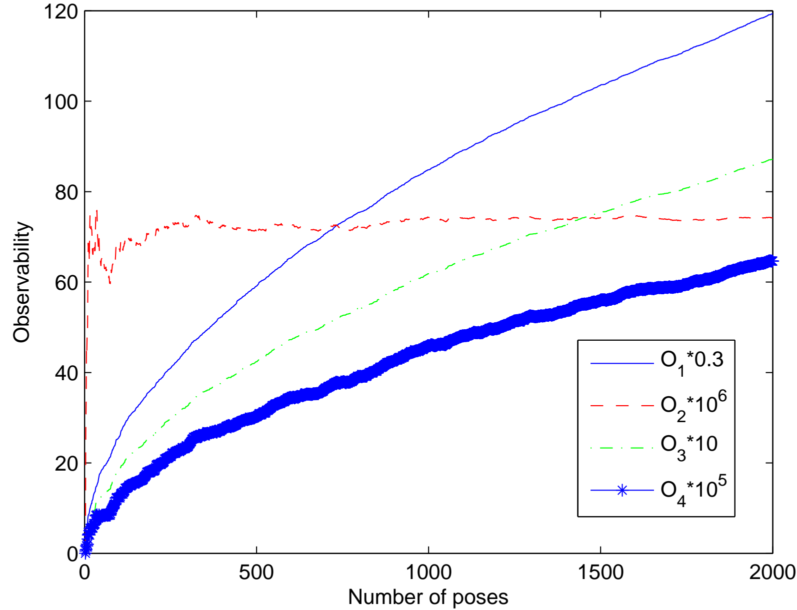

Figure 4.21: Observability of cost function E with 3 to 2000 poses.

4.5.5 Experimental identification and validation

Experiments are performed to identify the parameters and validate the performances implementing the five models. The results of identification and validation are presented as follows.

Data acquisition and parameters identification

To identify the kinematic parameters in Eq. (4.21), the first step is to acquire measuring information of the end-point. During data acquisition phase, the microrobotic system is commanded to reach a set of configurations by changing the translations and rotation joint coordinates. Meanwhile, the vision system captures all the images of the poses and retrieves the measuring information through Eq. (4.27). The defined trajectories of joint axes are shown in Fig. 4.22. This process takes about 1.3 hours. The number of measurements is chosen based on the observability analysis above. A total of 1200 pairs of measurements is obtained in data acquisition phase.

Geometric parameters are identified by solving nonlinear least-squares problem (using Matlab® function *lsqnonlin*). After identification, the parameters for five models are obtained and shown in Table 5.1. The modification of joint coordinates of X and Y axes considering position-dependent errors induces small differences of identified parameters between Model II and Model III. Models II and IV use the same values for these four parameters. The four parameters of Models III and V are the same. The validity of the

identified results have to be validated by implementing into the inverse kinematics of microrobotic system.

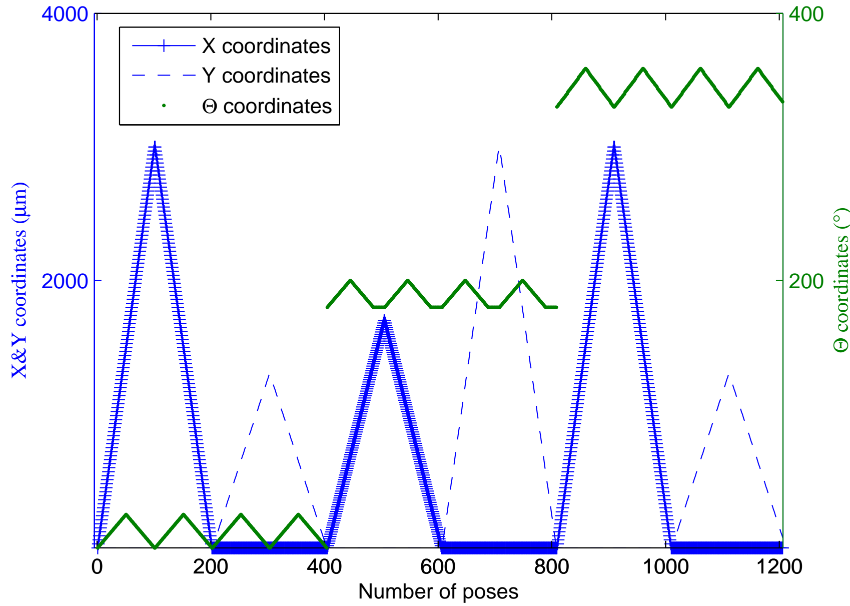

Figure 4.22: Joint coordinates of XYΘ stages in data acquisition.

Table 4.6: Geometric parameters for five models.

Identified parameters	$x_R(\mu m)$	$y_R(\mu m)$	$\alpha(°)$	$\beta(°)$
Model I	9572.902	7795.830	180	0
Model II	9572.902	7795.830	177.689	-0.132
Model III	9572.904	7795.858	177.685	-0.107
Model IV	9572.902	7795.830	177.689	-0.132
Model V	9572.904	7795.858	177.685	-0.107

Validation results

To test the performances of the microrobotic system using different calibration models, 9 target points (Table 4.7) in the world frame are chosen as validation points. The trajectory of validation follows P_0, P_1, ..., P_9 which is shown in Fig. 4.23. As in Fig. 4.24, the signal is processed in this procedure: 1) The target P_T is fed into the inverse kinematics and corresponding joint input P_c of the microrobotic system can be calculated; 2) the microrobotic system moves under the command P_c; 3) the measuring

system saves the images and retrieves the measurements information D_{PF} in the pattern frame; 4) the measurements are transformed into the value P_m with respect to the world frame. The validation results of positioning accuracy of the microrobotic system are shown in Fig. 4.25 and Table 4.8.

Table 4.7: Coordinates of five target points and rotation angles for validation.

Targets P_T	$x_T(\mu m)$	$y_T(\mu m)$	$\Theta_T(°)$
P_1	-1200	-200	1
P_2	-1600	-200	2
P_3	-2000	-200	3
P_4	-2000	-300	4
P_5	-1600	-300	5
P_6	-1200	-300	4
P_7	-1200	-400	3
P_8	-1600	-400	2
P_9	-2000	-400	1

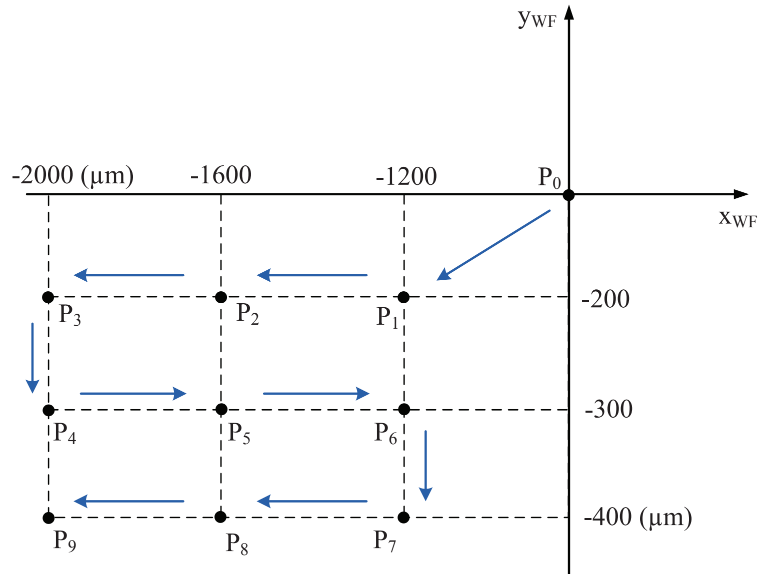

Figure 4.23: Moving sequence of target points (P_T) in validation.

The positioning accuracy using Model I (4.20) is approximately 100 μm. The accuracy becomes larger at the points further from the origin of the world frame which means the accuracy is highly influenced by the amplitudes of X and Y motions. This is due to the fact that the alignment parameter α and assembly error β are not taken into

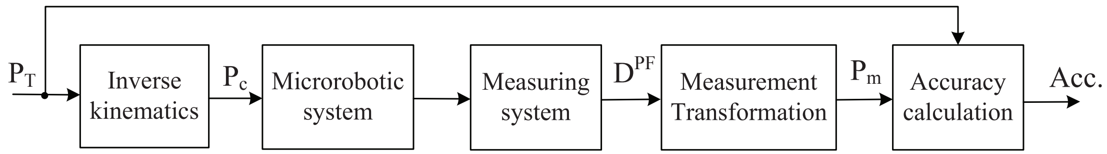

Figure 4.24: Block diagram of validation procedure.

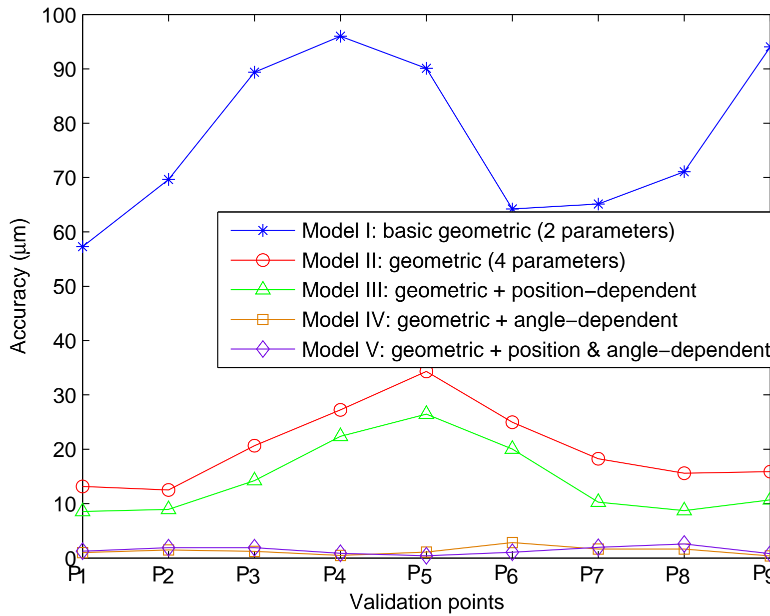

Figure 4.25: Experimental results of positioning accuracies using five models.

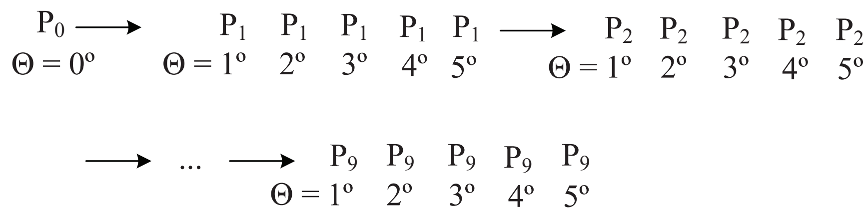

Figure 4.26: Moving sequence of target points (P_T) in measuring angle-dependent errors $f_{ax}(\Theta)$ and $f_{ay}(\Theta)$.

account in the model. The further the distance between the targets and the origin P_0 are, the larger the induced errors by the two angles are.

Thanks to the elimination of errors of α and β, the accuracy is improved a lot and reaches 35 μm. The accuracy curve achieved by Model II Eq. (4.21) demonstrates no

Table 4.8: Accuracy of different calibration models.

Model	Accuracy (μm)
Model I	95.980
Model II	34.338
Model III	26.461
Model IV	2.838
Model V	2.568

dependency with the distances between the targets and the origin, but demonstrates the dependency with rotation angles.

Moreover, compensation of position-dependent errors along X and Y axes can be reduced to reach nearly 10 μm of inaccuracy further with Model III (4.22). Similar to Model II, the accuracy curve of Model III also display dependency with rotation angle. The accuracy increases with the rotation angles.

To quantify the angle-dependent errors $f_{ax}(\Theta)$ and $f_{ay}(\Theta)$ in Model II and III, additional experiment is required to evaluate the residual errors. In the experiment, Model II and III are implemented to control the microrobotic system moving and following the target trajectory in Fig. 4.26. Every target position corresponds to 5 rotation angles. The positioning errors $f_{ax}(\Theta)$ and $f_{ay}(\Theta)$ at these poses form a lookup table through which $g_{ax}(\Theta)$ and $g_{ay}(\Theta)$ are calculated using inverse kinematics and added to the joint coordinate inputs. Implementing Model IV and V, the positioning accuracies are achieved to 2.8 and 2.5 μm respectively. The accuracies achieved by Model IV and V are quite close because quantified angle-dependent errors include a part of position-dependent errors.

In summary, different imperfections have different ways and amplitudes of influence on accuracy. The model selection is a tradeoff based on their model complexities and accuracies. Model I is for the most basic application. It requires little imperfection compensation except for the position of the rotation center.

The most influential parameters are α and β. So the performance-cost-ratio of Model II is high because these two parameters are easy to identify and, by compensating them, the accuracy improves by about 60 % with Model II.

Angle-dependent errors are also very significant. A 5° rotation induces nearly 20 μm inaccuracy. To achieve best performances, Model IV and V should be chosen and of course, more efforts must be made on measurement and calibration.

Position-dependent errors are relatively less important than other two kinds of imperfections which generate inaccuracy about $5 \sim 8$ μm. However, the complexities of Model II and III are lower than Model IV and V. So if only medium level of accuracy is required, the former two models are working.

4.6 Conclusions

This chapter aims at understanding and quantifying the influences of different imperfections and improving the positioning accuracy of microrobotic systems.

First, we presented the generic framework including general modeling, discussion about sources of imperfections, and parameter identification for microrobotic calibration that we used. This calibration framework could be embodied, extended, and applied to a wide range of structures of microrobots.

Second, as a preliminary step for calibration of the whole microrobotic system, the position-dependent errors along XY stages were characterized and compensated. The errors were measured and quantified to form a lookup table for compensation. Validation tests via trajectory tracking and random points positioning showed distinct improvement of positioning accuracy with 86% (from 22 μm to 3 μm) and 68% (from 22 μm to 7 μm) inaccuracy reduction, respectively.

Third, a serial microrobotic system with 3-DoF XYΘ is chosen as a case study because of its popularity in microscale applications and inclusion of most imperfections known in microrobots. Kinematic modeling of five models was proposed to depict and control the microrobotic system. The most significant sources of inaccuracy are tackled in the descending order, which are rotation center, alignment and assembly errors, position-dependent errors, and angle-dependent errors. Number of measuring poses is determined based on observability analysis. Experimental validations of five models have demonstrated substantial improvement of static positioning accuracy, showing 97% reduction (from 96 μm to 2.5 μm) in experimental results. Five models take into account different sources of inaccuracy at the microscale, and different levels of accuracy are achieved. Five models can be selected according to the required accuracy of the applications. In our case, if the required accuracy in an application is lower than 100 μm, according to the result of Model I, alignment error and perpendicularity error could be neglected and nominal parameters are sufficient. If the required accuracy is better than 40 μm, these two errors must to be compensated. Moreover, further 10 μm can be reduced by Model III making efforts of compensating position-dependent errors along X and Y axes. The best accuracies achieved by Model IV and V are better than 3 μm with angle-dependent errors compensation, which already reaches the limitation of the microrobotic system.

In many applications involving rotation stages, coordinates of rotation center (x_R,y_R) are a basic requirement to know in applications. Model I is the basic model meeting such requirement. The most influent parameters α and β identified in Model II are mounting errors due to manual assembly. Model III, IV, and V are advanced models requiring advanced knowledge of the microscale specificities on joint coordinates of XYΘ axes.

The generic framework can be generalized and applied to any common multi-DoF microrobotic systems (for example, $XYZ\Theta_x\Theta_y$). We can imagine that, in the future, the framework will becomes concretely a toolbox or library inclusive plenty of functional modules and knowledge documents. To perform a calibration task, users from robotic community could input the forward and inverse kinematics into the framework, and choose the model module based on their available measuring devices, source of inaccuracy

acting on their systems. After that, the calibration runs automatically. Normally, higher accuracy requires more input information. To get help from this, users could benefit from its accessibility, versatility as well as expandability. The framework paves the way for efficient interesting calibration solution for microrobotic systems.

Chapter 5

Calibration of Nanopositioning Stages

5.1 Introduction

This chapter is about calibration of nanopositioning stages. Nanopositioning stages are often combined with micropositioning stages which enable to achieve coarse-fine positioning. In Chapter 4, we have seen that we can achieve positioning accuracy in the range of a few microns with only micropositioning stages. Nanopositioning will thus aim at going one step further, that is, to achieve accuracy in 100 nm range in ambient environment (objective defined in Chapter 3). In general, nanopositioning systems with frictionless flexure guidance are superior to conventional guiding systems (bearings, etc.) in terms of resolution, repeatability, straightness and flatness. They can easily achieve repeatability of dozens of nanometers and resolution better than 10 nm based on the elastic deformation of a solid material. They have small strokes from a few tens of microns to about 500 μm. The flexible structure prevents any mechanical drawbacks, such as backlash or friction.

However, there is still nonlinear coupling behavior due to the intrinsic actuation and guiding principle of the stages. Such stages also require complex actuators and sensors integration. Inaccuracy may come from the deficient actuation model and/or indirect measurement. The motions of most nanopositioning stages are generated through a motion amplification system transferring local and small motions into large motions. For every stage, there is a model linking the flexure motion and motion of the mobile part. If the model is not accurate enough to depict this relation, the real motion of the stage will not match up what we input. In addition, external disturbances may affect the motion behavior so that the original model is unable to depict the real relation. For example, the temperature variation may induce big positioning errors, typically 1 $\mu m/°C$ as shown in Chapter 2. Inaccuracy may also come from indirect measurement of the stage motion. For an internal sensor, such as a strain gauge sensor, it measures indirectly, in that the position of the moving platform is inferred from a measurement

at the lever, flexure or stack. In this case, to achieve accurately positioning, an external sensor is required to make direct measurement.

This chapter presents problem formulation, modeling, and experimental validation for calibration of nanopositioning stage with thermal drift compensation. A single-axis nanopositioning stage and multi-DoF nanocube are chosen as the case studies, because such kind of stages is typical and commonly used for fine positioning in micro and nanomanipulation platforms and will enable to study the influence of main sources of inaccuracy usually affecting nanopositioning systems.

5.2 Modeling and identification of 1-DoF nanopositioning stage

Nanopositioning stage suffers from geometric errors and environmental effects which is mainly due to temperature change. Both come from different sources, we will construct different models to decouple their influence.

5.2.1 Geometric modeling

Geometric errors at the microscale are the main nonlinearities inherent in the nanopositioning stage. To model them, basic measurement of the errors behavior should be conducted. The nanopositioning stage is controlled to reach some positions and the actual positions are measured by an external sensor (in this case, an interferometer). Fig. 5.1 (a) shows the position-dependent errors of the nanopositioning stage measured using this external sensor and the one provided by the nanopositioning stage supplier. In this figure, the curves of the errors are cubic functions (3rd order) each with two critical points. It is worth mentioning that the positioning errors are significant (up to 400 nm) for nanopositioning, even though the stage has already been closed loop controller at the actuator layer. The peak-valley value measured by the supplier is also around 400 nm. The error curve has been moved in parallel which is due to long term use. This error is repeatable which means it can be compensated through calibration enabling to reach errors down to some tens of nanometers.

For the sake of convenience, we investigate inverse kinematic modeling directly instead of first forward kinematics and then inverse kinematics. The following model is chosen:

$$q_g = \sum_{i=0}^{n1} a_i x^i, \tag{5.1}$$

where q_g is the joint input which is usually the motors coordinates of the robot; x is the measured position by external sensor; $a_1, \ldots, a_{n1}$ are geometric coefficients; $n1$ is the order of the geometric model (here, n1=3). At the same time for the same x coordinates, the coupling errors y_m in y direction measure about 75 nm (Fig. 5.1) (b).

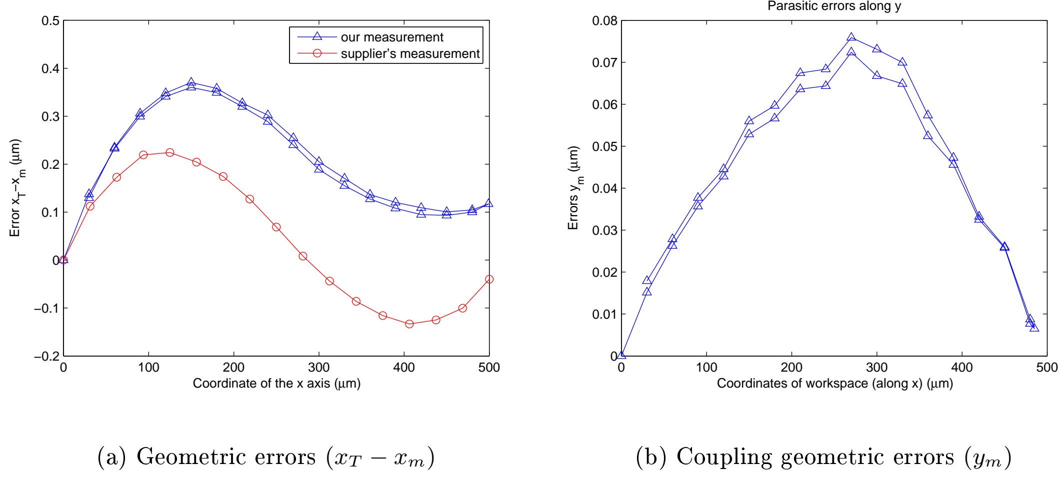

(a) Geometric errors ($x_T - x_m$)

(b) Coupling geometric errors (y_m)

Figure 5.1: Geometric errors of the nanopositioning stage in forward and backward motions. x_T is the target, x_m is the measured position along x, y_m is the measured position along y.

5.2.2 Thermal-drift modeling

There are two main sets of methods for thermal-drift modeling, which are principle-based methods and empirical-based methods [47]. The heat transfer model of the compact and small-sized system is very complex depending on system geometry which is difficult to be built analytically. So we decide to educe it through empirical-based method which is suitable for modeling the relation between temperature variation and part deformation. The thermal model is based on the quasi-static assumption that thermal errors vary slowly with time and are only related to the mechanical structure. However, thermal drift has static and dynamic aspects which is complex and difficult to model accurately, especially at the microscale. During a period of time, the behavior mode of thermal drift is static which can be modeled by the single model. However, the behavior mode would be dynamic that the previous model could not fit the drift as efficient as before. Here we construct single and adaptive models to tackle static and dynamic effects.

Thermal-drift measurement

Except for geometric errors, the system is also highly susceptible to thermal disturbances. To choose a suitable calibration model considering thermal effect in room environment, we have to perform an experiment to characterize the relation between temperature and drift. In this experiment, the interferometer is used to measure the position of the switched-off nanopositioning stage. The interferometer is defined as a global frame in two days of measurement. Even though without moving control input, the interferometer detects the drift of the stage. Fig. 5.2 (a) shows that there is a drift increasing with the

temperature decreasing in an opposite way. Fig. 5.2 (b) shows a roughly linear relation between temperature variation and position drift.

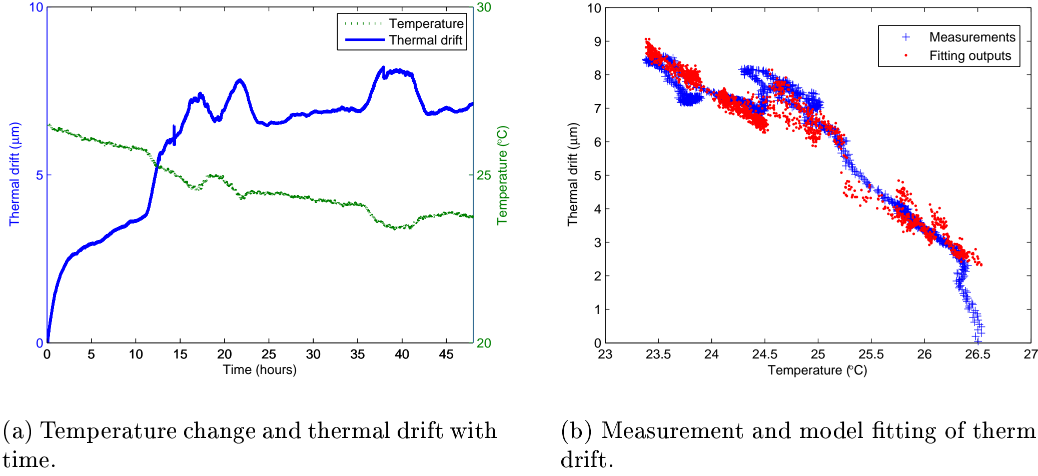

(a) Temperature change and thermal drift with time.

(b) Measurement and model fitting of thermal drift.

Figure 5.2: Relationship between temperature and thermal drift

Modeling

The drift is mainly due to the thermal elongation δ in different parts of the stage. Considering a ideal and simple case, the elongation δ can be computed based on the following 1-D equation:

$$\delta = L - L_0 = L \cdot \alpha \cdot (T - T_0),$$

where δ is the drift to be compensated; L_0 is the length at reference temperature T_0; α is thermal-expansion coefficient; L is the length of component after elongation due to temperature change $T - T_0$. The whole thermal drift of the nanopositioning cell is composed of thermal-expansion of different parts. Therefore, the 1st order relationship between the temperature and the drift is the modeling foundation.

Moreover, considering the nonuniform temperature field and nonlinear combination of thermal expansions, we monitor temperatures at several points of the workspace and have the thermal-drift model [55]:

$$q_t = \sum_{i=1}^{n2} b_i t_i + b_0 \tag{5.2}$$

where q_t is thermal compensation input; t_i is ith measured temperature and b_i is the corresponding coefficient; b_0 plays a role of bias; $n2$ is the order thermal-drift model. The model correlates temperature field to the induced drift through coefficients $b_1, \ldots, b_{n2}$.

Using this model we can approximate the thermal drift with temperature information, and the fitting result is shown in Fig. 5.2 (b). To determine the suitable model, we tried higher order thermal-drift model, but the they did not provide better results.

Besides, relative humidity is also measured at the same time. However, its evolution does not display any correlation to the drift. Therefore, humidity information is not taken into account in the model.

5.2.3 Single model

Combining geometric model and thermal drift model yields the complete model [83]:

$$q = \sum_{i=1}^{n1} a_i x^i + \sum_{i=1}^{n2} b_i t_i + \lambda, \tag{5.3}$$

where $\lambda = a_0 + b_0$. This model is chosen because it is a tradeoff of simple and "straightforward" physical meaning which help to know better the behavior, and to exploit a more powerful model in the future. Obtaining high fitting precision (submicrons) requires a set of measuring data for training:

$$\begin{bmatrix} q_1 \\ \vdots \\ q_m \end{bmatrix} = \sum_{i=1}^{n1} a_i \begin{bmatrix} x_1^i \\ \vdots \\ x_m^i \end{bmatrix} + \sum_{i=1}^{n2} b_i \begin{bmatrix} t_{i,1} \\ \vdots \\ t_{i,m} \end{bmatrix} + \lambda, \tag{5.4}$$

where m is the number of the pose measurements. The equation could be written as matrix form:

$$\begin{bmatrix} q_1 \\ \vdots \\ q_m \end{bmatrix} = \begin{bmatrix} x_1^1 & x_1^2 & \dots & x_1^{n1} & t_{1,1} & \dots & t_{n2,1} \\ \vdots & \vdots & \vdots & \vdots & \vdots & \vdots & \vdots \\ x_m^1 & x_m^2 & \dots & x_m^{n1} & t_{1,m} & \dots & t_{n2,m} \end{bmatrix} \begin{bmatrix} a_1 \\ \vdots \\ a_{n1} \\ b_1 \\ \vdots \\ b_{n2} \end{bmatrix} + \lambda. \tag{5.5}$$

To perform training and parameters identification, the stepwise regression ($Matlab^{®}$, $StatisticsToolbox^{TM}$) is used because it is able to automatically search the coefficients space and keeps the most influential ones by calculating the p-value of F-statistic. The algorithm could be implemented conveniently by a Matlab function $stepwisefit$.

Fig. 5.3 is the block diagram of the nanopositioning stage working in closed loop at actuator layer and in open loop at planning layer. A PID control is used for closed loop control in actuator layer. The control input q_c is calculated by the calibrated model with desired target q_T and measured temperature t. The mobile part moves in closed loop control in actuator layer. In the case of the system without calibrated model, the control input is directly q_T without processing with the model.

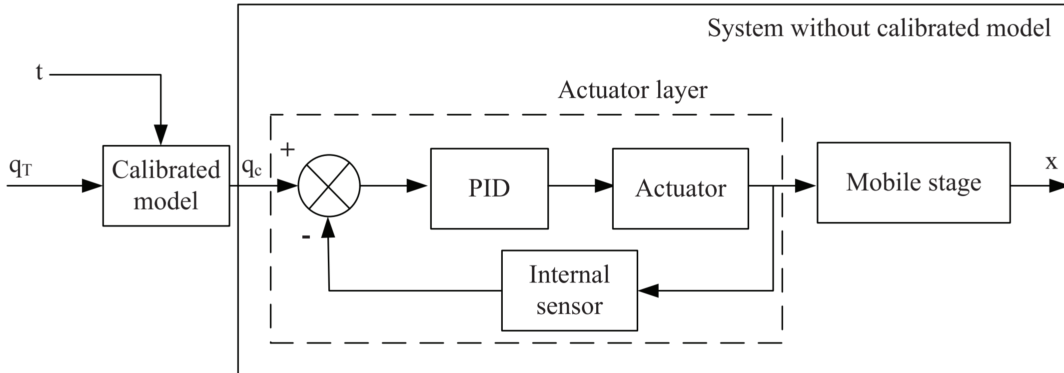

Figure 5.3: Block diagram of the system with single calibrated model.

5.2.4 Adaptive model using kiloMeter-Zero (KMZ)

Thermal behavior is complex and difficult to model accurately, especially at the microscale. During a period of time, the behavior mode of thermal drift is static which can be modeled by the single model. However, the behavior mode would be dynamic, so previous model could not fit the drift as efficient as before. On one hand, we need to construct a single feedforward model to compensate the static aspect of thermal drift. On the other hand, because the behavior mode of thermal drift is dynamic, we need to update the drift information when mode changes. Close-loop control in planning layer is robust to such change, however, accurate control requires multi-DoF sensors to be kept on the nanopositioning robot. Therefore, we propose an adaptive way adapting the model to compensate the dynamic aspect of thermal drift in the long term. Here, a method based on kiloMeter-Zero (KMZ) is introduced in case drift modeling is not sufficient.

KMZ is a trade off strategy which enables to integrate a small sensor which could be a part of the robot, this sensor must be high resolution and could have very limited measurement range. With this integrated sensor, we can obtain the drift information from time to time in closed loop and use open loop control most of the time to keep fast response time and high accuracy without using bulky and costly sensors for full closed loop.

Based on the knowledge that the thermal drift is position-independent, we propose to make measurement of the thermal drift at a local position, and then use this information to the whole stroke of the stage. To do that, we need to define an absolute frame to which the drift refers. We call this frame as the KMZ. This frame can be defined by a sensor performing direct measurement, or a fixed precise tool (e.g., a fixed AFM tip). In this chapter, we use the interferometer to define the KMZ. The working principle of adaptive model using kilometer-zero is as follows:

- define an absolute reference point (we call it kilometer-zero) using a sensor or a fixed precise tool globally.

- reach the kilometer-zero and record the measurement of the sensor.
- after a period of time, re-reach the kilometer-zero again and record the new measurement.
- the drift between the first and second reaching is the difference of two measurements of the sensor.
- the drift can be compensated by adding the calculated difference.

One adaptive model using KMZ is:

$$q = \sum_{i=0}^{n1} a_i x^i + \lambda_{KMZ}. \tag{5.6}$$

The first term of Eq. (5.6) is the same as that of the single model which compensate only the geometric errors. λ_{KMZ} is the drift detected by reaching the KMZ. In the following experimental studies, the adaptive models all refer to Eq. (5.6). In addition, we can also use the following model:

$$q = \sum_{i=1}^{n1} a_i x^i + \sum_{i=1}^{n2} b_i t_i + \lambda + \lambda_{KMZ}. \tag{5.7}$$

The block diagram of this adaptive model using kilometer zero is shown in Fig. 5.4. This adaptive model is a trade-off between geometric or single model and closed loop control in planning layer.

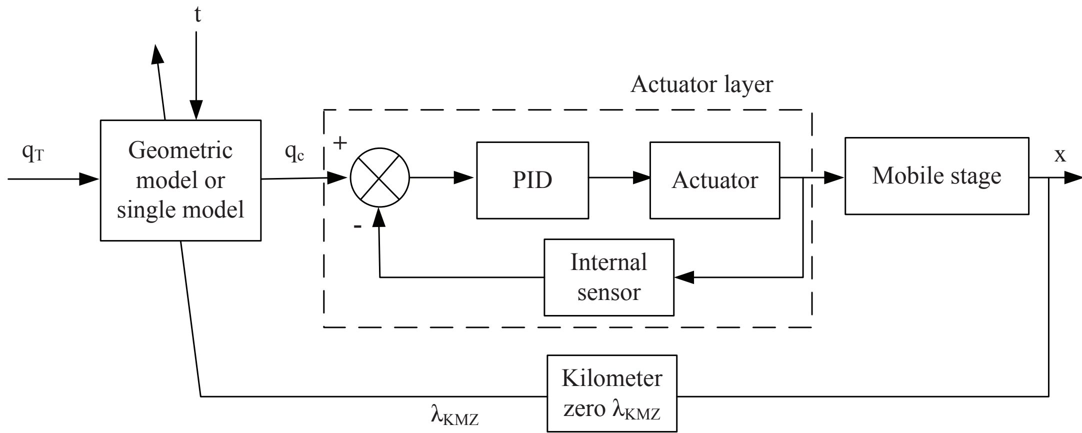

Figure 5.4: Block diagram of the system with adaptive model using kilometer zero.

With compensation using the adaptive model, $q_c = x_T + g'(x_T) + L'(t) + \lambda_{KMZ}$ replaces x_T as control input. In a given test, the ith position measurement x_{mi} corre-

sponding to target x_T is:

$$\begin{aligned} x_{mi} &= G_i(q) + L_i(t) \\ &= g_i(q) + P_i(q) + q + L_i(t) \\ &= g_i(x_T + g_i'(x_T) + L'(t) + \lambda_{KMZ}) + P_i(x_T + g_i'(x_T) + L'(t) + \lambda_{KMZ}) \\ &+ x_T + g_i'(x_T) + \lambda_{KMZ} + L_i(t) \\ &= g_i(x_T) + P_i(x_T) + x_T + g_i'(x_T) + \lambda_{KMZ} + L_i(t) \\ &= P_i(x_T) + x_T + \lambda_{KMZ} + L_i(t). \end{aligned}$$

Similar to the analysis in Chapter 3, $g(x_T + g'(x_T) + L'(t) + \lambda_{KMZ}) \approx g(x_T)$ and $P(x_T + g'(x_T) + L'(t) + \lambda_{KMZ}) \approx P(x_T)$, because $g'(x_T) + L'(t) + \lambda_{KMZ}$ is small.

The accuracy AP_A is expressed as:

$$\begin{aligned} AP_A &= \left| \frac{1}{n} \sum_{i=1}^{n} x_m - x_T \right| \\ &= \left| \frac{1}{n} \sum_{i=1}^{n} [P_i(x_T) + x_T + \lambda_{KMZ} + L_i(t)] - x_T \right| \\ &= \left| \frac{1}{n} \sum_{i=1}^{n} P_i(x_T) + \frac{1}{n} \sum_{i=1}^{n} [\lambda_{KMZ} + L_i(t)] \right| \end{aligned}$$

where λ_{KMZ} is only measured at the first zero position, so λ_{KMZ}=-$L_1(t)$, when x_T=0. Then the accuracy becomes

$$AP_A = \left| \frac{1}{n} \sum_{i=1}^{n} P_i(x_T) + \frac{1}{n} \sum_{i=2}^{n} [\lambda_{KMZ} + L_i(t)] \right|$$

If $L_i(t)$, $i \neq 1$ is very close to $L_1(t)$ due to small temperature change, then λ_{KMZ}=-$L_i(t)$, we have:

$$AP_A = \left| \frac{1}{n} \sum_{i=1}^{n} P_i(x_T) + \delta \right|, \delta \longrightarrow 0$$

Therefore, if the temperature change within the test is very small, the accuracy after compensation could be the level of that without geometric error and external error which is the highest accuracy theoretically. However, in most cases, the temperature change is not small in the long term.

Moreover, because temperature change is relatively slow in the normal micromanipulation laboratories, the frequency of visiting the kilometer-zero could be adjusted based on the temperature magnitude and changing rate.

5.2.5 Robustness criterion

There are some works about calibration of macro or micro robots with thermal compensation. However, few of them investigates the robustness of calibration which is very important for practical applications. To evaluate robustness of calibration, we propose to define a performance criterion, calibration robustness, in nanopositioning calibration. Robustness is classified into two types: space and time robustness. Space robustness defines the uniformity of the positioning accuracy of different positions in the whole workspace. The calculation equation is:

$$R_S = \frac{1}{n}\sum_{i=1}^{n}[Max(AP_i) - Min(AP_i)]. \tag{5.8}$$

which evaluates the sum of deviations between the maximum and minimum accuracies of all tests in a period of time.

Time robustness defines the uniformity of the positioning accuracy in the whole process. The calculation equation is:

$$R_T = \frac{\frac{1}{n}\sum_{i=1}^{n} Max(AP_i)}{Time}. \tag{5.9}$$

which evaluates the sum of maximum accuracies of all tests in a period of time.

The smaller values of R_S and R_T are, the better space and time robustness are.

5.3 Experimental study of 1-DoF nanopositioning stage

This section presents the experimental case study of accuracy of a nanopositioning stage using three models to (i) quantify the performance improvement, and (ii) identify the most influential factors. The three models are original model (without calibrated model), single model in Eq. (5.3), and adaptive model using KMZ in Eq. (5.6).

5.3.1 Experimental setup

As shown in Fig. 5.5, the experimental setup consists of a single-axis nanopositioning stage P-625.1CD (Physik Instrumente), two laser interferometer sensor heads (SP-S 120 SIOS Meßtechnik GmbH) with a resolution of 0.3 nm, and four K type thermocouples and a barometric pressure sensor. The nanopositioning stage is controlled in closed-loop (PID) at actuator layer with internal capacitive sensor. The positioning resolution is 1.4 nm according to company datasheet. The interferometer defines the global frame during training and validation by setting the initial reading at the beginning of training phase as zero.

According to Chapter 2, the three main measuring uncertainties of the interferometer system come from the wavelength compensation, deadpath correction and material thermal compensation. Here, wavelength compensation and deadpath correction are realized by built-in temperature/pressure-correction module (incorporates a temperature sensor

Pt100 and barometric-pressure sensor as seen in Fig. 5.5). Also in Chapter 2, we obtain the measurement uncertainty of less than 41 nm.

Four thermocouples are placed around the nanopositioning stage to monitor the temperature change. Even though the measurements of these thermocouples are close, there are still some minor differences. At the microscale, these minor differences are important for precise building an accurate model. Hence, several thermocouples are required. So far, nobody succeeds in defining where are the good locations to be measured. In addition, the experimental setup is covered by a shield against air flow.

Fig. 5.6 shows the hardware allocation and signal flow. The controller sends the control input q to the nanopositioning stage and receives measurement $x_{internal}$ from internal sensor for closed loop control in actuator layer. The stage reaches position x_{real}, y_{real}. Measurements x_m, y_m are obtained by interferometers. A Dspace board connected with the PC is the hub of signal flow.

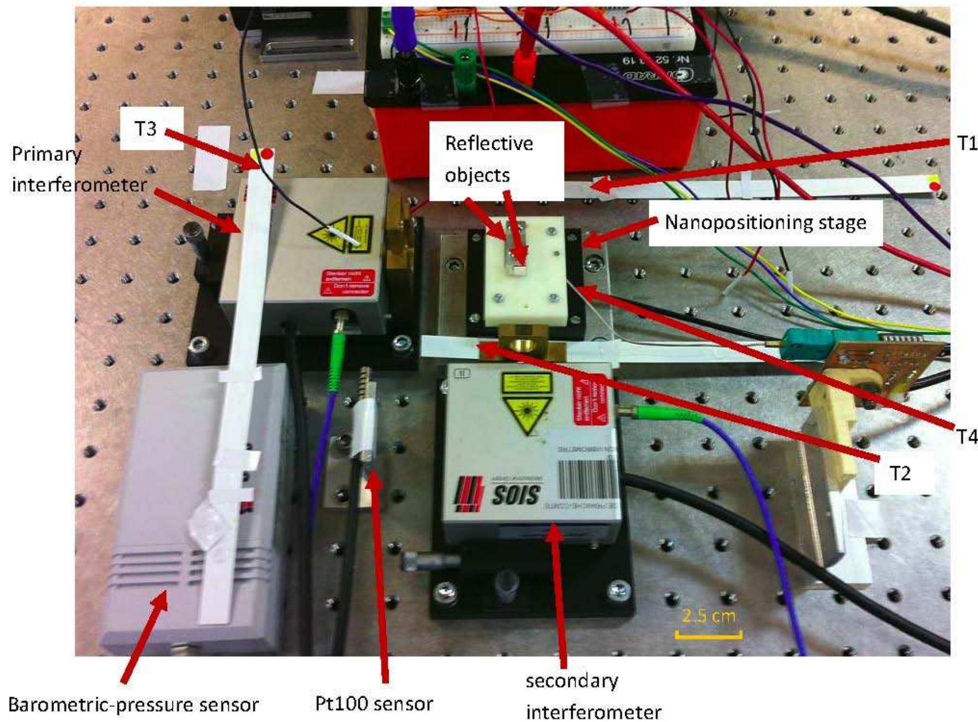

Figure 5.5: Experimental setup comprising one single-axis nanopositioning stage and reflective object, two interferometers with affiliated pressure/temperature sensors, four temperature sensors.

5.3.2 Procedures of calibration and validation

The whole procedure of the calibration using single model is shown in Fig. 5.7 which includes measurement, training, and validation phases. In measurement phase, a few

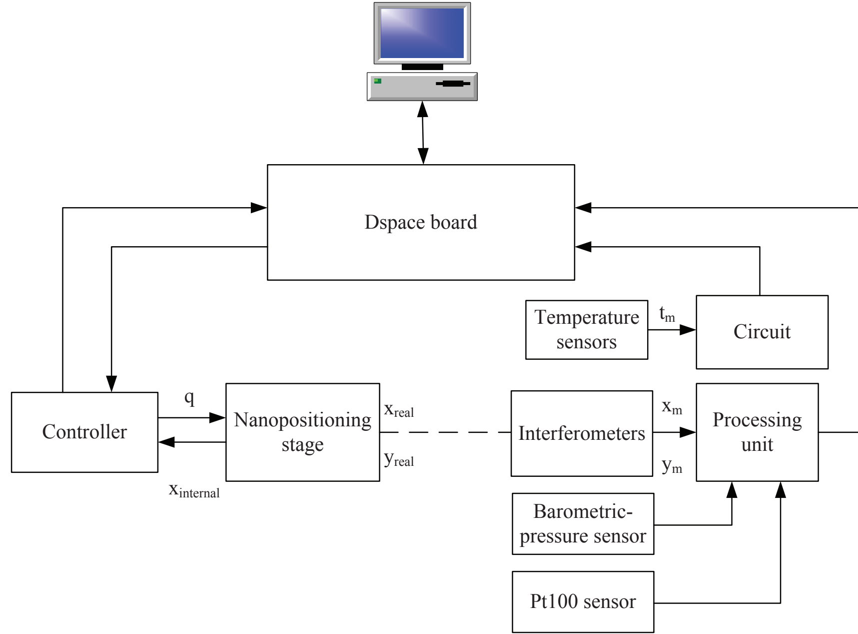

Figure 5.6: Schematic diagram of the hardware allocation and signal flow.

target points q along the axis are defined; the nanopositioning stage is controlled to reach these positions; the external sensor records the real position x and the thermocouples record the temperature t during this phase. Subsequently, based on the inverse model, parameters are identified using all information (q, x, and t). For implementing the calibrated model, we first define target points x', and then calculate the corresponding joint coordinates q' using the identified parameters and the model. The nanopositioning stage is controlled to move for performance validation. Finally, the real positions x'' are measured and used to calculate the accuracy achieved.

Firstly, we need to acquire position information for model training through external measurement. The workspace of the nanopositioning stage is a line of 500 μm. We define the joint coordinates of the moving trajectory (named training trajectory) at 0:30:480 μm. The reference trajectory is shown in Fig. 5.8 which demonstrates that, in every cycle, the rising time of the input signal is 4 seconds and the input keeps constant 25 seconds before the next in order to have stable state. The average values in the last 5 seconds of every step are considered as the measurements x and used for training. Meanwhile, four thermocouples obtain a set of temperature data t. Data acquisition takes about 12 hours for 24 cycles. All the data are fed into Stepwise algorithm for training. Afterwards, the identified parameters C are embedded into the controller.

Fig. 5.9 shows the validation trajectory. The test points x' for validation are taken at coordinates 0 80 160 240 320 400 480 μm. These points include the ones (0 240 480) also considered in training and the ones (80 160 320 400) never used for training. Validating the points both inside and outside the training set helps to evaluate performances of

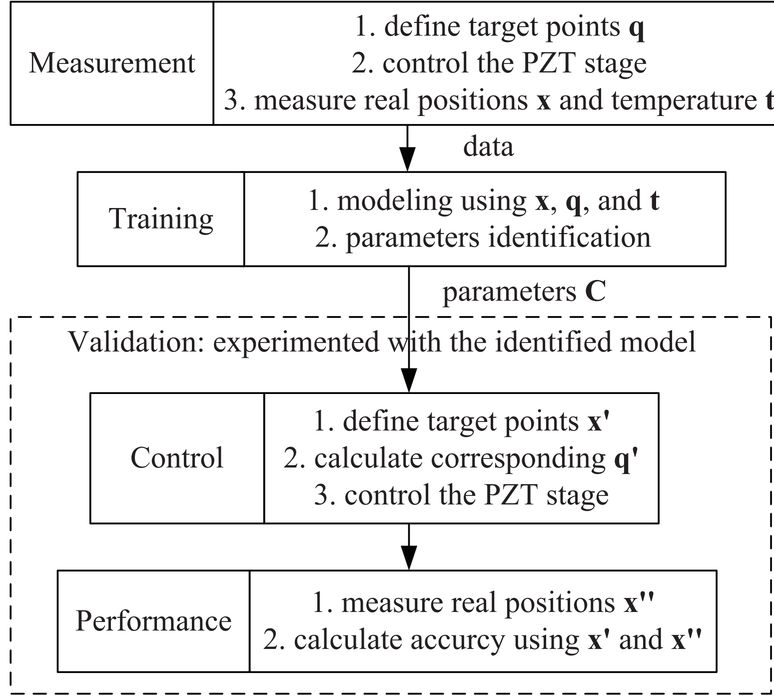

Figure 5.7: Flow chart of calibration of nanopositioning stage considering thermal drift.

both robustness and generalization (or interpolation). Every test of validation takes about 1.25 hours for 15 cycles of forward and backward motion.

5.3.3 Experimental results and discussions

Performance under constant temperature

The first experiment tests the positioning accuracy and repeatability of the nanopositioning stage without calibrated model in a metrology room with temperature control in order to decouple the geometric errors and the thermal effect. The temperature is controlled to keep "stable" inside the room. Fig. 5.10 shows the temperature deviation is within $\pm$ 0.05 $°C$.

The positioning accuracy measured by 1-DoF interferometer is showed in Fig. 5.11. In 15 cycles forward and backward motions, the accuracy is 350 nm which is only geometric aspect AP_I defined in *Remark 1*. In the environment with constant temperature, this value results from the intrinsic and position-dependent errors. The difference between the accuracies of the forward and backward motion is quite small (about 10 nm) which means the hysteresis of the stage has been eliminated well by the closed loop control in actuator layer.

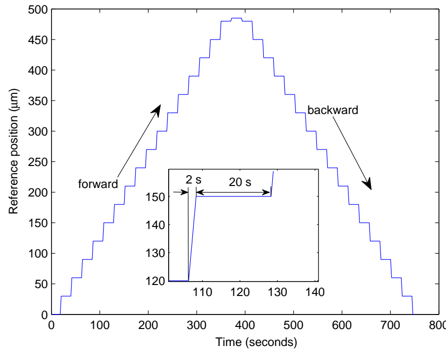

Figure 5.8: Reference trajectory of measurement for one cycle.

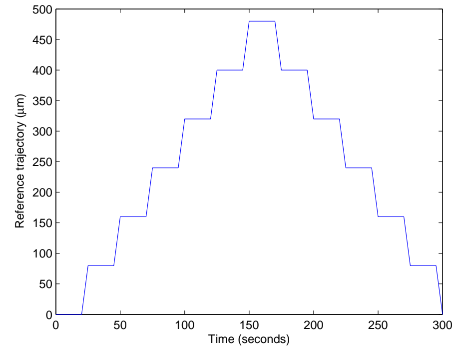

Figure 5.9: Reference validation trajectory.

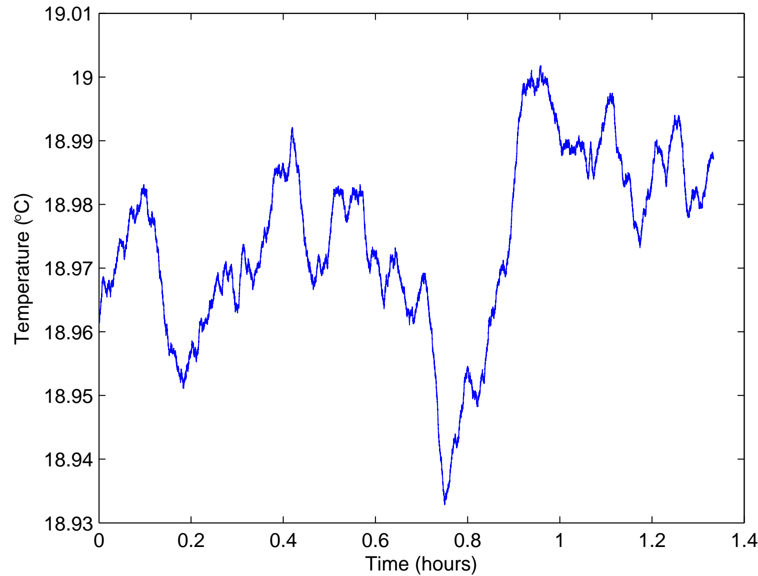

Figure 5.10: Temperature during the experiment in metrology room.

The corresponding repeatability is about 35 nm shown in Fig. 5.12. This value is induced by the controller and internal sensor which is considered as the intrinsic characteristics defined as RP_I in *Remark 1*.

Performances under varying temperature

The calibration procedure follows the flow chart in Fig. 5.7. The duration of training step is about 14 hours with 67 cycles of forward and backward motions. Every cycle = 18 poses (forward) + 16 poses (backward). After achieving the training, identified parameters of

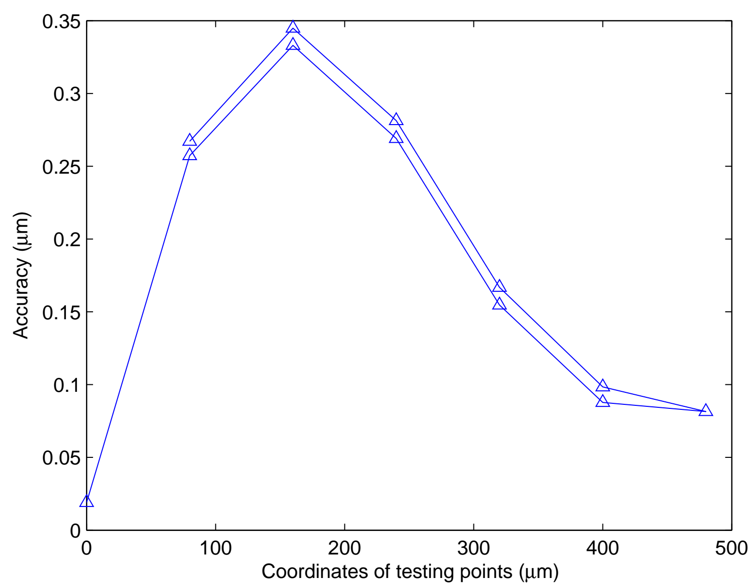

Figure 5.11: Accuracies of the nanopositioning stage in forward and backward motions without calibration in metrology room.

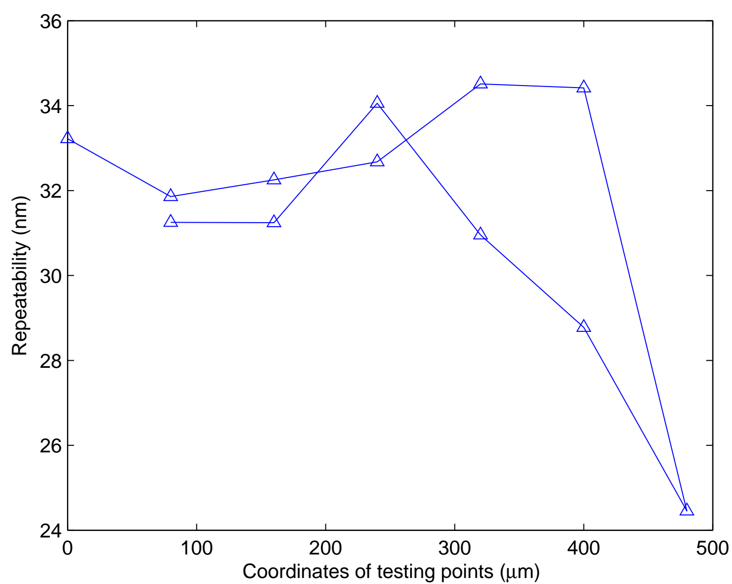

Figure 5.12: Repeatability of the nanopositioning stage without calibration in metrology room.

the model are obtained and shown in Table 5.1. Validation tests are then performed which aim at quantifying performances of the calibrated nanopositioning robot. Every validation test takes 1.25 hours for 15 cycles of forward and backward motions. Validation tests are performed in the repeating order of: with no calibration, with adaptive model using KMZ, and with single model.

Table 5.1: Identified parameters of single model.

Parameters	Values
a_1	2.454×10^{-8}
a_2	-2.167×10^{-5}
a_3	1.005
b_1	2.978
b_2	-3.142
b_3	-0.996
b_4	0.690
λ	10.413 (μm)

Among the accuracies of 34 poses in training phase (TP), the maximum value is more than 450 nm and the minimum is about 150 nm in forward and backward motions as depicted in Fig. 5.13. The accuracy of the first validation test (T1) with no calibration is showed in Fig. 5.14. Accuracies of different poses are quite different in the curves of no calibration. The difference between the maximum (650 nm) and minimum (350 nm) is about 300 nm which is close to that of TP. Both of the accuracy curves of TP and T1 are with the similar shape as well as that in Fig. 5.11. This is because thermal effect acts on all the positions and deviates them equivalently. The second (T2) and third (T3) tests are with adaptive model using KMZ and single model respectively. The corresponding accuracies of the two tests are shown in Fig. 5.15 and 5.16. The largest accuracies are about 43 nm in T2 and 95 nm in T3 which are much smaller than those without calibration. Accuracies on different points become much more closer. The difference is about 35 nm in T2 and is about 40 nm in T3. These results show that the two calibration models not only improve the overall accuracy, but also decrease the performance differences between different points in the workspace. Fig. 5.17 shows the accuracy evolution of all validation points in five days.

Picking up the maximum accuracy and repeatability of every test forms the Fig. 5.18. The accuracy of no calibration reaches 1 μm and keep larger than 400 nm during the whole process. These results suffer from the temperature influence which are different from that ($<$ 400 nm) in Fig. 5.11 where temperature influence is negligible. Single model performs good positioning accuracy (smaller than 0.4 μm) in the first 3 days and deteriorates afterwards. Adaptive model using KMZ achieves always accuracy better than 0.2 μm. Hence, the single model can provide much better performance than no

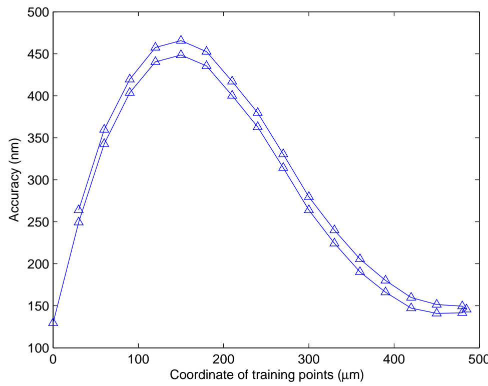

Figure 5.13: Accuracy in training phase (T-P).

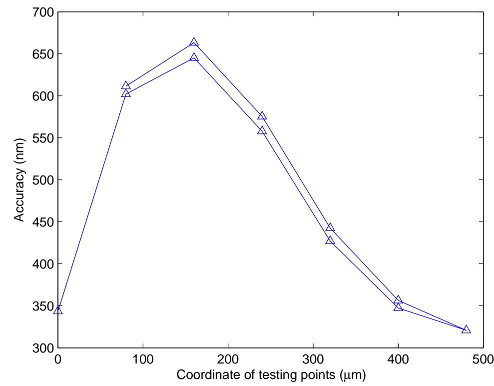

Figure 5.14: Accuracy of the first test without calibration (T1).

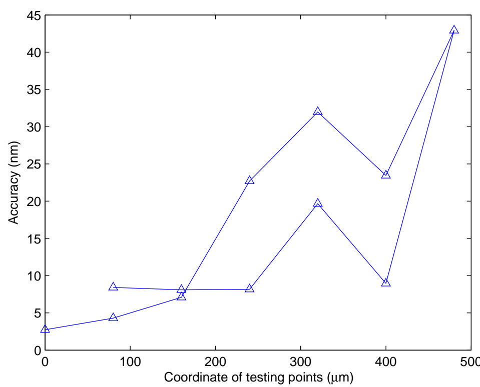

Figure 5.15: Accuracy of the second test with adaptive model using KMZ (T2).

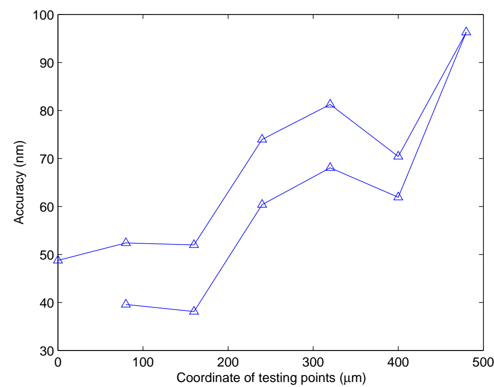

Figure 5.16: Accuracy of the third test with single model (T3).

calibration. If we want to achieve longer term good performance, the adaptive model must be used.

Fig. 5.19 shows the temperature evolution inside the room during the validation. Temperature change is relatively regular in first 50 hours, and the variations are about $0.2 \sim 0.3\ ^{\circ}C$ which is basically within the temperature range of training phase. In the latter 2 days, temperature changes $1.3\ ^{\circ}C$. Fig. 5.20 illustrates the relationship between temperature and accuracy/repeatability. The accuracy of adaptive model is not sensitive to temperature change no matter the temperature is in the range of training or not. When in the same range as or close to training phase temperature, accuracies of single model are almost better than 300 nm. But is getting much larger when temperature goes out of the temperature range of training phase. This means the performance of the single model largely depends on the training information. If the drift behavior and

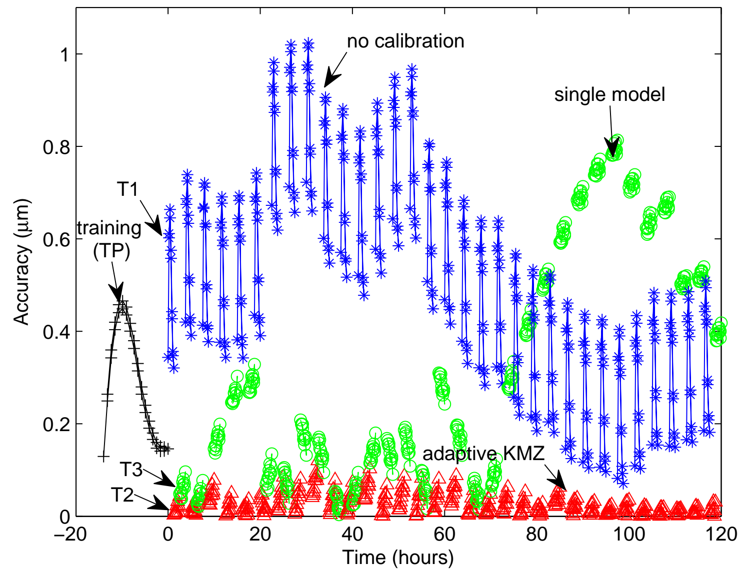

Figure 5.17: Accuracy evolution of all validation poses in five days. Time 0 = end of training = start of validation.

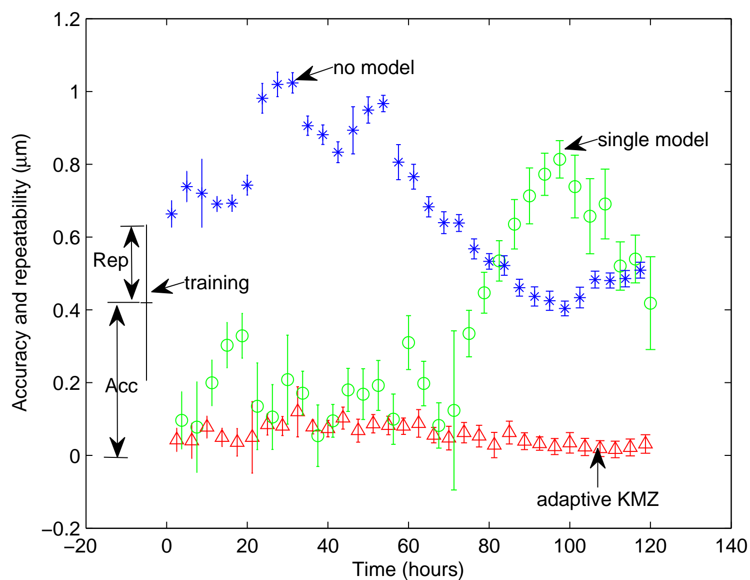

Figure 5.18: Evolution of maximum accuracy and repeatability of every test in five days. Time 0 = end of training = start of validation.

temperature range after training are close to those during training, the single model can provide efficient compensation based on previous knowledge. Adaptive model is able to update the new information that thermal drift can be compensated efficiently in spite of how temperature changes.

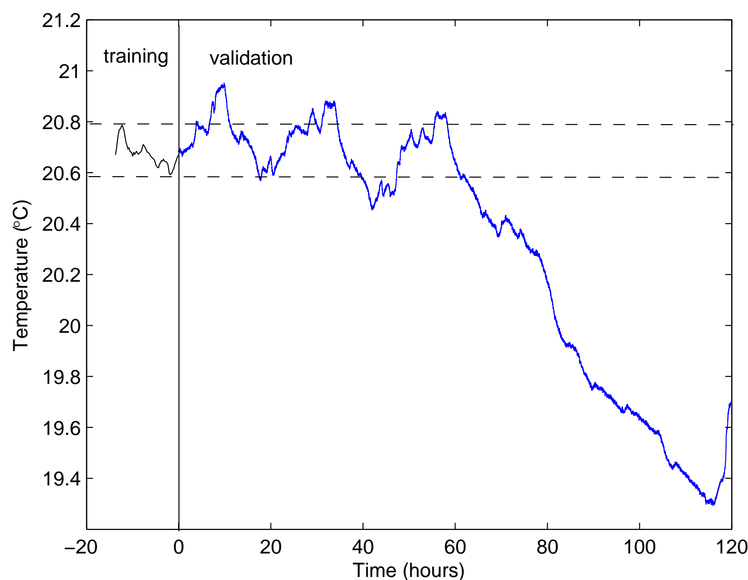

Figure 5.19: Evolution of the room temperature in five days.

Based on the equations in Section 5.1, the space and time robustness indices are calculated and shown in Table 5.2. The quantified values clearly show that the robustness indices using calibration (0.044 and 0.048 in space, 0.002 and 0.004 in time) is much better than those of no calibration (0.369 in space and 0.018 in time). Adaptive model using KMZ is the best with smallest robustness indices.

Table 5.2: Robustness of calibration of nanopositioning stage.

	No calibration	adaptive model using KMZ	single model
Space robustness R_S	0.369	0.044	0.048
Time robustness R_T	0.018	0.002	0.004

5.4 Calibration of Multi-DoF nanopositioning stage

The above study of 1-DoF calibration of nanopositioning stage can be extended to multi-DoF study of coupling effect. This section illustrates the extension of single model to multi-DoF case (with 2-DoF as example).

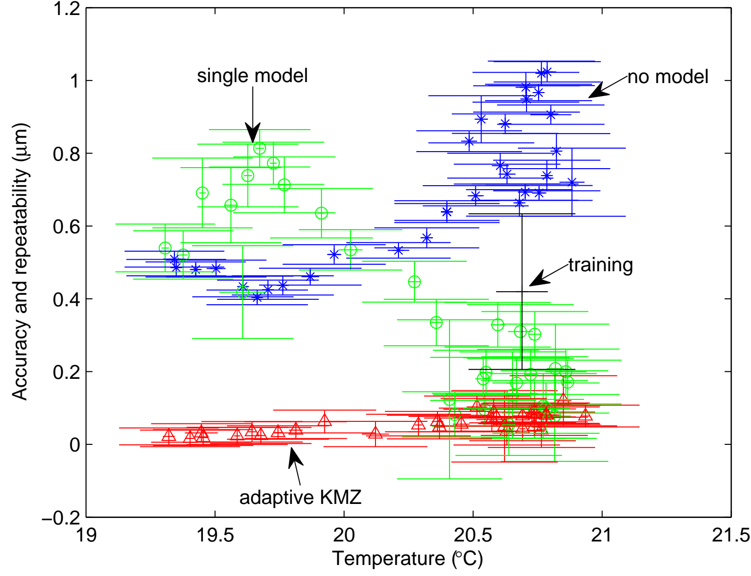

Figure 5.20: Relationship between temperature and accuracy and repeatability.

5.4.1 Modeling of 2-DoF nanopositioning stage

Similar to the 1-DoF nanopositioning, the 2-DoF is also modeled with polynomials. The difference from 1-DoF is the consideration and compensation of coupling errors from one axis to another. We define the following model for the 2-DoF nanopositioning stage:

$$\begin{cases} q_x = \sum_{i=1}^{n1} a_{ix} x^i + \sum_{i=1}^{n2} b_{ix} y^i + \sum_{i=1}^{n3} c_{ix} t_i + \lambda_x, \\ q_y = \sum_{i=1}^{n1} a_{iy} x^i + \sum_{i=1}^{n2} b_{iy} y^i + \sum_{i=1}^{n3} c_{iy} t_i + \lambda_y, \end{cases} \tag{5.10}$$

where a_{ij} is the ith coefficient for modeling errors along j axis induced by X motion; b_{ij} is the ith coefficient for modeling errors along j axis induced by Y motion; c_{ij} is the ith coefficient for modeling thermal drift along j axis; λ_j is the offset term along j axis.

5.4.2 Experimental study of 2-DoF nanopositioning robot

Procedures of calibration and validation

Fig. 5.21 shows the trajectory of joint space for data acquisition for model training. The measurements are taken at positions 0:10:80 μm along XY and 81 pairs of measurements are obtained in every cycle. At the end of every cycle, nanopositioning robot is controlled to go back to the start point from the end point. Totally 12 cycles are finished during 6 hours of training phase.

Five points (P_1,...,P_5) never used for training plus the origin P_0 are chosen for validation (Fig. 5.22). The coordinates of these points are $(0, 0)$, $(45, 45)$, $(75, 15)$,

(75, 75), (15, 75), and (15, 15) μm. The nanopositioning stage is controlled from P_0 to P_1,...,P_5 in turn, and then goes back to P_0 for a new cycle.

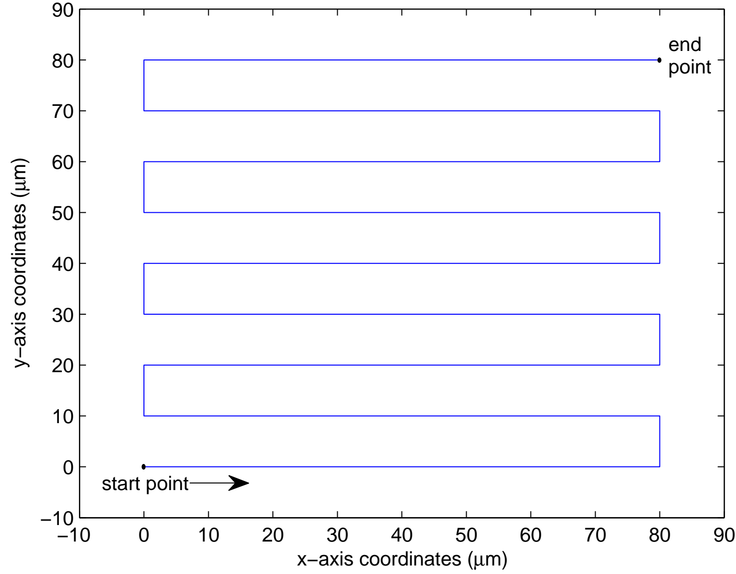

Figure 5.21: Trajectory of data acquisition for model training.

Experimental results

Fig. 5.23 shows the overall accuracy and repeatability of 2-DoF nanopositioning stage. The accuracy value in the training phase is larger than 1.4 μm. After training, performance tests are performed with and without using the calibration model Eq. (5.10). In nearly one day, the accuracy of no calibration is always about 1.2 $\sim$ 1.4 μm which is in quite the same range as the accuracy in training phase. Using the calibrated model, most of the accuracies keep better than 200 nm and all of them are better than 500 nm. The temperature evolution during this time is shown in Fig. 5.24. When temperature changes within the range as the training temperature, accuracy can even be better than 200 nm which is much superior to that (1400 nm) without using model.

5.5 Conclusions

Nanopositioning robot suffers from geometric errors derived from nonlinear behavior of large deformation of flexible structure and designing principle of the actuator. In addition, thermal drift is also a major source of inaccuracy. To improve the nanopositioning accuracy, we need to compensate the geometric errors and thermal drift.

This chapter presented theoretical formulations, modeling discussions, and experimental validation results. A single model and an adaptive model has been proposed. Sin-

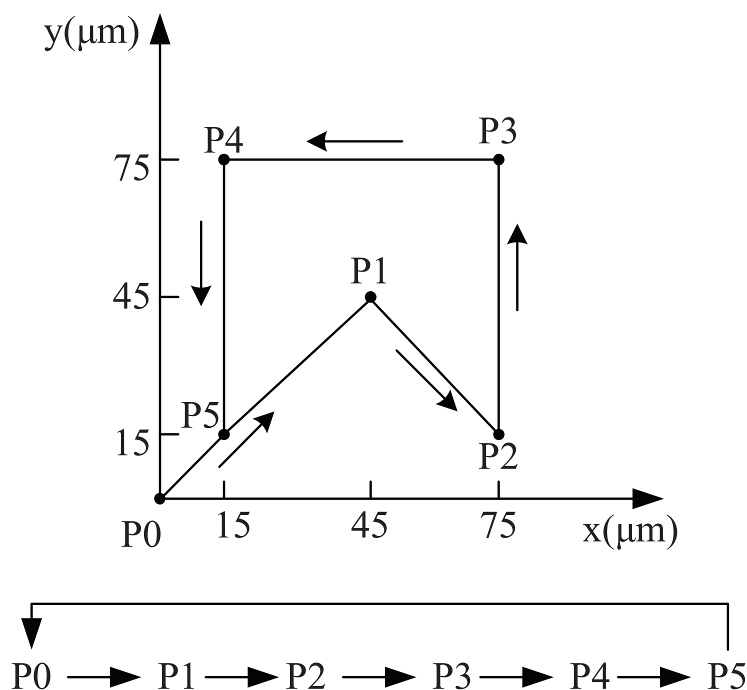

Figure 5.22: Coordinates and trajectory of six points for validation.

gle model depicted the geometric errors and thermal drift in a static structure. Adaptive model was able to compensate thermal drift by updating the drift information through revisiting the kilometer-zero. Based on measurements of interferometer and thermocouples, a set of experiments had been conducted to characterize, calibrate, and improve the performances of the nanopositioning stages.

The experimental results demonstrated that the performance of single model largely depended on the consistency of conditions before and after training. If the drift behavior and temperature range after training were close to those during training, the single model can guarantee efficient compensation based on training knowledge. Results showed that accuracy is better than 400 nm in this case. Adaptive model was able to update the new information that thermal drift can be compensated efficiently in spite of how temperature changes. The achieved accuracies were in the 100 nm range. On the other side, without compensation, accuracy could be up to 1000 nm even if temperature did not go far away from the training range. Calculation of time and space robustness provide numerical comparison of two models and no calibration.

In addition, we extend 1-DoF calibration to multi-DoF by a case study of 2-DoF nanopositioning robot. Results also demonstrated the model efficiently to improve the 2D accuracy from 1400 nm to 200 nm.

In the above experiments, we use the interferometer to define the KMZ. Alternatively, the KMZ can also be defined by another low cost sensor because the interferometer

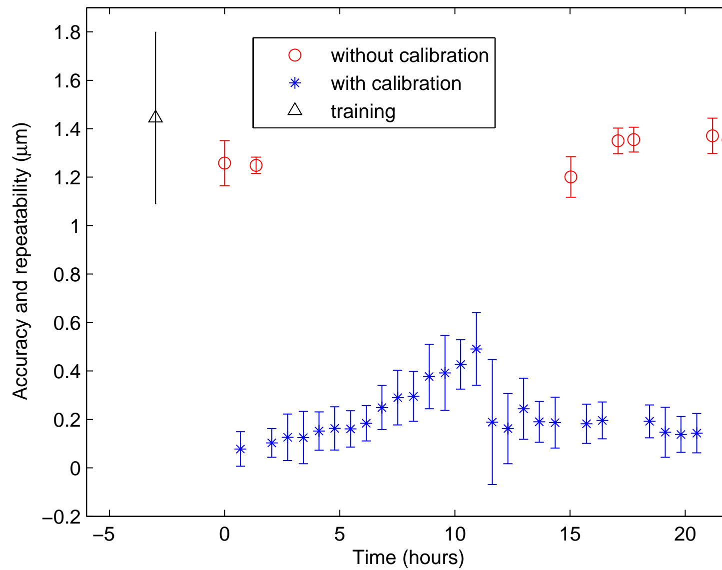

Figure 5.23: Experimental accuracy and repeatability of 2-DoF nanopositioning stage in training and validation phases. Time 0 = end of training = start of validation.

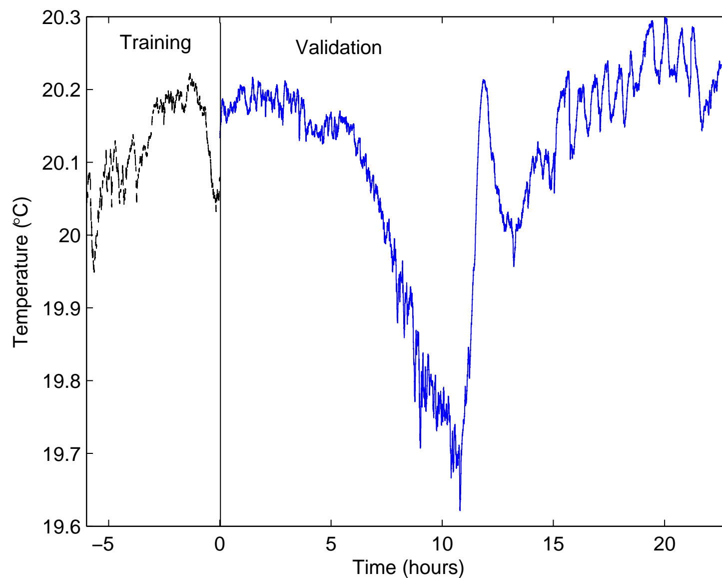

Figure 5.24: Temperature evolution in training and validation phases.

should not be used during the whole working phase of nanopositioning stage otherwise it is better to use closed loop control. Such kind of sensors should be small-sized to avoid

temperature influence and with good temperature stability, high resolution and small measuring range. We propose AFM probe to define the KMZ because AFM probe has very good thermal stability [10]. Fig. 5.25 is the schematic diagram of the experimental setup consisting of the nanopositioning stage, a KMZ cell, and a circuit. The nanopositioning stage is made up of a fixed part and a mobile part. The KMZ cell contains an AFM probe fixed on a PCB, a screw fixed with a conductive part, and two fixtures. The circuit consists of a resister (R), a capacitor (C), and a generator. The screw is used to finely adjust the distance between conductive part and the AFM tip. The conductive part is fixed to the screw which can be fixed by the nut on fixture 1. The AFM probe is fixed on the PCB and then both of them are fixed to fixture 2.

Fig. 5.26 shows the real prototype of this solution. In the prototype, we use a small piece of silicon coated with a layer of gold as the conductive part. The AFM probe (*Electri*Cont-G from Budget Sensors) is electrically conductive thanks to coating of 5 nm Chromium and 25 nm Platinum on both sides of the probe. A voltage is applied between the AFM probe and the ground. The conductive part is grounded because the mobile part, the nanopositioning stage and the table are all electrically conductive. The voltage will decrease to a low level when the mechanical contact is full established.

The main working principle is:

- AFM probe defines an reference frame (AFM frame) with the origin d_0. We assume that this frame does not move even if temperature affects.

- At time T_0, nanopositioning stage is at the initial position measured by the internal sensor ($x_{Im} = 0$). This position is d_1 with respect to the AFM frame.

- At time T_1, the mobile part of the nanopositioning stage touches the AFM tip while electrical contact is established. The internal sensor records the measurement x_{Im1} at that time. Because T_1 is short based on the thermal changing speed, x_{Im1} can be seen as the reference origin of the kilometer-zero.

- After a period of time T_2, the mobile part gets back to the zero position defined by the internal sensor (x_{Im}=0). However, during this time, the zero position has drifted to d_2 because of temperature change.

- Then, the mobile part touches the AFM tip again and the internal sensor records the measurement x_{Im2}.

- Finally, the thermal drift $d_2 - d_1$ can be calculated by $x_{Im1} - x_{Im2}$.

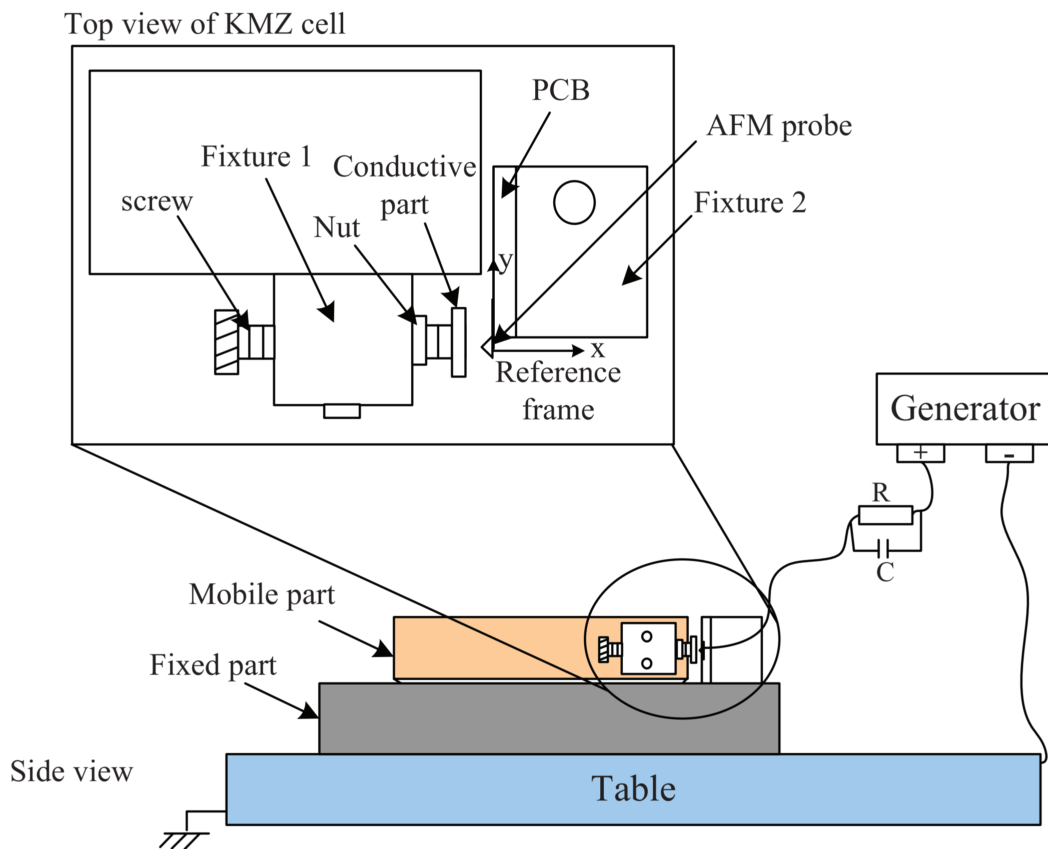

Figure 5.25: Schematic diagram of experimental setup with kilometer-zero defined by the AFM probe.

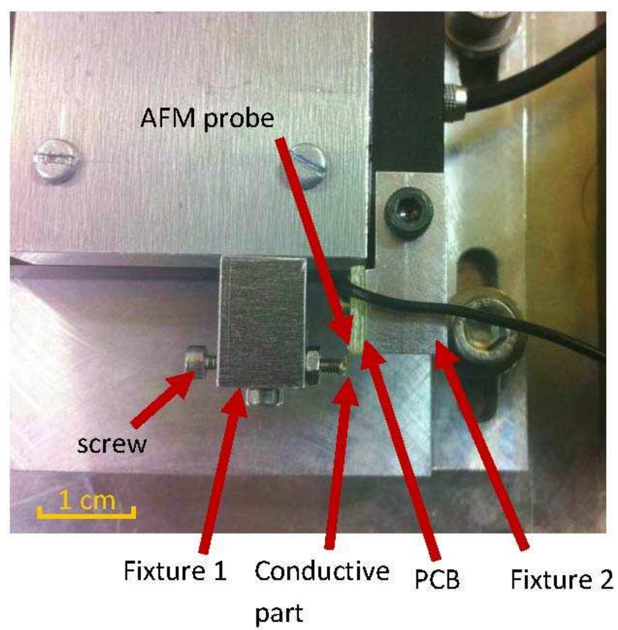

(a) Whole view of the KMZ cell

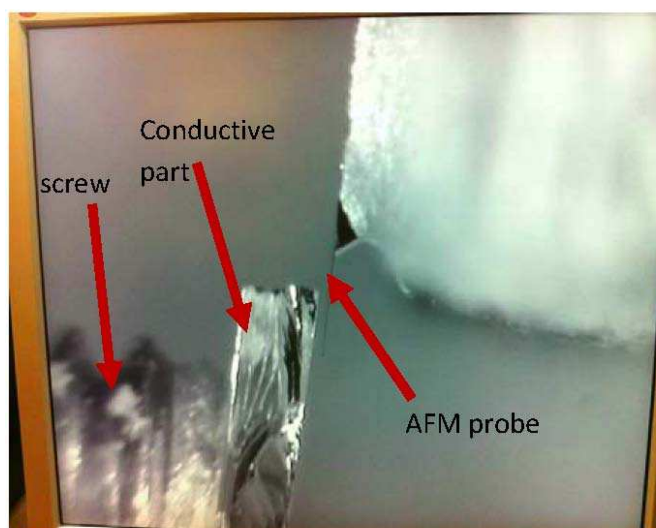

(b) Local view of the small parts

Figure 5.26: Prototype of the KMZ cell.

Chapter 6

Conclusions

In this thesis, at first, we presented the motivations of our research. Our work was driven by the need of high-accuracy micro-nano robots for microscale applications. The typical accuracy level ranges from some tens of microns to a few nanometers. At the microscale, there are many sources hindering the improvement of accuracy, such as assembly errors between two axes, nonlinearity along the axis, environmental disturbances. To compensate these imperfections so as to improve the accuracy, we need to measure the positions of the micro-nano robot accurately. However, sensing at the microscale is a tough issue and suitable sensors are not easy to take. Once sensing solution is available, we chose robot calibration in open loop as the control strategy because: (i) only closed loop in actuator layer is not sufficient; (ii) it avoids to use several sensors at the same in small space when applying the micro-nano robot. To evaluate the accuracy and repeatability of the micro-nano robot, we adapted the metrics based on ISO 9283 standard, and proposed complementary definition for repeatability. Based on the state-of-the-art, we set up the objectives to achieve accuracy better than 4 μm for micropositioning and 100 nm for nanopositioning systems.

There are three problems to be solved: (i) performances of micro-nano robots are not well known and should be studied and characterized; (ii) sensing solutions for micro-nano positioning measurement; (iii) improvement of micro-nano positioning accuracy. The main imperfections at the micro-nanoscales are structure and dimension errors, assembly errors, nonlinearities (position and angle) along the motion axis, environmental disturbances, etc. For micropositioning, we chose the vision system with Pseudo-Periodic Pattern (PPP) as the sensing tool. A generic calibration framework was considering the most influential imperfections, i.e. assembly errors, position-dependent errors, and angle-dependent errors. Different sets of imperfections were tackled by five models that their influences could be quantified. The final positioning accuracy was improved. In the case study of $XY\Theta$ microrobotic system, the most basic model (Model I) obtained 96 μm accuracy, and the accuracy was improved model by model. The best accuracy achieved was 3 μm with the most advanced model (Model V). For nanopositioning, we chose interferometer as the sensing tool. Geometric errors and thermal drift were tried to compensated by a single model and an adaptive model using KiloMeter-Zero (KMZ).

Single model worked well when temperature keeps within or close to the range of training phase. Adaptive model achieve the best performance that accuracies were always better than 100 nm thanks to the update of thermal-drift information.

The idea of the research is to focus on using existing modeling tools and identification algorithms to explore unknown knowledge and to propose new calibration models. The research performed in this thesis led to several original contributions for micropositioning. A general calibration framework was presented including general modeling, errors description, and parameters identification. We applied a novel measuring system for micropositioning sensing, i.e., vision with PPP and its algorithm. Characterization and compensation were conducted for position-dependent errors inherent in the XY micropositioning stages. We considered the four kinds of main imperfections and took them into account in five calibration model consisting of forward and inverse kinematics. Different models tackled different sets of imperfections. To quantify the influences of these imperfections, we proposed and performed a set of experimental validation tests. Finally, we know the importance of different sources and improve the positioning accuracy of the microrobotic system experimentally.

For nanopositioning, we also contributed to several aspects. A single model was proposed based on behaviors of geometric errors of nanopositioning stage and thermal drift. An adaptive model using KMZ was proposed for compensating thermal drift. We implemented experimental validation tests for the two models and comparisons with no model were performed after calibration training. We investigated the robustness of calibration in the long term in terms of space and time. Besides, a prototypal solution using AFM probe was proposed to define the KMZ.

The idea of modeling of micro-nano robots is based on the robots' motion behavior. The model is established according to characterization results of motion errors. Furthermore, we proposed new definitions of intrinsic and extrinsic repeatabilities complementary to the concept of repeatability.

Based on what have been achieved and remaining problems, we can draw some remarks for future directions. We can try to get benefits from existing calibration methods at the macroscale, and apply to microscale robot calibration. For example, self-calibration of a macrorobot can be realized based on hand-eye vision. Microrobot can not be attached with a camera but usually can be integrated with MEMS force sensor. In this case, microrobot may also be self-calibrated using information provided by the force sensor.

A very important condition to achieve a successful calibration is the use of a powerful measuring system. However, due to rigorous requirements on resolution, accuracy, range, multi-DoF, size, etc., such device is still not available in the market. Because sensing is a fundamental issue at the microscale, improvement in this area can benefit to many aspects. Except for developing advanced sensors, fusion of available sensors would be an alternative and efficient way to get more accurate, more complete, and more reliable measurement. For example, in a micromanipulation task, there involve several sensors including internal and external ones. Making an intelligent sensing architecture by integrating multi-sensor information can extract accurate information on position, speed,

force, and so on. This would be better than when these information sources are used individually.

Moreover, the KMZ method should be improved in regard to accuracy, reliability, price, etc. That is, the objective is to find a relatively low-cost solution which is able to precisely define the reference frame insensitive to external disturbances. This kind of sensor should be able to make direct measurement of the mobile part of interest and stable subjected to temperature disturbance.

Bibliography

[1] Manipulating industrial robots - performance criteria and related test methods, ISO 9283: 1998.

[2] Point-to-point and static performance characteristics-evaluation, ANSI/RIA R 15.05-1-1990.

[3] Y. Bai. On the comparison of model-based and modeless robotic calibration based on a fuzzy interpolation method. *International Journal of Advanced Manufacturing Technology*, 31:1243–1250, 2007.

[4] Y. Bai and D. Wang. On the comparison of trilinear, cubic spline, and fuzzy interpolation methods in the high-accuracy measurements. *IEEE Transactions on Fuzzy Systems*, 18(5):1016–1022, 2010.

[5] Y. Bai and H. Zhuang. On the comparison of bilinear, cubic spline, and fuzzy interpolation techniques for robotic position measurements. *IEEE Transaction on Instrumentation and Measurement*, 54(6):2281–2288, 2005.

[6] Y. Bellouard. *Microrobotics: Methods and Applications*. CRC Press, 2009.

[7] J. H. Borm and C. H. Menq. Determination of optimal measurement configurations of robot calibration based on observibility measure. *International Journal of Robotics Research*, 10(1):51–63, 1991.

[8] B. Borovic, A. Liu, D. Popa, H. Cai, and F. Lewis. Open-loop versus closed-loop control of mems devices: choices and issues. *Journal of Micromechanics and Microengineering*, 15(10):1917–1924, 2005.

[9] M. Boudaoud, Y. Haddab, Y. Le Gorrec, and P. Lutz. Noise characterization in millimeter sized micromanipulation systems. *International Journal of Mechatronics*, 21(6):1087–1097, 2011.

[10] M. Boudaoud, Y. Haddab, Y. Le Gorrec, and P. Lutz. Study of thermal and acoustic noise interferences in low stiffness atomic force microscope cantilevers and characterization of their dynamic properties. *Review of Scientific Instruments*, 81(1), 2012.

[11] J. F. Brethé. Granular stochastic modeling of robot micrometric precision. In *IEEE/RSJ International Conference on Intelligent Robots and Systems*, pages 4066–4071, 2011.

[12] D. Cappelleri, P. Cheng, J. Fink, G. Gavrea, and V. Kumar. Automated assembly for mesoscale parts. *IEEE Transactions on Automation Science and Engineering*, 8(3):598–613, 2011.

[13] D. Cappelleri, M. Fatovic, and U. Shah. Caging micromanipulation for automated microassembly. In *IEEE International Conference on Robotics and Automation*, Shanghai, China, 2011.

[14] D. Cappelleri, J. Fink, B. Mukundakrishnan, V. Kumar, and J. Trinkle. Designing open loop plans for planar micro manipulation. In *IEEE International Conference on Robotic and Automation*, Orlando, FL, USA, 2006.

[15] H. F. F. Castro. Uncertainty analysis of a laser calibration system for evaluating the positioning accuracy of a numerically controlled axis of coordinate measuring machines and machine tools. *Precision Engineering*, 32(2):106–113, 2008.

[16] N. Chaillet and S. Régnier. *Microrobotics for Micromanipulation*. Wiley-ISTE, 2010.

[17] H. Chen, T. A. Fuhlbrigge, S. Choi, J. Wang, and X. Li. Practical industrial robot zero offset calibration. In *IEEE International Conference on Automation Science and Engineering*, pages 516–521, Arlington, VA, USA, 2008.

[18] J. S. Chen, J. Yuan, and J. Ni. Thermal error modelling for real-time error compensation. *The International Journal of Advanced Manufacturing Technology*, 12:266–275, 1996.

[19] C. Clévy, M. Rakotondrabe, and N. Chaillet. *Signal measurement and estimation techniques for micro and nanotechnology*. Springer, 2011.

[20] A. N. Das, R. Murthy, D. O. Popa, and H. E. Stephanou. A multiscale assembly and packaging system for manufacturing of complex micro-nano devices. *IEEE Transactions on Automation Science and Engineering*, 9(1):160–170, 2012.

[21] A. N. Das, P. Zhang, W. H. Lee, D. Popa, and H. Stephanou. Multiscale, deterministic micro-nano assembly system for construction of on-wafer microrobots. In *IEEE International Conference on Robotics and Automation*, 2007.

[22] G. Dogangil, B. L Davies, and F. Rodriguez y Baena. A review of medical robotics for minimally invasive soft tissue surgery. *Proceedings of the IMechE, Part H, Journal of Engineering in Medicine*, 224(5):653–679, 2010.

[23] B. R. Donald, C. G. Levey, and I. Paprotny. Planar microassembly by parallel actuation of mems microrobots. *Journal of Microelectromechanical Systems*, 17(4):789–808, 2008.

[24] M. R. Driels and U. S. Pathre. Significance of observation strategy on the design of robot calibration experiments. *Journal of Robotic Systems*, 7(2):197–223, 1990.

[25] M. R. Driels, L. W. Swayze, and L. S. Potter. Full-pose calibration of a robot manipulator using a coordinate measuring machine. *The International Journal of Advanced Manufacturing Technology*, 8(1):34–41, 1993.

[26] A. Y. Elatta, P. Li, L. Fan, D. Yu, and F. Luo. An overview of robot calibration. *Information Technology Journal*, 3(1):74–78, 2004.

[27] N. Fazenda. *Calibration of High-Precision Flexure Parallel Robots.* PhD thesis, EPFL, Lausanne, 2007.

[28] S. Fraser, M. H. Attia, and M. O. M. Osman. Modelling, identification and control of thermal deformation of machine tool structures, part 2: Generalized transfer functions. *Journal of Manufacturing Science and Engineering*, 120(3):632–639, 1998.

[29] P. Glass, E. Cheung, and M. Sitti. A legged anchoring mechanism for capsule endoscopes using micropatterned adhesives. *IEEE Transactions on Biomedical Engineering*, 55(12):2759–2767, 2008.

[30] C. Gong, J. Yuan, and J. Ni. Nongeometric error identification and compensation for robotic system by inverse calibration. *International Journal of Machine Tools and Manufacture*, 40(14):2119–2137, 2000.

[31] E. J. Griffith and S. Akella. Coordinating multiple droplets in planar array digital microfluidic systems. *International Journal of Robotics Research*, 24(11):933–949, 2005.

[32] R. He, Y. Zhao, S. Yang, and S. Yang. Kinematic-parameter indentification for serial-robot calibration based on POE formula. *IEEE Transactions on Robotics*, 26(3):411–423, 2010.

[33] J. M. Hollerbach and C. W. Wampler. The calibration index and taxonomy for robot kinematic calibration methods. *International Journal of Robotics Research*, 15(6):573–591, 1996.

[34] S. Hu and D. Sun. Automatic transportation of biological cells with a robot-tweezer manipulation system. *International Journal of Robotics Research*, 30(14):1681–1694, 2011.

[35] M. Jääskeläinen, V. Sariola, and Q. Zhou. Environmental effects on droplet self-alignment assisted hybrid microassembly. In *IEEE International Symposium on Assembly and Manufacturing*, pages 177–182, Suwon, Korea, 2009.

[36] J. H. Jang, S. H. Kim, and Y. K. Kwak. Calibration of geometric and nongeometric errors of an industrial robot. *Robotica*, 19:311–321, 2001.

[37] J. Jeswieta and R. Helferty. Measuring robot repeatability an application of ISO and ANSI standards. *Advanced Robotics*, 10(5):503–520, 1996.

[38] W. Jing, N. Pagano, and D. Cappelleri. A micro-scale magnetic tumbling micro-robot. In *ASME International Design Engineering Technical Conferences*, Chicago, IL, USA, 2012.

[39] N. Kammerer and Y. Perrot. High accuracy patient positioning system: geometric and elastic error calibration of a flexible model. In *IEEE International Conference on Automation Science and Engineering*, Seoul, Korea, 2012.

[40] C. W. Kennedy and J. P. Desai. Modeling and control of the mitsubishi PA10 robot arm harmonic drive system. *IEEE/ASME Transactions on Mechatronics*, 10(3):263–274, 2005.

[41] W. Khalil and S. Besnard. Self calibration of stewart-gough parallel robots without extra sensors. *IEEE Transaction on Robotics and Automation*, 15(6):1116–1121, 1999.

[42] W. Khalil and S. Besnard. Geometric calibration of robots with flexible joints and links. *Journal of Intelligent and Robotic Systems*, 34:357–379, 2002.

[43] W. Khalil, S. Besnard, and Ph. Lemoine. Comparison study of the geometric parameters calibration methods. *International Journal of Robotics and Automation*, 15(2):56–67, 2000.

[44] W. Khalil and É. Dombre. *Modeling, Identification and Control of Robots*. Hermes Penton Science, London, 2004.

[45] W. Khalil, M. Gautier, and P. Lemoine. Identification of the payload inertial parameters of industrial manipulators. In *IEEE International Conference on Robotics and Automation*, pages 4943–4948, Roma, Italy, 2007.

[46] D. A. Krulewich. Temperature integration model and measurement point selection for thermally induced machine tool errors. *Mechatronics*, 8:395–412, 1998.

[47] J. W. Li, W. J. Zhang, G. S. Yang, S. D. Tu, and X. B. Chen. Thermal-error modeling for complex physical systems: The-state-of-the-arts review. *INT J ADV MANUF TECH*, 42:168–179, 2009.

[48] T. Li, K. Sun, Y. Jin, and H. Liu. A novel optimal calibration algorithm on a dexterous 6 DOF serial robot-with the optimization of measurement poses number. In *IEEE International Conference on Robotics and Automation*, pages 975–981, Shanghai, China, 2011.

[49] C. Lightcap, S. Hamner, T. Schmitz, and S. Banks. Improved positioning accuracy of the PA10-6CE robot with geometric and flexibility calibration. *IEEE Transcations on Robotics*, 24(2):452–456, 2008.

[50] L. Liu, S. Pal, and H. Xie. Mems mirrors based on a curved concentric electrothermal actuator. *Sensors and Actuators A: Physical*, pages 2522–2525, 2012.

[51] Y. Liu, N. Xi, G. Zhang, X. Li, H. Chen, C. Zhang, M. J. Jeffery, and T. A. Fuhlbrigge. An automated method to calibrate industrial robot joint offset using virtual line-based single-point constraint approach. In *IEEE International Conference on Intelligent Robots and Systems*, pages 715–720, St. Louis, USA, 2009.

[52] Y. Lou, T. Chen, Y. Wu, Z. Li, and S. Jiang. Improved and modified geometric formulation of POE based kinematic calibration of serial robots. In *IEEE/RSJ International Conference on Intelligent Robots and Systems*, pages 5261–5266, St. Louis, USA, 2009.

[53] Z. Lu, X. Zhang, C. Leung, N. Esfandiari, R. F. Casper, and Y. Sun. Automated cell manipulation: Robotic ICSI. In *IEEE International Conference on Robotics and Automation*, 2011.

[54] E. Lubrano. *Calibration of ultra-high-precision robots operating in an unsteady environment.* PhD thesis, EPFL, Lausanne, 2011.

[55] E. Lubrano and R. Clavel. Thermal behavior of an ultra high-precision linear axis operating in industrial environment. In *9th International Workshop on Research and Education in Mechatronics*, pages 151–152, 2008.

[56] S. Marie and P. Maurine. Elasto-geometrical modeling of closed-loop industrial robots used for machining applications. In *International conference on robotics and automation*, pages 1294–1300, Pasadena, CA, USA, 2008.

[57] A. Matsumoto, K. Yoshida, and Y. Maeda. *Design of a Desktop Microassembly Machine and its Industrial Application to Microsolder Ball Manipulation, in Robotic Microassembly.* John Wiley & Sons, Inc., Hoboken, NJ, USA, 2010.

[58] L. S. Mattos and D. G. Caldwell. A fast and precise micropipette positioning system based on continuous camera-robot recalibration and visual servoing. In *IEEE International Conference on Automation Science and Engineering*, pages 609–614, Bangalore, India, 2009.

[59] M. A. Meggiolaro, S. Dubowsky, and C. Mavroidis. Geometric and elastic error calibration of a high accuracy patient positioning system. *Mechanism and Machine Theory*, 40:415–427, 2005.

[60] Y. Meng and H. Zhuang. Autonomous robot calibration using vision technology. *Robotics and Computer-Integrated Manufacturing*, 23(4):436–446, 2007.

[61] A. Nahvi and J. M. Hollerbach. The noise amplification index for optimal pose selection in robot calibration. In *IEEE International Conference on Robotics and Automation*, pages 647–654, Minneapolis, Minnesota, USA, 1996.

[62] T. F. Niaritsiry, N. Fazenda, and R. Clavel. Study of the sources of inaccuracy of a 3 DOF flexure hinge-based parallel manipulator. In *IEEE International Conference on Robotics and Automation*, pages 4091–4096, 2004.

[63] K. Okamura and F. C. Park. Kinematic calibration using the product of exponentials formula. *Robotica*, 14:415–421, 1996.

[64] C. Pawashe and M. Sitti. Two-dimensional vision-based autonomous microparticle manipulation using a nanoprobe. *Journal of Micromechatronics*, 3(3-4):285–306, 2006.

[65] D. O. Popa, R. Murthy, and A. N. Das. M3-deterministic, multiscale, multirobot platform for microsystems packaging: Design and quasi-static precision evaluation. *IEEE Transactions on Automation Science and Engineering*, 6(2):345–361, 2009.

[66] K. Rabenorosoa, C. Clévy, Q. Chen, and P. Lutz. Study of forces during microassembly tasks using two-sensing-fingers gripper. *IEEE/ASME Transactions on Mechatronics*, 17(5):811–821, 2012.

[67] K. Rabenorosoa, C. Clévy, and P. Lutz. Active force control for robotic microassembly: application to guiding tasks. In *IEEE International Conference on Robotics and Automation*, pages 2137–2142, Anchorage, AK, USA, 2010.

[68] K. Radkhah, T. Hemker, M. Friedmann, and O. von Stryk. Towards the deployment of industrial robots as measurement instruments - an extended forward kinematic model incorporating geometric and nongeometric effects. In *IEEE/ASME conference on advanced intelligent mechatronics*, pages 124–129, 2009.

[69] M. Rakotondrabe, C. Clévy, and P. Lutz. Complete open loop control of hysteretic, creeped, and oscillating piezoelectric cantilevers. *IEEE Transactions on Automation Science and Engineering*, 7(3):440–450, 2009.

[70] P. Renaud, N. Andreff, J.M. Lavest, and M. Dhome. Simplifying the kinematic calibration of parallel mechanisms using vison-based metrology. *IEEE Transcations on Robotics*, 22(1):12–22, 2006.

[71] P. Renaud, N. Andreff, P. Martinet, and G. Gogu. Kinematic calibration of parallel mechanisms: a novel approach using legs observation. *IEEE Transcations on Robotics*, 21(4):529–538, 2005.

[72] A. A. G. Requicha, D. J. Arbuckle, B. Mokaberi, and J. Yun. Algorithms and software for nanomanipulation with atomic force microscopes. *International Journal of Robotics Research*, 28(4):512–522, 2009.

[73] Z. Roth, B. Mooring, and B. Ravani. An overview of robot calibration. *IEEE Journal of Robotics and Automation*, 3(5):377–385, 1987.

[74] P. Saketi, M. Von Essen, M. Mikczinski, S. Heinemann, S. Fatikow, and P. Kallio. A flexible microrobotic platform for handling microscale specimens of fibrous materials for microscopic studies. *Journal of Microscopy*, 248(2):163–171, 2012.

[75] P. Sandoz, R. Zeggari, L. Froelhy, J. L. Prétet, and C. Mougin. Position referencing in optical microscopy thanks to sample holders with out-of-focus encoded patterns. In *Journal of Microscopy*, volume 255, 293-303.

[76] J. Sun and H. Xie. MEMS-based endoscopic optical coherence tomography. *International Journal of Optics*, 2011(825629), 2011.

[77] Y. Sun and J. M. Hollerbach. Observability index selection for robot calibration. In *IEEE International Conference on Robotics and Automation*, pages 831–836, 2008.

[78] Y. Sun and B. J. Nelson. Biological cell injection using an autonomous microrobotic system. *International Journal of Robotics Research*, 21(10-11):861–868, 2002.

[79] H. D. Taghirad, P. R. Belanger, and A. Helmy. An experimental study on harmonic drives. Technical report, International Submarine Engineering Ltd., McGill University, Center for Intelligent Machines, 1996.

[80] B. Tamadazte, T. Arnould, S. Dembélé, N. Le Fort-Piat, and E. Marchand. Real-time vision-based microassembly of 3D MEMS. In *IEEE/ASME International Conference on Advanced Intelligent Mechatronics*, 2009.

[81] B. Tamadazte, S. Dembélé, and N. Le Fort-Piat. CAD model-based tracking and 3D visual-based control for MEMS microassembly. *International Journal of Robotics Research*, 29(11):1416–1434, 2010.

[82] B. Tamadazte, N. Le-Fort Piat, and E. Marchand. A direct visual servoing scheme for automatic nanopositioning. *IEEE-ASME Transactions on Mechatronics*, 17(4):728–736, 2012.

[83] N. Tan, C. Clévy, and N. Chaillet. Calibration of single-axis nanopositioning cell subjected to thermal disturbance. In *IEEE International Conference on Robotics and Automation*, pages 3645–3650, Karlsruhe, Germany, 2013.

[84] N. Tan, C. Clévy, G.J. Laurent, and N. Chaillet. Calibration and validation of XYΘ micropositioners with vision. In *IEEE/ASME International Conference on Advanced Intelligent Mechatronics*, pages 256–261, Kaohsiung, Taiwan, 2012.

[85] P. Y. Tao, G. Yang, and M. Tomizuka. A calibration framework for industrial robotic work cells. In *IEEE/ASME International Conference on Advanced Intelligent Mechatronics (AIM)*, pages 1637–1642, Wollongong, Australia, 2013.

[86] M. Vincze, J. P. Prenninger, and H. Gander. A laser tracking system to measure position and orientation of robot end effectors under motion. *International Journal of Robotics Research*, 13:305–314, 1994.

[87] Q. Xu, Y. Li, and N. Xi. Design, fabrication, and visual servo control of an XY parallel micromanipulator with piezo-actuation. *IEEE Transactions on Automation Science and Engineering*, 6(4):710–719, 2009.

[88] J. A. Galeano Zea. *Position referenced microscopy: microfabricated pseudo-periodic patterns for absolute positioning of specimens with sub-micrometer accuracy.* PhD thesis, Université de Franche-Comté, 2011.

[89] J. A. Galeano Zea, P. Sandoz, E. Gaiffe, J. L. Prétet, and C. Mougin. Pseudo-periodic encryption of extended 2-D surfaces for high accurate recovery of any random zone by vision. *International Journal of Optomechatronics*, 4(1):65–82, 2010.

[90] Y. Zhang, M. Han, C. Y. Shee, and W. T. Ang. Calibration of piezoelectric actuator-based vision guided cell microinjection system. In *IEEE/ASME International Conference on Advanced Intelligent Mechatronics*, pages 808–812, Xi'an, China, 2008.

[91] H. Zhao, J. Yang, and J. Shen. Simulation of thermal behavior of a CNC machine tool spindle. *International Journal of Machine Tools and Manufacture*, 47(6):1003–1010, 2007.

[92] Q. Zhou, C. del Corral, P. J. Esteban, and A. Aurelian. Environmental influences on microassembly. In *IEEE/RSJ International Conference on Intelligent Robots and Systems*, 2002.

[93] Q. Zhou, P. Korhonen, J. Laitinen, and S. Sjövall. Automatic dextrous microhandling based on a 6 DOF microgripper. *Journal of Micromechatronics*, 3:359–387, 2006.

[94] J. Zhu. *Robust Thermal Error Modeling and Compensation for CNC Machine Tools.* PhD thesis, The University of Michigan, 2008.

[95] H. Zhuang, H. Motaghedi, and Z. S. Roth. Robot calibration with planar constraints. In *IEEE International Conference on Robotics and Automation*, volume 1, pages 805 – 810, Detroit, MI, USA, 1999.

[96] H. Zhuang, Z. S. Roth, and F. Hamano. A complete and parametrically continuous kinematic model for robot manipulators. *IEEE Transactions on Robotics and Automation*, 8(4):451–463, 1992.

Résumé :

Une des conditions fondamentales de la performance des systèmes repose sur leur capacité à générér des déplacements avec une précision de positionnement élevée. Cependant, à l'échelle micrométrique, de nombreux paramètres agissent et réduisent cette précision. A cette échelle, il est également particulièrement complexe de mesurer la précision de positionnement d'un système micro ou nanorobotique et donc d'identifier les différentes sources d'imprécision. L'étalonnage géométrique des systèmes micro et nanorobotiques prenant en compte ces différents sources est rarement étudié. Pour ces raisons, l'originalité et les contributions de cette thèse portent sur deux aspects principaux (i) la caractérisation des perperformances des systèmes micro et nanorobotiques et l'analyse des paramètres affectant leur précision de positionnement (ii) l'amélioration des performances de ces robots fondés sur différents types de modèles robotiques.

Abstract:

High accuracy is usually the necessary condition of the system performance. However, there are many sources of inaccuracy acting on microrobotic systems. At the microscale, it is very difficult to accurately measure the performances (positioning accuracy) of the micro-nano robots and to characterize the influences of the imperfections. The calibration of microrobotic systems combining all these sources is rarely studied and their relative importance remains unknown. The originalities and contributions of this thesis lie in two aspects: 1. characterization of micro-nano robots performances and influences of imperfections; 2. dealing with performance improvements of micro-nano robots based on different kinds of models.

■ École doctorale SPIM 16 route de Gray F - 25030 Besançon cedex

■ tél. +33 (0)3 81 66 66 02 ■ **ed-spim@univ-fcomte.fr** ■ www.ed-spim.univ-fcomte.fr

UFC
UNIVERSITÉ
DE FRANCHE-COMTÉ